A NOVEL SENSOR TO MONITOR SURFACE CHARGE INTERACTIONS: THE OPTICALLY STIMULATED CONTACT POTENTIAL DIFFERENCE PROBE

A Dissertation
Presented to
The Academic Faculty

By

Francis McCarthy Mess

In Partial Fulfillment
Of the Requirements for the Degree
Doctor of Philosophy in Mechanical Engineering

Georgia Institute of Technology

May 2006

A NOVEL SENSOR TO MONITOR SURFACE CHARGE INTERACTIONS: THE OPTICALLY STIMULATED CONTACT POTENTIAL DIFFERENCE PROBE

Approved by:

Dr. Steven Danyluk, Advisor
School of Mechanical Engineering
Georgia Institute of Technology

Dr. Thomas Kurfess
School of Mechanical Engineering
Georgia Institute of Technology

Dr. Jiri Janata
School of Chemistry
Georgia Institute of Technology

Dr. Peter Hesketh
School of Mechanical Engineering
Georgia Institute of Technology

Dr. Ajeet Rohatgi
School of Electrical and Computer Engineering
Georgia Institute of Technology

Date Approved: January 10, 2006

To my wife, Dawn

For selflessly allowing me to pursue my ambitions,

And not allowing me to abandon them.

Thank you.

ACKNOWLEDGMENTS

I would first like to thank my advisor, Dr. Steven Danyluk, for allowing me the opportunity to return to Georgia Tech and finish the work I began so many years ago. Few people have had such a persistent and substantial influence on my life. I also want to thank the members of my reading committee for their support, and guidance: Dr. Peter Hesketh, Dr. Jiri Janata, Dr. Thomas Kurfess, and Dr. Ajeet Rohatgi. My research experience and the quality of this work were substantially improved by their constructive criticisms and experimental suggestions.

Financial support for this research was provided the Office of Naval Research with special thanks to Dr. Peter Schmidt. I would like to thank Dr. Anatoly Zharin for his insight and advice, and particularly for his direct support of this research with the design and fabrication of several generations of CPD probes. I would also like to acknowledge the contributions of Sergey Tsiareshka, an excellent research partner and theoretical sounding board: thank you.

Due to the multi-disciplinary nature of this research, there were a large number of individuals that contributed substantially to this work and to whom I would like to express my gratitude:

To Yuri Pyekh for assistance in characterizing the frequency and gain characteristics of my CPD probe.

To Daniel and Andres Osorno for help with conducting experiments, and assistance in obtaining necessary lab equipment (sometimes creatively).

To Lisa Ellis for the critical re-discovery of the importance of surface preparation by HF etching.

To Dr. Vijay Yelundur for numerous meetings and feedback on the theoretical operation of the osCPD sensor and most importantly for his guidance and support in the use of PC1D software used to model the osCPD sensor photo-voltaic response.

To Jonathan Rudniecki of Analysts, Inc. for his knowledge of and industry perspective on oil degradation analysis, as well as for oil sample preparation and analysis.

To Dr. Mira Josowicz for her assistance with so many characterizations and measurements of my oil samples.

To Dr. Richard Crandall for his feedback and insight on semiconductor physics and photovoltaic response modeling.

To Arnab Choudhury for ellipsometric measurements of the silicon substrates.

Finally, I would like to thank my family and friends for years of encouragement and support, most especially Mom, Pop, Pat, and George. The eternal student is finally finished... for now.

TABLE OF CONTENTS

LIST OF TABLES

LIST OF FIGURES

LIST OF SYMBOLS AND ABBREVIATIONS

A	area
A_1	gain of 1st stage amplifier in CPD electronics
A_2	gain of 2nd stage amplifier in CPD electronics
A_m	molecular area of adsorption
α	photon absorption coefficient
α_1	fraction of molecules striking a surface that adhere or condense
AC	alternating current
b	relative concentration proportionality constant
B	reduced Helmholtz proportionality constant
c_n	electron capture coefficient
C	capacitance
C’	molar concentration of adsorbate species
C^*	relative concentration of adsorbate species
C_a	adsorbate concentration in conductimetric sensor
C_{eq}	equivalent capacitance of capacitors in series
C_{mica}	capacitance of mica sheet
C_{oil}	capacitance of oil sample
CPD	contact potential difference
C_{SiO2}	capacitance of native oxide film
ΔGA	standard adsorption free energy
d	separation gap in a parallel plate capacitor
d_0	average separation gap in a vibrating plate capacitor
d_1	amplitude of vibration in a vibrating plate capacitor
D_N	electron diffusion coefficient
ε	electric field
ε_o	permittivity of free space – 8.85×10^{-14} F/cm
ε_r	relative dielectric constant
e	fundamental unit of charge – 1.6×10^{-19}C
E_a	Activation energy in Arrhenius relation
E_o	vacuum or reference energy level
Ec	conduction band energy in a semiconductor
E_F	Fermi energy
E_i	Fermi energy for an intrinsic (un-doped) semiconductor
$E_{i(bulk)}$	intrinsic Fermi energy in bulk of semiconductor (away from surfaces)
$E_{i(surface)}$	intrinsic Fermi energy in at surface of semiconductor
E_V	valence band energy in a semiconductor
EHP	electron-hole pair
ϕ_F	work function of bulk silicon in flat band state
ϕ_s	surface potential of silicon
Φ	work function of a surface
Φ_T	work function of CPD probe tip
f	frequency (Hz)

FET	field effect transistor
γ	empirical calibration constant for conductimetric sensor
G	total gain of CPD amplification electronics and software artificial gain
G_L	photo-induced EHP generation rate
HF	hydrofluoric acid
I	intensity (W / cm^2)
I_D	drain current in MOSFET
i_{CPD}	CPD-induced current
I_o	maximum incident light intensity
J_N	total electron current
$J_{N\text{-}diff}$	electron diffusion current
$J_{N\text{-}drift}$	electron drift current
k	Boltzmann constant – 8.617×10^{-5} eV/K; 1.381×10^{-23} J/K
k^*	imaginary component of refractive index
K	reciprocal of the adsorption equilibrium constant
K_1	proportionality constant for nvCPD measurement of adsorption
λ	photon wavelength
L	characteristic absorption depth for 95% absorption
LAPS	light-addressable potentiometric sensor
LED	light emitting diode
μ_1	number of gram-molecules striking a surface per square cm per second
μ_n	electron mobility
μ_p	component of dipole moment perpendicular to the surface
M	measurement system gain constant for conductimetric sensor
MISC	metal insulator silicon capacitor
MOSC	metal oxide silicon capacitor
MOSFET	metal oxide silicon field effect transistors
ν_1	fraction of molecules striking a surface that immediately evaporate
n	electron density in semiconductor
n_i	intrinsic carrier concentration
n_o	equilibrium condition concentration of electrons
n_p	concentration of electrons in p-type silicon
n^*	real component of refractive index
n_1	charge density function in nvCPD adsorption model
n_a	number of adsorbed molecules/ square cm
$n_{surface}$	concentration of electrons at semiconductor surface
nvCPD	non-vibrating contact potential difference
N	number of adsorption sites
N_p	incident photon flux
N_T	volume density of R-G centers
osCPD	optically stimulated contact potential difference
π	geometric proportionality constant, Pi = 3.14159
Ψ	surface potential
p	hole density in semiconductor
p_o	equilibrium condition concentration of holes
q	fundamental unit of charge of an electron

q^*	total charge of a capacitor
Q_{SS}	magnitude of trapped charge at SI-SiO_2 interface
R	reaction rate in Arrhenius relation
R	ideal gas constant
R_n	percentage of incident light that is reflected
R_s	film resistance of a conductimetric sensor
R-G	recombination – generation centers
s_n	surface recombination velocity for electrons (cm / s)
s_p	surface recombination velocity for holes (cm / s)
Si	single crystal elemental silicon
SiO_2	silicon dioxide, also referred to as "oxide layer" or "native oxide"
SGFET	suspended gate field effect transistor
θ	fractional area of coverage of available adsorption sites
τ_n	characteristic electron lifetime (s)
τ_p	characteristic hole lifetime (s)
t	time in seconds (s)
T	temperature in degrees Kelvin (K)
v	linear velocity (m/s)
V	voltage in volts (V)
V_B	bias voltage
V_{CPD}	contact potential difference (volts - V)
V_D	drain voltage in MOSFET
V_G	gate voltage in MOSFET
V_{input}	voltage appearing at input to 1st stage CPD amplifier (volts – V)
V_n	thermal noise appearing at resistor (volts – V)
V^*_n	amplified thermal noise appearing in output signal (volts – V)
V_{osCPD}	final voltage signal recorded by data acquisition system
V_{PP}	peak-to-peak voltage of measured osCPD signal (volts – V)
V_S	source voltage in MOSFET (volts – V)
V_{signal}	output voltage signal from CPD amplification electronics (analog, V)
ω	frequency of oscillation (hertz – Hz)
ω_r	rotational speed
X	electron affinity in a semiconductor with respect to vacuum level
Xi	electron affinity in insulator with respect to vacuum level
z	height above hard disk surface in nvCPD measurement system

SUMMARY

This thesis addresses the development of a sensor to monitor chemical adsorption and charge transfer processes on a surface using a contact potential difference probe (CPD). The current investigation is an outgrowth of ongoing research in the Electronic Materials Lab at Georgia Tech on non-vibrating CPD probes (nvCPD). The work on nvCPD probes led to the recent development of a novel measurement technique utilizing optical stimulation: optically stimulated CPD (osCPD). Primary outcomes of this thesis are the theoretical modeling, fabrication and demonstration of a functional osCPD sensor. The research also involved significant engineering and experimentation in the design, development, and application of this sensor to oil condition monitoring.

This technique measures dielectric and chemical properties of a fluid at the interface between the fluid and a semiconductor substrate. Chopped visible light is used to stimulate the rear surface of a semiconductor substrate, and a CPD probe measures the work function response of the semiconductor on the front surface of the substrate. The work function response is influenced by the nature and quantity of adsorbed species on the front surface, allowing the probe to detect changes in chemical composition at the substrate/fluid interface.

A CPD probe was specifically designed and fabricated for this application, as was an integrated test fixture. It should be noted, however, that similar results were obtained

using a non-optimized CPD probe, thus indicating the robustness of the technique. As constructed, the test fixture was modular in design to allow continual development and refinement of the individual subcomponents of the osCPD test system.

An analytical model is developed that relates the osCPD sensor output signal to the chemical and dielectric properties of the oil sample, as well as to the geometry, composition, and control inputs of the silicon substrate and test fixture. The model is based on single-layer adsorption (Langmuir) of polar molecules on the front surface of the silicon substrate. The dipole moment of the adsorbate interacts with the space charge region in the silicon. The space charge region is modulated by minority carrier diffusion induced by the chopped light. When the light is on, a quasi-Fermi level is created in the silicon. The energy of the quasi-Fermi level is determined by the adsorbed layer of polar molecules. When the light is off, the silicon returns to the grounded (flat-band) state.

The modulated quasi-Fermi level at the front surface of the silicon induces an image charge at the surface of the CPD probe tip that is proportional to the energy of the quasi-Fermi level in the silicon. As the light is chopped, the quasi-Fermi level is modulated between a maximum steady-state value when the light is on, and a grounded state when the light is off. This drives the image charge in the CPD probe tip which results in an induced current in the probe tip. This probe tip current is converted to voltage and amplified by the CPD probe electronics. The final voltage output signal is acquired using a typical PC-based data acquisition system.

In this investigation, the osCPD sensor was used to evaluate dielectric and chemical properties of commercially available engine oil. Prime-grade Cz-silicon was used as the substrate. Oil samples were intentionally degraded through thermal aging (oxidation) and through addition of known contaminants. Changes in the chemical composition of oil were detected and quantified using the osCPD sensor, and these measurements are compared with other physical measurements of the oil. The osCPD sensor shows good sensitivity to depletion of antioxidants in the oil, as well as to the presence of ferric chloride, an oil-soluble salt typically used to calibrate laboratory test equipment. As tested in this investigation, the osCPD sensor exhibited a signal-to-noise ratio of 42dB with a predicted measurement resolution of 0.005eV with respect to the surface potential of the silicon substrate. It should be emphasized that these results are achieved in a relatively non-controlled lab environment at room temperature (as opposed to clean-room or high vacuum environments).

CHAPTER 1

INTRODUCTION

Relevance and Relation to Existing Fields of Study

The study of surfaces and their interaction with their environment is an increasingly important science. Many of the recent advances in the area of nano-technology are dependent upon knowledge of and control over surface interactions at a molecular scale. Measuring and modeling adsorption processes at interfaces has been an active area of research since the beginning of the previous century[1]. The measurement and monitoring of adsorption processes is an interdisciplinary science, often involving teams of chemists, physicists, biologists, and engineers. Adsorption plays an extremely important role in industrial, environmental and biological processes. Endpoint detection in manufacturing processes is frequently based on measurement of the change in concentration of components at an interface. Purification and measurement of water, sewage, and effluents are also processes involving adsorption or that can be monitored by measuring adsorption and surface interactions. Sensors capable of measuring surface interactions are crucial tools to researchers and engineers alike. It is therefore not surprising that sensor development in and of itself is such an active area of current research[2]. This thesis develops a new sensor, the optically-stimulated contact potential difference sensor (osCPD sensor). The sensor is shown to be capable of monitoring adsorption processes and charge interactions at a semiconductor surface in non-laboratory conditions (many Kelvin probe systems require ultra-high vacuum environments in order to obtain

repeatable results). The chosen application focus for the current study was engine oil degradation, but the fundamental technique is more broadly applicable to dielectric fluids in general. This introductory chapter will present a high-level survey of adsorption sensor technology, and a more detailed discussion and comparison of existing technologies that share similarities with the current research.

There are numerous techniques and experimental procedures for studying liquid adsorbates at solids interfaces. A representative survey of methods for studying the adsorption from fluid solutions onto solids includes IR, visible and UV spectroscopic techniques, magnetic resonance, ellipsometry, and radioactive tracer methods. Most of these techniques are suitable for use only in the laboratory due to the expense or size of the associated measurement equipment.

A newer and rapidly evolving category of adsorption-sensitive devices is semiconductor-based sensors. A sensor is broadly defined as a device that converts non-electrical input stimulus such as temperature or vibration into an electrical output signal. Semiconductor-based chemical sensors with possible applications in adsorbate detection can be classified according to the principle measurand or input signal as conductimetric, potentiometric, calorimetric, coulometric, and mechanical sensors[3]. What follows is a brief description and example of conductimetric and potentiometric sensors since these device types are most similar to the osCPD sensor. The osCPD sensor is fundamentally a potentiometric device. A more detailed discussion of other potentiometric devices as well as comparison and contrast with the osCPD sensor follows later in this section.

Conductimetric sensors

Conductimetric sensors measure a change in the electrical resistance of a material in the presence of a target gas adsorbate[4]. Semiconducting metal oxides such as SnO_2 are frequently used as the resistive element in such devices. A layer of SnO_2 is placed on a non-conducting, heated substrate. Sintering the SnO_2 at high temperature in an oxygen environment leads to adsorption of oxygen. The adsorbed layer creates a surface potential on the SnO_2 which in turn creates a potential barrier at grain boundaries. Each end of the film is connected to a resistance measurement circuit by electrodes. Reduction reactions consume the adsorbed oxygen. This depletion can be detected as a change in resistance. The relationship between the measured resistance of the film and gas concentration is given by:

$$R_s = A[C]^{-\gamma} \tag{1.1}$$

Where

A is a constant determined by the measurement electronics

C is the adsorbate concentration, and

γ is an empirical constant based on SnO_2 structure and the adsorbate.

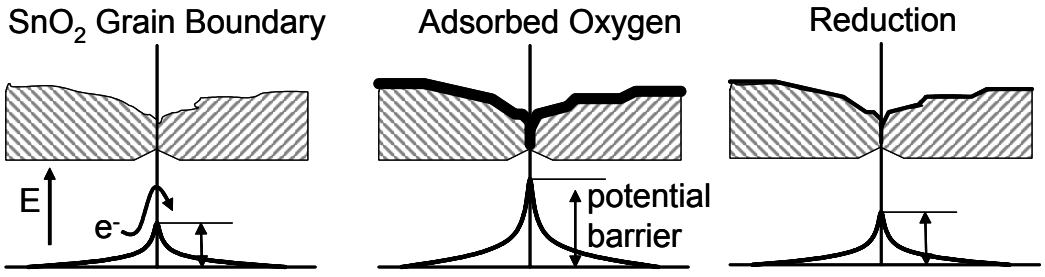

Figure 1-1: Schematic diagram of typical conductimetric sensor

Potentiometric sensors

It has been observed that Metal Oxide Silicon Field Effect Transistors (MOSFETs) are the most numerous man-made objects in history. They form the basis of nearly all electronic devices, and have undergone decades of intense development and refinement. More recently, the basic operating principles and processing technology of the MOSFET have been employed in developing a variety of chemical sensors. One of the first demonstrations of such a sensor was an ion-sensitive FET as described by Bergveld[6] in 1970. In 1975, Lundstrom[7] et al. demonstrated the Pd-gate MOSFET, a device sensitive to the presence of hydrogen. As illustrated in Figure 1-2, the Pd-gate MOSFET is fundamentally identical to a typical MOSFET with the key difference being the composition of the gate metal. As the name implies, in a Pd-gate MOSFET, palladium replaces the more typical aluminum as the gate metal.

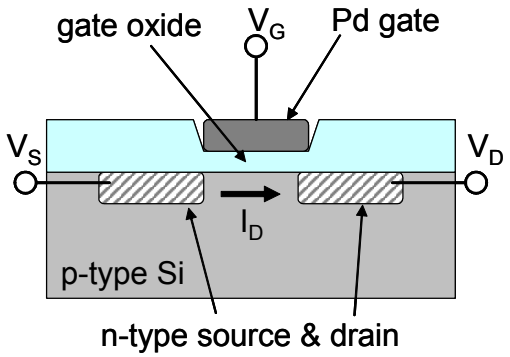

Figure 1-2: Schematic illustration of Pd-gate MOSFET

As in a typical MOSFET, a bias voltage applied between the source and drain (V_D-V_S) results in a drain current, I_D. The drain current can be modulated by applying a voltage bias to the gate, V_G. The applied gate voltage induces a field (the "field effect") in the

surface region between the source and drain (the channel). The effect of this field is to change the carrier concentrations in the channel, and thus modulate the conductivity of the channel. As the conductivity changes, so does the drain current.

Due to the difference in work function (discussed in more detail in Chapter 2) between palladium and silicon, there is a field present even in the absence of an applied gate voltage (i.e. when $V_G = 0$). This results in a surface charge on the palladium gate, and an induced space charge region (SCR) in the silicon. Palladium is permeable to hydrogen. Hydrogen atoms that are adsorbed onto the top surface of the Pd gate diffuse through the bulk material and adsorb to the bottom surface of the gate. The adsorbed layer of hydrogen at the palladium-silicon oxide interface modifies the work function of the palladium, which in turn modifies the field in the silicon. This can be detected as a change in the drain current, I_D, through the channel.

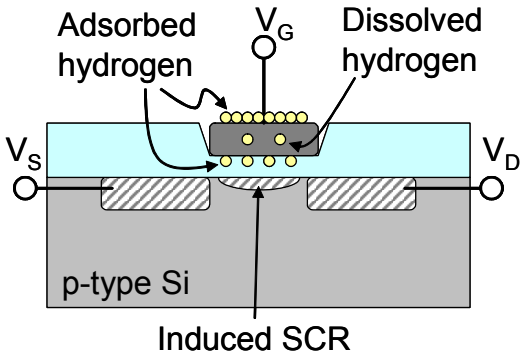

Figure 1-3: Schematic diagram illustrating functionality of Pd-gate MOSFET

As initially constructed, the Pd-gate MOSFET was limited to detection of hydrogen. However, subsequent development has led to the use of discontinuous thin films that are

composed of materials other than palladium. These ultra-thin layers are permeable to, and therefore sensitive to, a broader array of gases[3] (e.g. ammonia, ethanol, etc.). More recently, Hatfield at al. successfully demonstrated the use of polypyrrole (PPy), a conductive polymer, as the gate material[9]. This will likely open the door to a yet wider range of adsorbed species that can be detected.

The MOSFET devices described to this point are limited in application by the need for the analyte to diffuse through the gate material before being sensed. A method that removes the limitations imposed by diffusion through the gate material was developed by Janata et al. As illustrated in Figure 1-4, the suspended gate FET (SGFET) separates the gate metal from the gate insulator by a small gap.

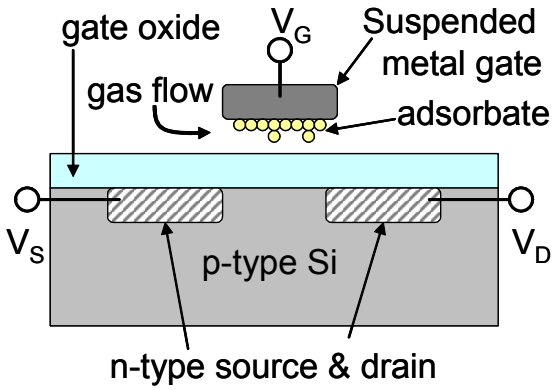

Figure 1-4: Schematic diagram of a suspended gate FET (SGFET)

In this configuration, the SGFET is amenable to detection of much broader range of gaseous species. Tailored coatings on the suspended gate also provide a path for selective response.

LAPS Sensors

The light-addressable potentiometric sensor is based on the metal-insulator-semiconductor structure (MIS). It is typically used to make pH and redox potential measurements of electrolytic liquids[10]. The typical LAPS metal-insulator system is comprised of either an n-type or a p-type silicon substrate with a silicon oxynitride insulator on the top surface. As shown in Figure 1-5, rather than a metal electrode deposited directly on the insulator surface as in the case of a MIS-capacitor or a metal gate as in the case of the MOSFET, the LAPS technique utilizes a metal electrode immersed in a catalytic fluid which is contained on the surface of the silicon oxynitride.

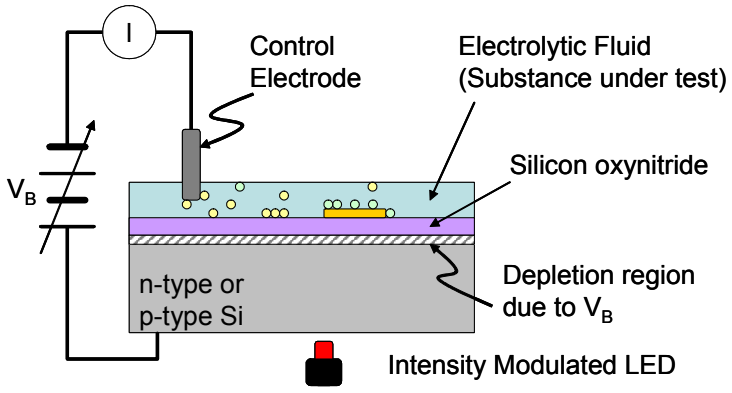

Figure 1-5: Schematic illustration of Light Addressable Potentiometric Sensor (LAPS)

The catalytic fluid is both a necessary signal path, and is also the substance under test. The electrode is electrically connected to the back surface of the silicon, and a bias voltage, V_B, is applied. The effect of the bias voltage is to create a depletion region in the top surface of the silicon at the silicon – silicon oxynitride interface. An intensity modulated light is used to illuminate either the front or back surface of the silicon. Due to the application of the bias voltage, an AC photocurrent develops in the depletion region. The amplitude of the photocurrent is a function of the applied bias, the light intensity, and surface potential of the insulator.

osCPD Sensor

The osCPD sensor is, fundamentally, a field-effect device. Unlike the MOSFET or the LAPS, however, the osCPD sensor does not utilize an applied voltage to modulate the silicon response. As shown in Figure 1-6, in the osCPD sensor a CPD probe is suspended above a silicon substrate. The silicon has a native oxide, grown at room temperature after etching in HF. As a result of this method of substrate preparation, there is a substantial trapped charge at the interface between the Si and SiO_2. The charge is large enough in magnitude to induce a static depletion region in the top surface of the Si substrate.

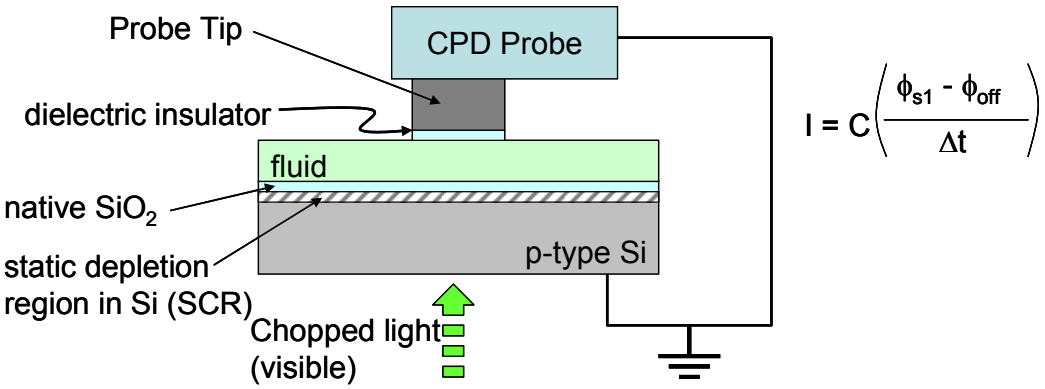

Figure 1-6: Schematic illustration of optically stimulated CPD sensor (osCPD)

The photovoltaic effect in silicon creates a quasi-Fermi level when the light is turned on. The steady-state value of the quasi-Fermi level depends on the intensity of the light, and the static depletion region. When the light is turned off, the silicon returns to the flat band state. An image charge exists on the surface of the CPD probe tip that is proportional to the quasi-Fermi level at the silicon surface. As the light intensity is modulated, the time-varying induced charge generates a current in the CPD probe tip. This current is amplified to produce the output voltage signal.

As is known for MOSFETs and LAPS, the chemical state of the oxide surface influences the work function of either the gate metal (as in MOSFETs) or the silicon substrate (as in LAPS). In the osCPD sensor, the SCR in the silicon is affected by the surface state of the SiO_2. Adsorbed dipoles alter the static (flat-band) value of the SCR in the silicon. This in turn results in a modification of the quasi-Fermi level attained when the light is turned on. Therefore, adsorption of dipole molecules on the surface of the $Si0_2$ results in a measurable change in the light-induced quasi-Fermi level of the silicon.

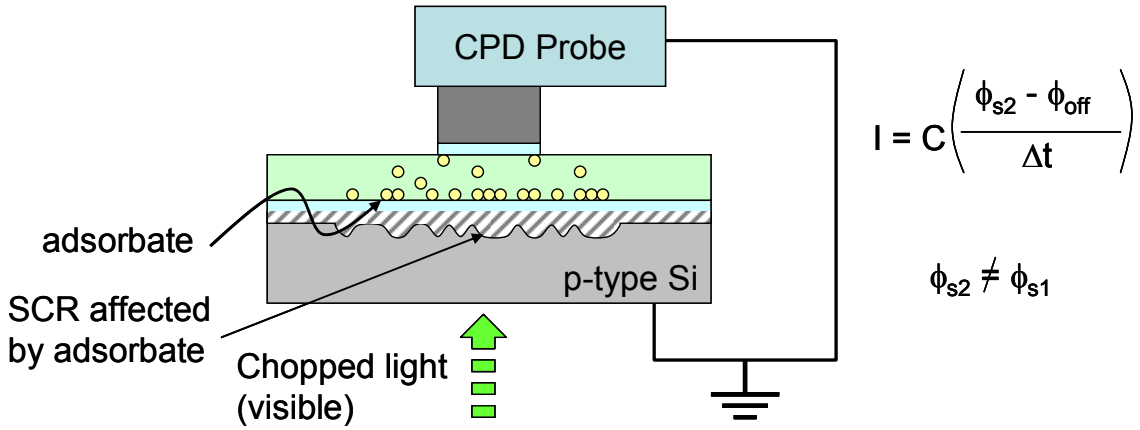

Figure 1-7: Schematic illustration of functionality of osCPD sensor

Comparison of Figures 1-6 and 1-7 shows that the mechanism for signal generation is the effect of the adsorbate on the quasi-Fermi level at the front surface of the silicon substrate. The change can be detected as a change in surface potential when the surface potential is modulated by the chopped light. As a silicon-based sensor, the osCPD sensor shares many of the fundamental device physics with the MOSFET class of sensors and the LAPS sensor. While there are many similarities, there are also substantial differences. Table 1-1 contains a comparison of the osCPD sensor with MOSFETs and LAPS.

Table 1-1: Key features comparison of the osCPD probe, LAPS, and MOSFET sensors

	osCPD	**LAPS**	**MOSFET**
Principle Measurand	F_N – quasi-Fermi level	AC photo-current	Drain Current
Chemically Sensitive Layer	Native SiO_2 on Si substrate	$SiNO_x$ and tailored surface chemistries	Gate metal
Signal stimulus	Chopped light	Chopped light and applied bias	Applied bias (source, gate, and drain voltages)
Device architecture	MIS-C + CPD	MIS-C	MOSFET (+CPD for SGFET)
Output Signal path	Restricted to Probe Tip and amplifier	Through electrolyte (sample)	Source-drain channel
Gases	Yes	No	Yes
Conductive Liquids	Yes	Yes	No
Dielectric Liquids	Yes	No	Yes

Initial osCPD Application: Oil Condition Measurement

In-situ condition monitoring of lubricating oil is another active area in terms of current research and development of sensors. Proper lubrication of moving components in machinery is an important problem. It is estimated that up to 70% of machine failures are due to surface degradation of moving components, and a substantial majority of these failures are related to lubrication[11]. Knowledge of the condition of a lubricant is, therefore, critical in assessing machine condition, and in preventing machine failure.

Increasing costs of capital equipment and competitive market pressure drive the need to maximize machine uptime. Machine failure due to catastrophic lubricant failure can be costly if the machine in question is on a production line, and can be fatal in the event of

aircraft engine failure. There is a trend among forward looking companies to move from reactive/ repair-based maintenance to routine scheduled maintenance and beyond to pro-active/ preventive maintenance. One frequently employed tactic is for plant engineers to obtain oil samples from critical machinery at prescribed intervals. The oils samples are sent to a central analysis laboratory which is frequently an external vendor. The results of the analysis are then sent back to the customer, along with recommendations for any corrective actions. The total cycle between drawing an oil sample and receiving analysis results typically takes at minimum several days, and can even take several weeks. Although the intent of drawing and measuring the samples is to prevent catastrophic failure by monitoring trends in the oil measurements, there is still the potential for the sudden onset of catastrophic failure of the engine oil during the interval between sampling and return of results. Such sudden onset failures are frequently the result of a mechanical failure. For example, a broken seal can result in leakage of coolant fluid into the oil or the ingress of foreign debris.

There is a need for in-situ oil condition monitoring sensors. Companies are currently developing such sensors with technologies ranging from viscometers to dielectric spectrometers. This thesis develops a new sensor, the optically-stimulated contact potential difference sensor (osCPD sensor) that is capable of detecting changes in oil condition, and may have the possibility for commercial development and productization.

CHAPTER 2

THEORETICAL BACKGROUND & LITERATURE SURVEY

This chapter reviews the basic operating principles of the osCPD sensor. The sensor is an integration of several established fields of investigation. As shown in Figure 2-1, these fields include silicon device physics and the photovoltaic effect, the Kelvin probe (or CPD probe), and adsorption and its effect on work function. This chapter will review these fundamental building blocks and will integrate these to form a predictive model of the osCPD sensor. In the process, this chapter will also present a brief historical review of the scientific research of the past century that laid the foundation for the development of the osCPD sensor.

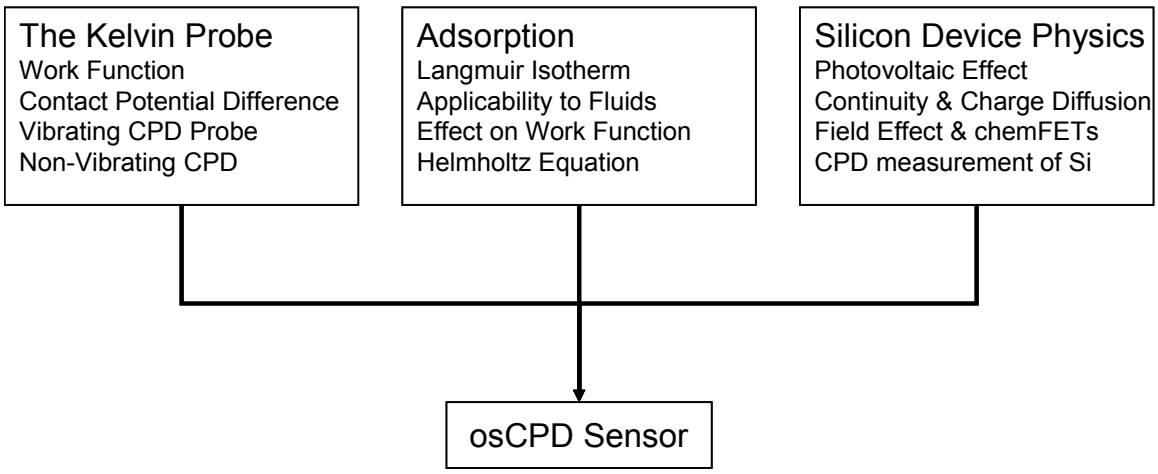

Figure 2-1: Primary constituents of osCPD sensor theory of operation

Work Function

The work function ,Φ, of a material is the minimum work required to move an electron from a point in the bulk of the material to a point outside the surface of the material where it is free of the electrostatic influence of the surface[12] (to a "vacuum level"). Due to the physical discontinuity created by the interface between the surface and the surrounding vacuum, a surface dipole, Ψ, always exists at the phase boundary. Thus, the work function of a material can be visualized as the difference between the Fermi energy, E_F and the vacuum level, plus the energy required to overcome the surface dipole Ψ. The Fermi energy represents the represents the energy of the highest filled energy level in the conduction band of the metal. This idealized definition of work function is given for conditions that exist at zero degrees Kelvin.

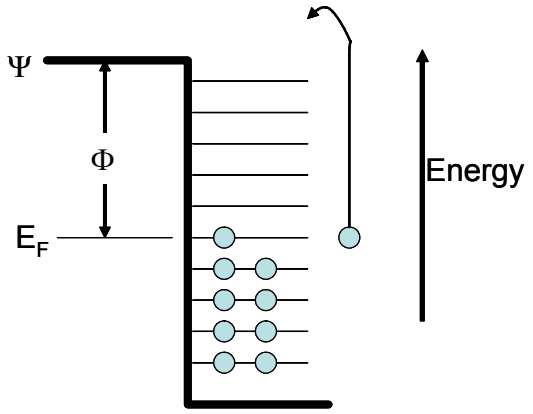

Figure 2-2: Schematic of work function and Fermi energy in metal

Contact Potential Difference

Contact potential difference refers to voltage potential that develops at an interface between dissimilar materials held in close proximity and electrically connected at a region away from the interface in question. As illustrated in Figure 2-3, a contact

potential difference is created when a transient current is allowed to flow between the dissimilar materials to equilibrate the Fermi energies of the two materials. The contact potential difference is related to the work function of the two materials by

$$V_{CPD} \propto \frac{\Phi_1 - \Phi_2}{|e|} \tag{2.1}$$

Where

e = 1.6 x 10^{-19}C is the unit of charge of an electron.

As a result of the transient current flow, equal and opposite charges are created on the opposing surfaces, and an electric field is developed in the gap between the surfaces. The potential developed is related to the work function of the two materials. The total charge transfer is related to the difference in voltage of the surfaces by

$$q = CV_{CPD} \tag{2.2}$$

Where

C is the capacitance formed by the surfaces.

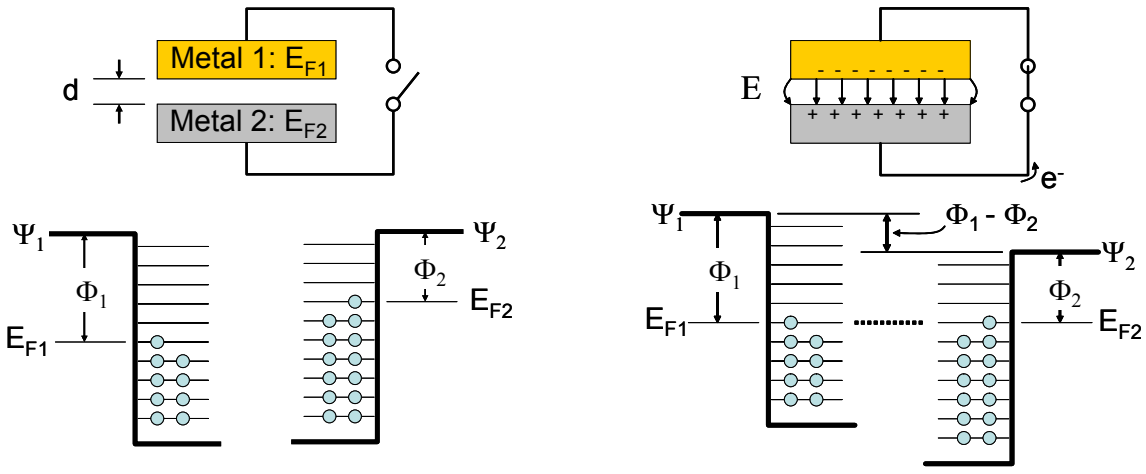

Figure 2-3: Schematic of contact potential difference

For a parallel plate capacitor in which each of the two surfaces is homogeneous and separated by a uniform dielectric material, the capacitance can be calculated as

$$C = \frac{\varepsilon_r \varepsilon_o A}{d} \tag{2.3}$$

Where

$\boldsymbol{\varepsilon_o}$ = 8.85 x 10^{-14} F/cm is the permittivity of free space,

$\boldsymbol{\varepsilon_r}$ is the relative dielectric constant of the gap material between the plates,

A is the surface area common to both plates, and

d is the gap between the plates.

The Kelvin Probe

Description of the phenomenon of contact potential difference is often attributed to Lord Kelvin (although similar work was previously performed by other investigators, including Pellat). In a paper published in 1898, Kelvin described using a gold leaf electrometer to measure surface charges that were generated by placing parallel plates of dissimilar metals in close proximity to each other, and then making a temporary electrical contact between the plates[13]. When the contact was removed, the deflection of the leaves remained, indicating that charge had been transferred between the dissimilar metals.

The Vibrating CPD Probe

Lord Kelvin's observation was transformed into a practical measurement technique in 1932 by Zisman[14]. As illustrated in Figure 2-4, Zisman's system was essentially a parallel plate capacitor in which one of the plates was held stationary, and the other was vibrated in close proximity to the fixed plate.

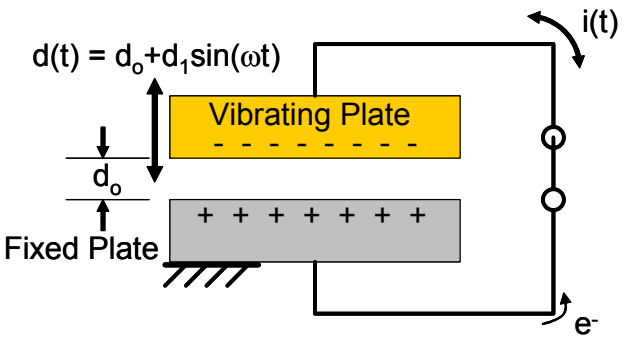

Figure 2-4: Schematic of Vibrating CPD Probe

The two plates were fabricated of dissimilar metals so that as described previously, a contact potential difference was developed. The vertical vibration of the top plate resulted in a periodic change in capacitance between the plates given by

$$C(t) = \frac{\varepsilon_r \varepsilon_o A}{d(t)} \tag{2.4}$$

In which

$$d(t) = d_o + d_1 \sin \omega t \tag{2.5}$$

Here,

ω is the frequency of oscillation,

d_0 is the mean gap height, and

d_1 is the amplitude of vibration.

Zisman's measurement system, often referred to as the Kelvin-Zisman probe, employed a circuit similar to the one illustrated in Figure 2-5. The current generated by vibrating the two plates was measured using an electrometer. By applying a voltage bias, V_B, in

parallel with the capacitor plates, the current could be nullified, thus indicating the contact potential difference between the metal plates.

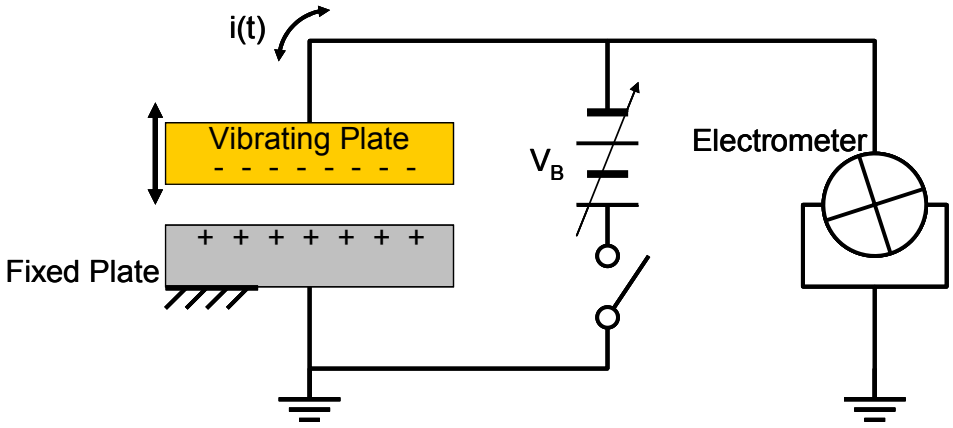

Figure 2-5: Schematic of Zisman's detection circuit

In the system shown in Figure 2-5, a current is developed in the connecting wire that is proportional to the time rate of change of charge in the capacitor:

$$i(t) = \frac{\partial q}{\partial t} \tag{2.6}$$

Partial derivatives are indicated here solely to avoid confusion in nomenclature with the gap height, d. Combining Equation 2-2 and Equation 2-6 yields

$$i(t) = \frac{\partial \left(C V_{CPD} \right)}{\partial t}. \tag{2.7}$$

Differentiating, one obtains

$$i(t) = C \frac{\partial V_{CPD}}{\partial t} + V_{CPD} \frac{\partial C}{\partial t}. \tag{2.8}$$

If the measurement is made at a specific location with respect to the fixed plate, and if environment is not affecting the work function of either the surfaces,

$$\frac{\partial V_{CPD}}{\partial t} \to 0. \tag{2.9}$$

Combining Equations 2-4, 2-5, and 2-8, the current can be expressed as

$$i(t) = V_{CPD}\frac{\partial C}{\partial t} = \left(\frac{\Phi_1 - \Phi_2}{|e|}\right)\frac{\partial}{\partial t}\left(\frac{\varepsilon_o \varepsilon_r A}{d_0 + d_1 \sin \omega t}\right). \tag{2.10}$$

Thus it can be seen that the fundamental mechanism driving the signal is vibration of the top plate. It can also be seen that the generated signal current is proportional to the difference in work function of the metals is proportional to the shared area of the surfaces, and is inversely proportional to the gap separating the plates.

The concepts developed to this point can be extended to a system in which the stationary lower plate is replaced by a target or surface to be investigated, and the vibrating top plate is replaced by a smaller probe tip. Such an arrangement is shown in Figure 2-6. As before, signal generation is given by

$$i(t) = C\frac{\partial V_{CPD}}{\partial t} + V_{CPD}\frac{\partial C}{\partial t} \tag{2.11}$$

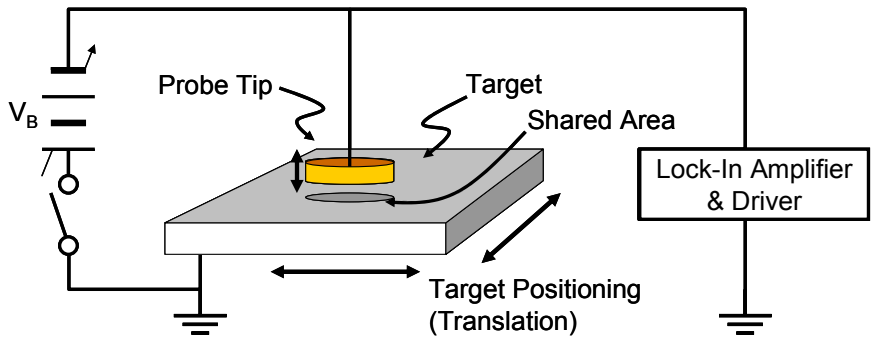

Figure 2-6: Schematic of typical CPD measurement system

Although the measurement technique and resolution were refined over the following decades and applied to numerous material systems, the basic principle of operation remained the same[15, 16, 17].

Non-Vibrating CPD

Work on non-vibrating contact potential difference techniques (nvCPD) has been conducted in the Electronic Materials Research Lab at Georgia Tech since 1995[18-22]. As illustrated in Figure 2-7, the nvCPD signal is generated by the relative motion of the system under investigation with respect to the CPD probe tip. In the example shown, a bi-metallic plate is translated back and forth under the probe tip (conversely, the probe tip could be scanned in a raster pattern over the surface). As the probe tip passes over the boundary between the two metals, the work function changes. Therefore, the contact potential difference, V_{CPD}, between the probe tip and the target is a function of position.

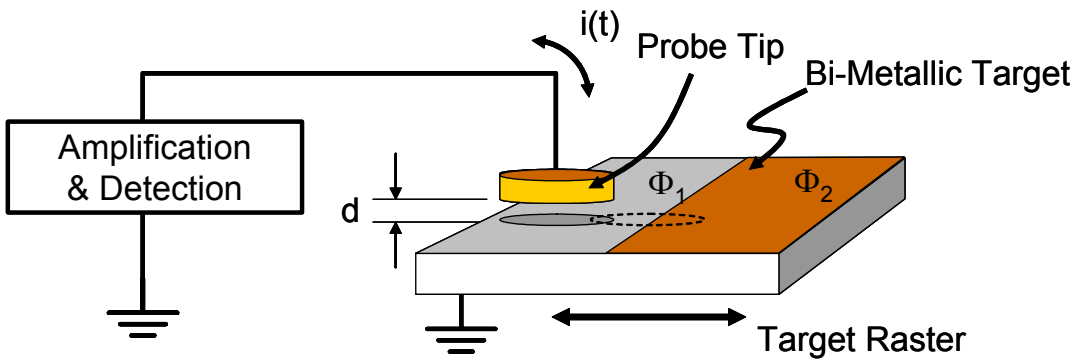

Figure 2-7: Schematic of nvCPD measurement system

Assuming a constant probe-to-target gap or "fly height", the capacitance remains constant as a function of position, and therefore is also constant as a function of time as the target is scanned. In this case, Equation 2-11 reduces to

$$i(t) = C\frac{\partial V_{CPD}}{\partial t} \tag{2.12}$$

If we take Φ_T as the work function of the probe tip, then the contact potential difference between the probe tip and the target metals can be expressed as

$$V_{CPD-1} = \frac{\Phi_T - \Phi_1}{|e|} \tag{2.13}$$

$$V_{CPD-2} = \frac{\Phi_T - \Phi_2}{|e|} \tag{2.14}$$

Where Φ_1 and Φ_2 are the work functions of *metal-1* and *metal-2*, respectively. As the probe tip passes over the interface between *metal-1* and *metal-2*, the contact potential difference between the probe tip and the target changes from V_{CPD-1} to V_{CPD-2}. The time rate of change of the contact potential difference is dependent on the relative velocity between the probe tip and the target, and can be expressed as

$$\frac{\partial V_{CPD}}{\partial t} \cong \frac{\Delta V_{CPD}}{\Delta t} = \frac{V_{CPD-1} - V_{CPD-2}}{\Delta t} \tag{2.15}$$

Inserting Equations 2-13 and 2-14 yields

$$\frac{\partial V_{CPD}}{\partial t} \cong \frac{1}{|e|}\left(\frac{(\Phi_T - \Phi_1) - (\Phi_T - \Phi_2)}{\Delta t}\right) = \frac{(\Phi_2 - \Phi_1)}{|e|\Delta t} \tag{2.16}$$

The resulting current in the probe tip is given by

$$i(t) = C \cdot \frac{(\Phi_2 - \Phi_1)}{|e|\Delta t} \tag{2.17}$$

It is important to note that in this configuration, the work function of the probe tip itself, Φ_T, does not contribute to the final signal. A similar lack of dependence of the output signal with respect to the probe tip work function will later be shown for the osCPD sensor.

Adsorption – The Langmuir Isotherm

Over the past century, many models have been developed to describe the steady state characteristics of adsorbed layers as well as the molecular dynamics of formation of adsorbed layers. One of the most widely employed models for adsorption is the Langmuir Isotherm. In 1918, Langmuir published a paper on experiments he conducted on the adsorption of gas molecules to mica, glass, and platinum[23]. Based on the results of these experiments in combination with kinetic models of gas molecule/ surface interactions, Langmuir developed the relationship

$$\theta_1 = \frac{\alpha_1 \mu_1}{(\upsilon_1 + \alpha_1 \mu_1)} \tag{2.18}$$

Where

θ_1 is the fractional coverage of the adsorbed molecule with respect to available adsorption sites ("elementary spaces").

α_1 is the fraction of molecules striking the surface that adhere or condense

ν_1 is the fraction of molecules striking the surface that immediately evaporate

μ_1 is the number of gram-molecules striking the surface per square cm per second

Here, μ_1 is a function of pressure and temperature as well as of molecular size. Higher pressures, higher temperatures, and lower molecular weights would increase μ_1.

This relationship for fractional coverage can be expressed in an equivalent form as

$$\theta = \frac{KC}{(1+KC)} \tag{2.19}$$

where,

θ is the fractional area of surface coverage

. **C** is the molar concentration of adsorbate species, and

K is the reciprocal of the adsorption equilibrium constant, i.e.

$$\frac{1}{K} = \exp\left(-\Delta GA\ /RT\right) \tag{2.20}$$

in which

ΔGA is the standard adsorption free energy,

R is the gas constant, and

T is the absolute temperature.

In simplest terms, the fractional area of coverage of the adsorbed species is a function of the concentration of the species present in the region of the surface, the environmental conditions (i.e. temperature and pressure), and the particular surface affinity of the adsorbate.

Effect of Adsorption on Work Function - The Helmholtz Equation

In 1931, Schulman and Rideal reported on experimental measurements of the effect of unimolecular films on surface potentials[24, 25]. Their apparatus, shown schematically in Figure 2-8, consisted of a glass trough filled with water. A film was placed on the water, and the surface potential was measured using an electrometer.

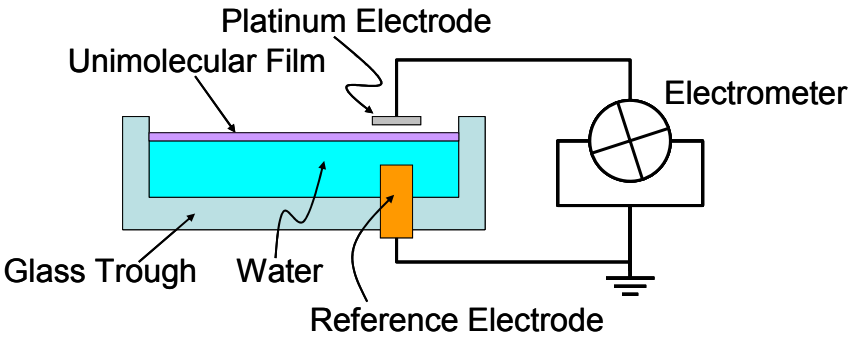

Figure 2-8: Schematic of measurement apparatus used by Schulman and Rideal

Schulman and Rideal[24,25] observed a change in surface potential due to the presence of the unimolecular film. They concluded that the change in potential followed the relationship given by Helmholtz as

$$\Delta\Phi = 4\pi n\mu_p . \tag{2.21}$$

Where

$\Delta\Phi$ = the change in surface potential at the interface

n = the number of adsorbed molecules/ square cm of the film forming adsorbate,

μ_p = the perpendicular component of the dipole moment of the adsorbate.

Although these experiments were conducted on unimolecular adsorption layers at a liquid-liquid phase boundary, work by later authors would confirm the applicability of the Helmholtz equation to gas-solid and liquid-solid phase boundaries as well as multi-layer adsorption processes.

Vibrating CPD Measurement of Gas Adsorption

Both vibrating and non-vibrating CPD probes have been used to measure adsorption. In 1951, Phillips described a method to detect impurities in air using a modified Kelvin-Zisman probe[26]. A schematic diagram of the system is shown in Figure 2-9. A voltage bias, V_B, was applied to nullify the signal generated by the system in ambient air flowing over a prepared stainless steel surface. Pulsed doses of various vapors including ethyl alcohol, acetone, and amyl acetate were then introduced individually into the air flow. The resulting transient response was captured and analyzed.

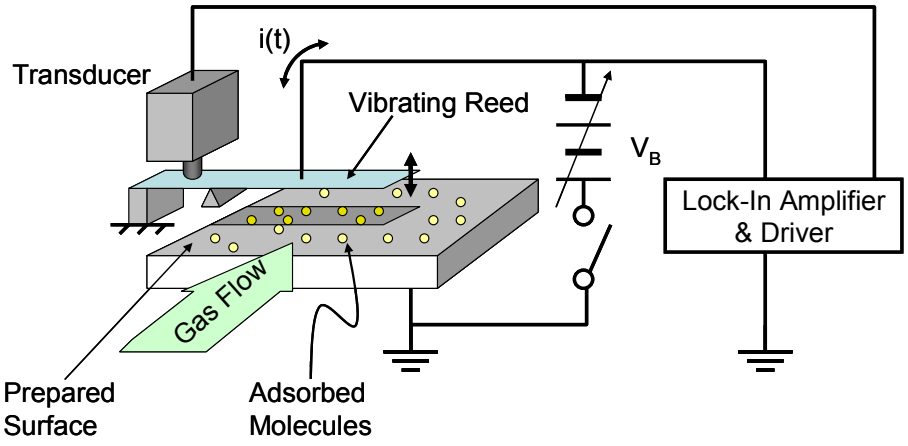

Figure 2-9: Schematic of vibrating CPD adsorption measurement system[26]

Phillips employed the Helmholtz equation in analyzing his results. He noted that the change in potential due to adsorbed alcohol was approximately 10^4 times greater than the change in potential due to adsorbed benzene due to the difference in dipole moments and to differences in numbers of adsorbed molecules of each species. His experimental results for chloro-acetate gas in air are shown in Figure 2-10.

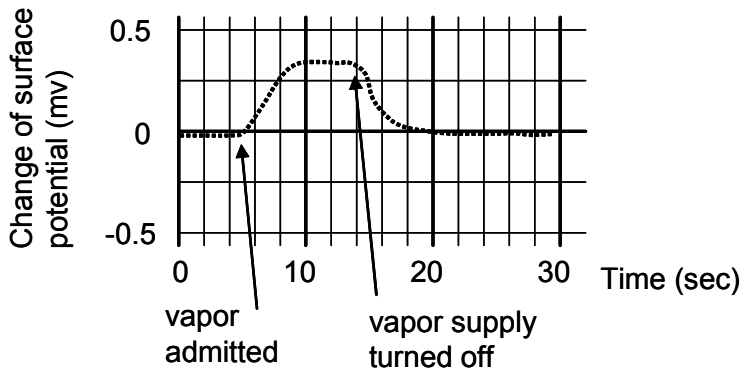

Figure 2-10: Reproduction of Phillips' CPD measurements of adsorption-desorption[26]

In this experiment, 5 ppm by weight chloro-acetate was injected into the gas flow. Adsorption of chloro-acetate gas caused the indicated change in surface potential. When the chloro-acetate flow was turned off, the adsorbed layer evaporated from the surface, and the surface potential returned to its original state. The short time constants and lack of significant hysteresis suggest that the process was one of pure adsorption, as opposed to a combination of adsorption and chemical reaction. As shown in figure 2-11, the data also showed that absorption of specific species from a gas mixture could be adequately modeled using the Langmuir Isotherm.

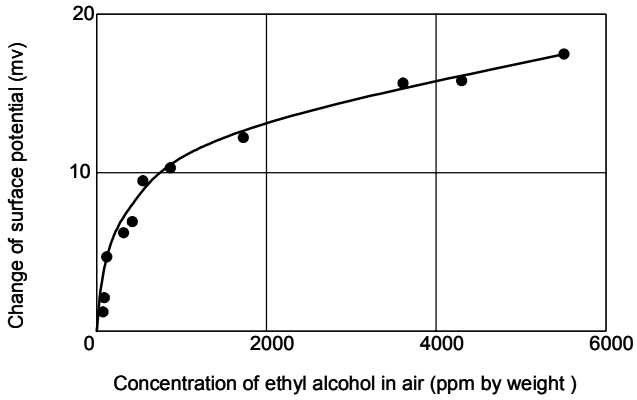

Figure 2-11: Reproduction of Phillips' CPD measurements of adsorption isotherm[26]

Vibrating CPD Measurement of Single-Phase Liquid Adsorption

In 1964, Bewig and Zisman[27] reported on an extensive study of adsorption of liquids on metal surfaces. The study measured a change in surface potentials due to adsorption using a vibrating CPD probe system similar to those already discussed. As indicated in Figure 2-12, a pure gold disc was used as the vibrating electrode, and a variety of other metals were used for the target electrode, including platinum, gold, chromium, nickel, tungsten, and copper. In this and other adsorption studies[28], there was good agreement with the Helmholtz equation in terms of predicting the change in surface potential caused by adsorption. This study also showed that the Langmuir Isotherm could be used to adequately describe the adsorption of liquids onto a solid surface.

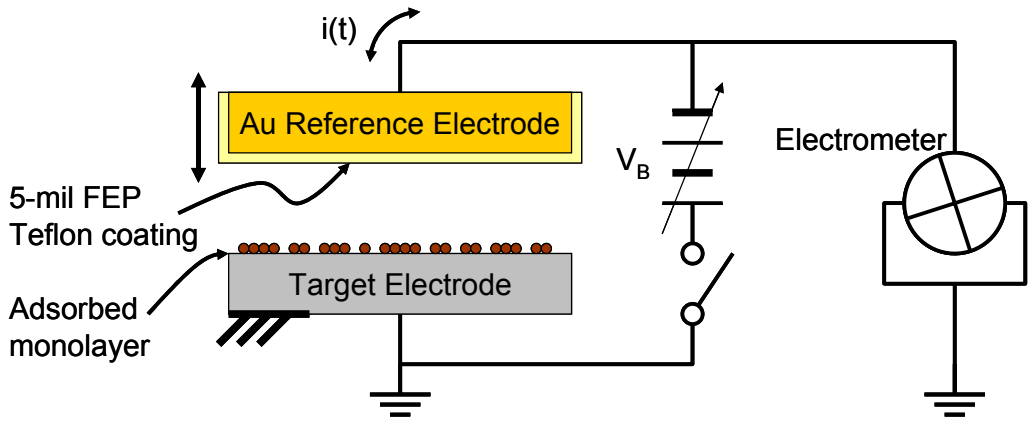

Figure 2-12: Schematic of Bewig-Zisman apparatus for measuring adsorption[27]

One group of adsorbates studied was comprised of a homologous family of n-alkanes. A portion of these results is shown in Table 2-1. A key finding of their work was that within the degree of certainty, the measured change in work function, $\Delta V_{CPD,}$ for the homologous group of adsorbates did not vary with the number of carbon atoms in the

Table 2-1: Bewig-Zisman Measured change in contact potential due to adsorption[27]

Adsorbed Compound	ΔV_{CPD}
n-Hexane	0.215
n-Octane	0.220
n-Decane	0.220
n-Dodecane	0.205
n-Tetradecane	0.210
n-Hexadecane	0.215

associated hydrocarbon molecule. This suggests that the effect on work function due to adsorption is dominated by the polar end-groups, and not by the hydrocarbon "tail". This concept is schematically illustrated in Figure 2-13. Molecules *A* and *B* have equivalent dipole moments in their polar end groups, and thus equivalent changes in work function, independent of their associated molecular chains. Molecules *B* and *C* have different dipole moments in their polar end-groups, and thus lead to different changes in work function even though their associated molecular weights are equivalent.

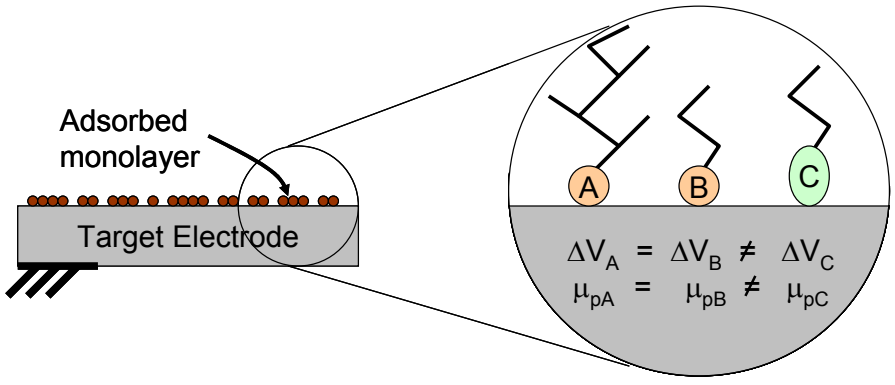

Figure 2-13: Schematic illustrating change in surface potential based on polar end-group.

Vibrating CPD Measurement of Liquid Adsorption from Solution

In 1992, Beltzer reported on a study of adsorption of long-chain friction modifying molecules[29]. Beltzer used a vibrating CPD system to make measurements of the adsorption of long-chain molecules from hydrocarbon solutions onto a metal surface. Beltzer noted that while absolute values of surface potential cannot be measured using this approach, the change in contact potential difference can be measured with good repeatability. He found the signal generated to be due to the change in contact potential difference by

$$i(t) = V_{CPD} \frac{\partial C}{\partial t}. \tag{2.22}$$

For a system in equilibrium, all of the terms in equation 2.22 are constant in magnitude. However, after addition of friction modifying molecules, V_{CPD} changes due to the effect of adsorption on surface potential according to the Helmholtz equation. The Helmholtz equation can also be expressed as

$$\Delta\Phi = \frac{\mu_p N}{\varepsilon_0 \varepsilon_r} \theta \tag{2.23}$$

Where

N is the number of adsorption sites

$\boldsymbol{\varepsilon_o}$ = 8.85 x 10-14 F/cm is the permittivity of free space

$\boldsymbol{\varepsilon_r}$ is the relative dielectric of the adsorbate, and

$\boldsymbol{\theta}$ is the fractional area of surface coverage (same as Langmuir Isotherm).

For analysis of experimental data, Beltzer simplified this relation to

$$\Delta\Phi = k\theta . \tag{2.24}$$

He next combined the simplified Helmholtz equation with the Langmuir isotherm to obtain:

$$\Delta\Phi = k\frac{KC}{(1+KC)} \tag{2.25}$$

This equation predicts a change in work function due to adsorption, where the number of adsorbed molecules is a function of the concentration of these molecules in solution. Evaluating his results using the combined Langmuir-Helmoltz equation, Beltzer confirmed the predicted change in measured work function based on the concentration of additive in the hydrocarbon solution. A key observation is the applicability of the Langmuir isotherm to complex liquid systems, rather than the single-species gas relationship it was originally created to describe. This study showed that the Langmuir Isotherm could be used to adequately describe the adsorption of liquids from complex solutions onto a solid surface.

Non-Vibrating CPD Measurement of Single-Phase Adsorption

In 1999 and again in 2001, Korach, Streator and Danyluk reported on the use of a non-vibrating CPD probe to measure lubricant thin films on hard drive surfaces[30, 31]. The experimental apparatus used is illustrated schematically in Figure 2-14.

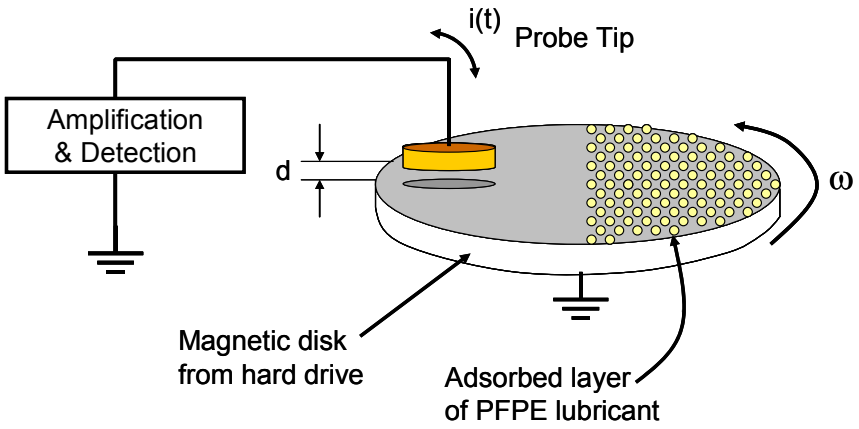

Figure 2-14: Schematic of adsorption measurement using nvCPD system

A hard disk from a magnetic storage drive was selectively coated with an adsorbed layer of PFPE lubricant. The disk was rotated at high speed, leading to a relatively large velocity between the probe tip and the disk surface. As the boundary between the coated and uncoated regions of the disk passed beneath the probe tip, a signal was created in an analogous fashion previously described for a bi-metallic disk:

$$i(t) = C \cdot \frac{\left(\Phi_2 - \Phi_1\right)}{|e|\Delta t}. \tag{2.26}$$

Once again, the work function of the probe tip itself, Φ_T, does not contribute to the final signal. As given in Equation 2-27, a modified version of the Helmholtz equation was employed to calculate the dipole moment of the film, and the surface charge density based on the measured signal.

$$\Delta\Psi = \frac{\mu_p}{\varepsilon_r \varepsilon_o A_M} \tag{2.27}$$

Where,

$\mathbf{A_M}$ is the area of one molecule of the PFPE adsorbate.

The authors further postulated that the effect of the adsorbed film thickness could be accounted for by calculating the charge density through the thickness of the film as

$$\mu_p = K_1 \int_0^h n dz \tag{2.28}$$

Where

K_1 is a constant of proportionality,

n is the charge density through the thickness,

h is the film thickness, and

z is the vertical distance from the hard disk surface.

The charge density, *n*, was modeled by a Boltzmann distribution of the form

$$n(z) = n_o \cdot e^{-mz} \tag{2.29}$$

Where n_o is the charge density at the hard disk surface, and *m* is a mode 1 fitting coefficient. By setting $k = K_1(n_o/m)$ and combining Equations 2.27 – 2.29, the final predictive result was obtained as

$$\Delta\Psi(z) = \frac{k}{\varepsilon_r \varepsilon_o A_M}\left(1 - e^{-mz}\right) \tag{2.30}$$

The dipole moment for the PFPE film investigated was calculated as 0.13 D as compared to published values of 0.04 D for similar lubricants. An important conclusion of this study was that the nvCPD probe was shown to be capable of measuring lubricant thicknesses on the order of 2-40 nm thick.

Surface Photovoltage and CPD Characterization of Silicon

Kelvin probes have also been used to measure properties of semiconductor materials[32]. The objective of these characterizations was to measure the electronic properties of the silicon[33-37]. Minority carrier lifetime is frequently measured to obtain information about doping levels and surface quality of semiconductor substrates. The measurement of minority carrier lifetimes in semiconductors was demonstrated by Johnson[33] in 1957. The setup utilized by Johnson is schematically illustrated in Figure 2-15. The signal was generated by applying optical pulses to the surface of the semiconductor, and a Kelvin probe was used to monitor surface charge as a function of time.

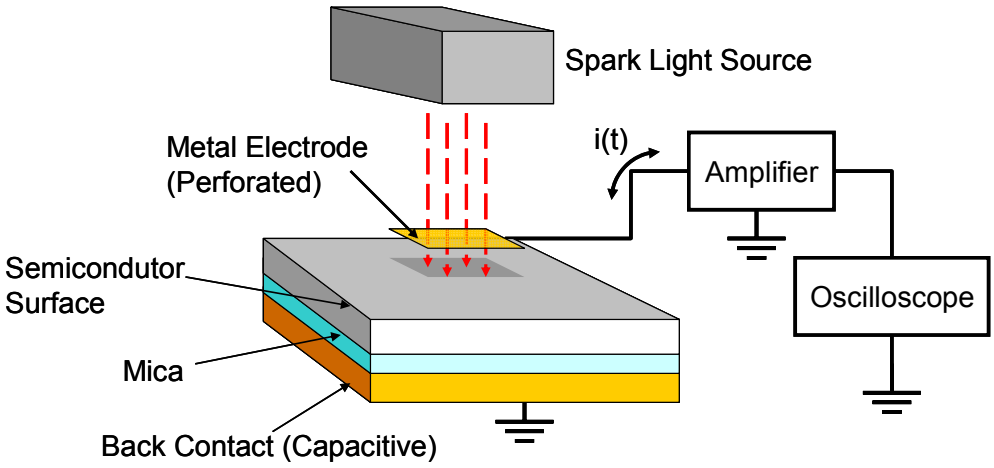

Figure 2-15: CPD Measurement of Minority Carrier Lifetime

As illustrated in Figure 2-16, Johnson ascribed the resulting signal to the combined effect of trapped charges at the semiconductor surface and the photovoltage created by the pulsed light input. The fixed trapped charges create a static space charge region in the semiconductor. When the light is on, excess carriers injected by photogeneration modulate the space charge region, with the change in surface potential being due to

surface photovoltage. After the light turns off, excess carriers recombine, and the SCR returns to the flat band state. The recombination rate of the excess carriers, and thus the decay rate of the measured CPD signal, is influenced by the surface and bulk quality of the silicon.

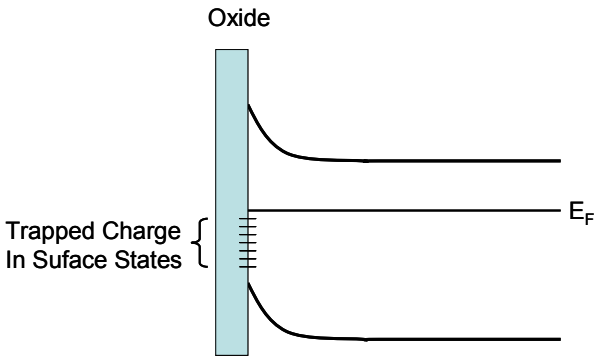

Figure 2-16: Schematic by Johnson[33] of Trapped Charge & Photovoltage

In 1999, Lagel et al. reported on similar experiments using p-type (100) silicon and a CPD probe[35]. The experimental setup is illustrated schematically in Figure 2-17. The spark light source used by Johnson was replaced by a 3mW laser diode operating at 670nm. The measured signal was captured by a high-speed oscilloscope. Measurements were made with a vibrating CPD probe with the laser continuously on or off.

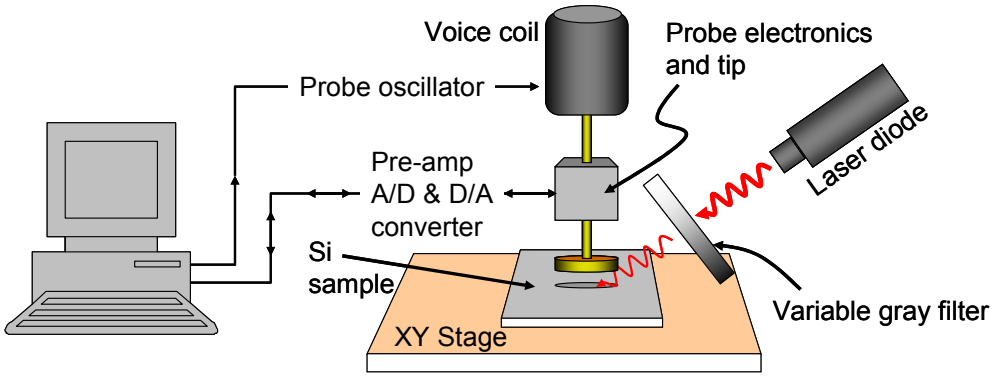

Figure 2-17: Schematic of Lagel's Si contamination CPD measurement system

Two groups of silicon substrates were measured. The first group, Wafers A and B, had a native oxide layer, and the second group, Wafers C and D, had a 15nm thick thermally grown oxide layer (30 minutes at 900C). Wafers B and D were intentionally contaminated by immersion in Fe-spiked solution which resulted in surface concentrations of Fe of approximately 10^{12} atoms/cm^2. The experiments demonstrated that the surface photovoltage technique is sensitive to iron contamination during wafer processing. As illustrated in Figure 2-18, a key observation is that the presence of iron *increased* the work function of the silicon surface by approximately 50 meV.

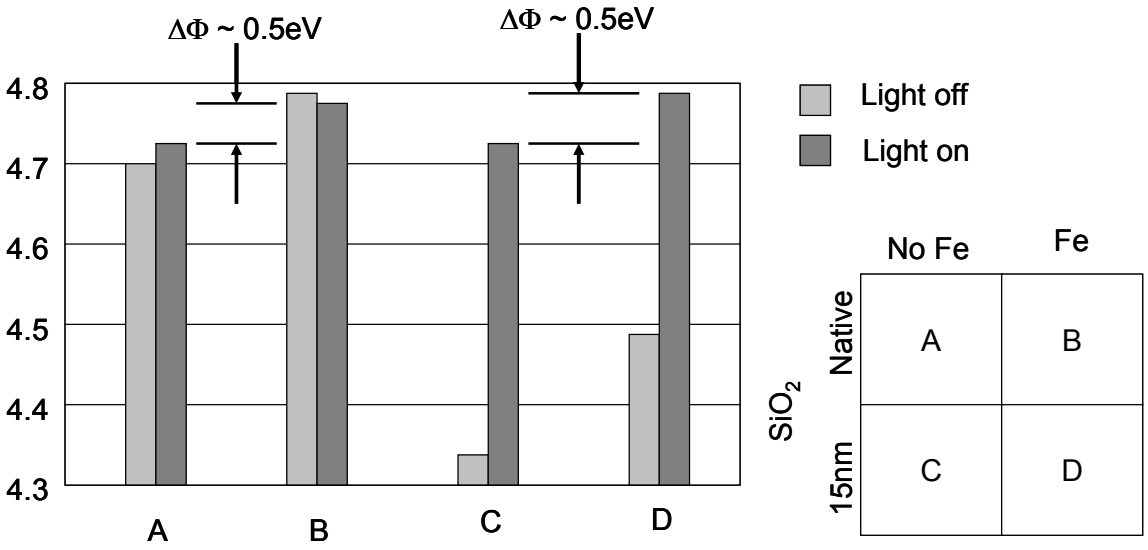

Figure 2-18: Reproduction of Lagel's Si CPD results

In the case of a non-vibrating CPD probe, Schroder[32] ascribes CPD signal generation to the detection of the quasi-Fermi level at the surface of the silicon. The quasi-Fermi level is created by the injection of excess minority carriers into the SCR when continuous incident light is turned on. The analysis is essentially identical to that for a MOS-C with the metal surface represented by the probe tip. Figure 2-19 shows a typical band diagram for a p-type MOS-C

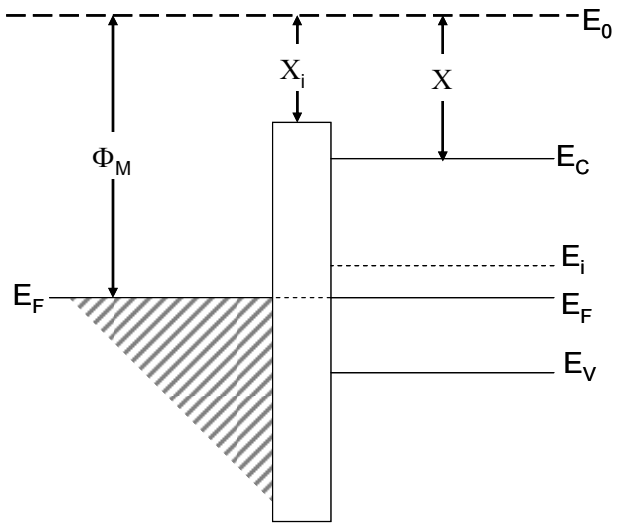

Figure 2-19: Equilibrium energy band diagram of a typical MOS-C

The major difference between the response of the gate voltage in a MOS-C and the probe tip voltage in a CPD probe is that in the CPD probe it is the surface potential of the silicon that drives the potential of the probe tip, V_T, as schematically illustrated in Figure 2-21. As shown in Figure 2-20, the reverse is true of a MOS-C in which the gate voltage, V_G, drives the surface potential of the silicon.

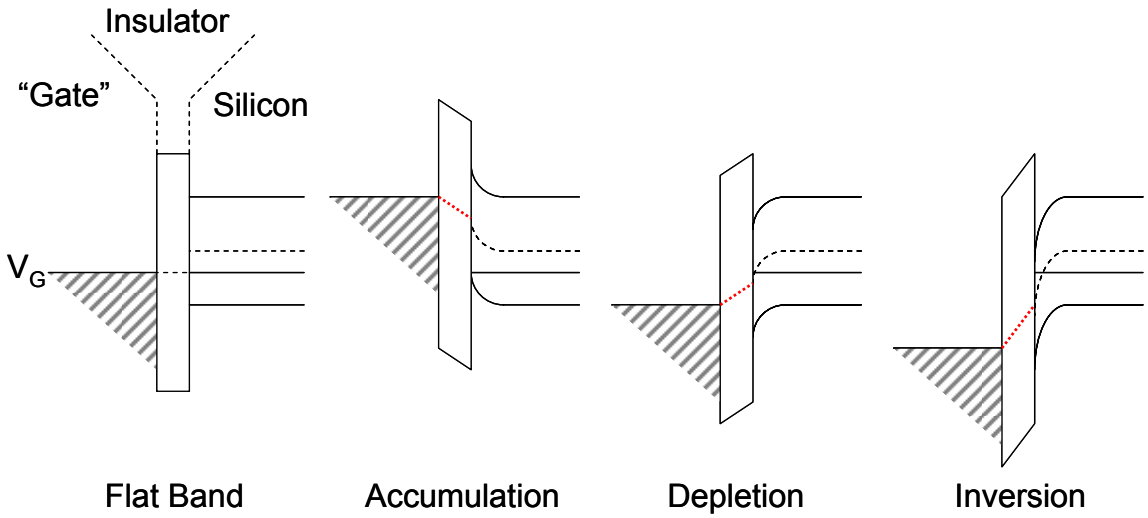

Figure 2-20: Schematic diagrams of gate voltage, V_G, driving silicon surface potential

As shown in Figure 2-20, the gate voltage in a MOS-C, V_G, drives the surface potential in the silicon. In this sense, the gate voltage can be seen as a potential "handle", pulling the surface potential of the silicon to follow it.

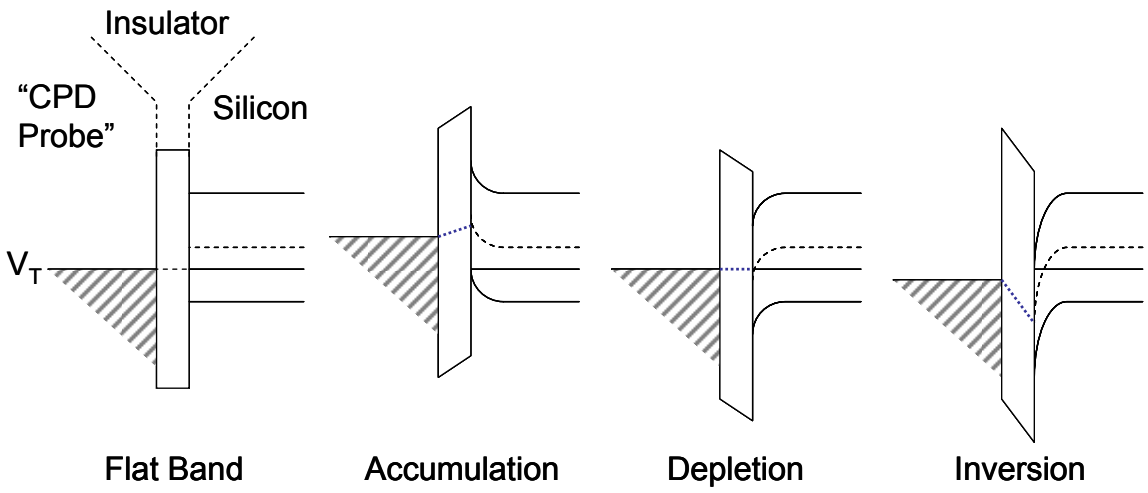

Figure 2-21: Schematic diagrams of silicon surface potential driving probe voltage, V_T

As shown in Figure 2-21, the surface potential of the silicon drives the response in the CPD probe tip, V_T. In this sense, the silicon surface potential can be seen as a potential "handle", pulling the surface potential of the probe tip to follow it.

Theoretical Extension to osCPD Sensor

As described by Johnson[33], the presence of a charge trapped at the interface between the silicon and SiO_2 leads to a static SCR and its associated band bending, as illustrated in Figure 2-22.

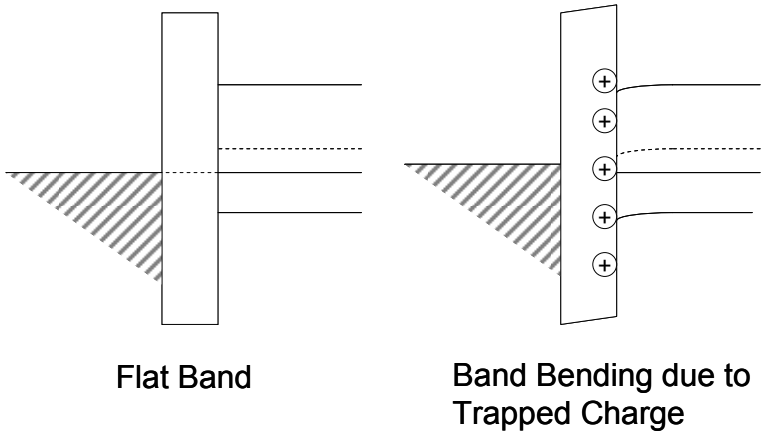

Figure 2-22: Schematic of static band bending due to trapped charge at Si-SiO_2 interface

The static SCR shown in Figure 2-22 is present in the osCPD sensor even when there is no incident light. As schematically illustrated in Figure 2-23, the static SCR present due to the trapped charge is in turn modulated by minority carrier diffusion induced by the chopped light. When light is turned on, an electron quasi-Fermi level is created in the silicon. The energy of the quasi-Fermi level is determined by the adsorbed layer of polar molecules. When the light is off, the silicon returns to the grounded (flat-band) state.

As the light intensity is modulated, the quasi-Fermi level is modulated between a maximum steady-state value when the light is on, and a grounded state when the light is off. This drives an image charge in the osCPD probe tip that is proportional to the energy of the quasi-Fermi level in the silicon.

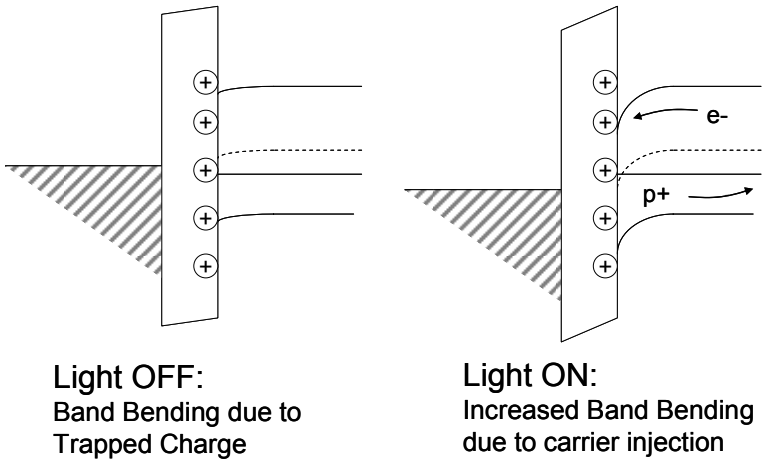

Figure 2-23: Schematic diagram of effect of carrier injection with trapped charge

The response of the CPD probe tip in the osCPD sensor is expected to be of the form

$$i(t) = C \cdot \frac{\left(\Phi_{ON} - \Phi_{OFF}\right)}{|e|\Delta t} \tag{2.31}$$

Where

$\mathbf{\Phi_{ON}}$ is the light-induced quasi-Fermi level in the silicon substrate, and

$\mathbf{\Phi_{OFF}}$ is the (grounded) Fermi level when the light is off.

Finally, the surface potential of the silicon substrate, $\mathbf{\Phi_{ON}}$, is determined by the presence of adsorbates according to the combined Langmuir isotherm and Helmholtz equation previously given in Equation 2.25 as

$$\Delta\Phi = k\frac{KC}{\left(1+KC\right)} \tag{2.32}$$

CHAPTER 3

EXPERIMENTAL APPARATUS

A substantial number of components were custom designed and fabricated for the purpose of this research. These included a CPD probe and purpose-built experimental test fixtures. The custom-built components were used in combination with commercially available test and lab equipment. All of these items were integrated into a test platform with software-driven data acquisition. This chapter describes the experimental equipment used in this research.

Test System Architecture

The experimental apparatus consisted of four primary subsystems: a test fixture, a CPD probe, a modulated light source, and a data acquisition system. A photograph of the osCPD test fixture is shown in Figure 3-1, and a simplified wiring diagram of the main components is shown in Figure 3-2. The system was designed to allow precise control of key experimental parameters in order to enhance experimental repeatability. These parameters included the intensity and wavelength of the light source, the frequency at which the light source is modulated, the thickness of the oil film under investigation, and the spacing between the probe tip and the silicon substrate. The following section contains a description of the osCPD test fixture. Subsequent sections provide details and specifications for the CPD probe, the light source, the data acquisition hardware and software, and other individual components and pieces of equipment.

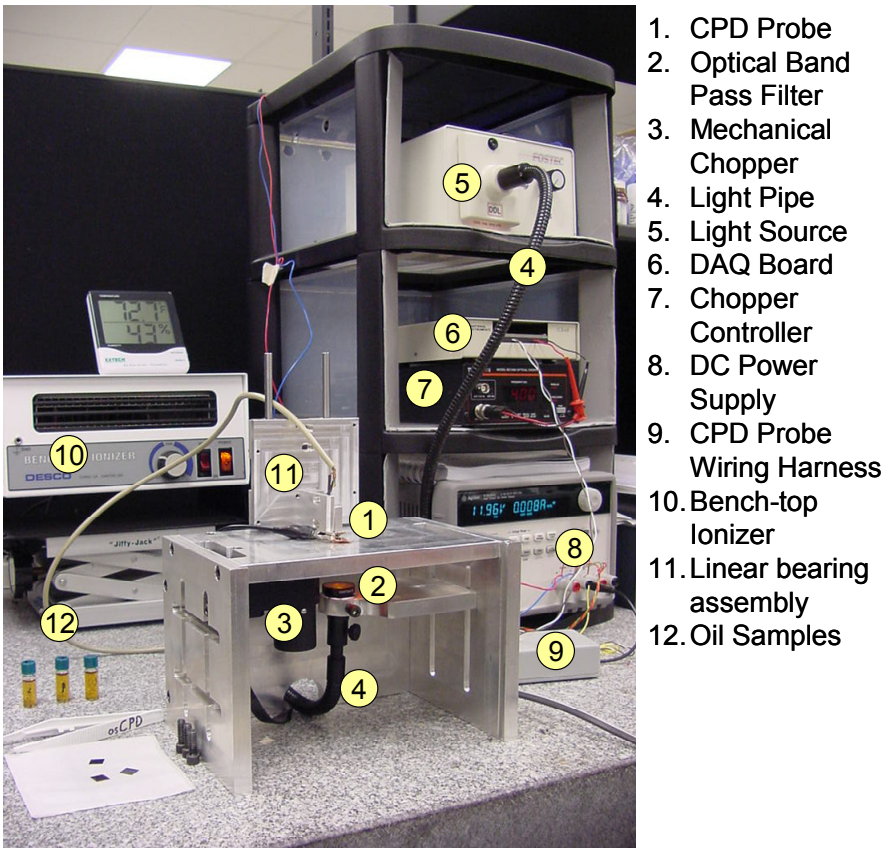

Figure 3-1: Photograph of primary components of osCPD Sensor Test System

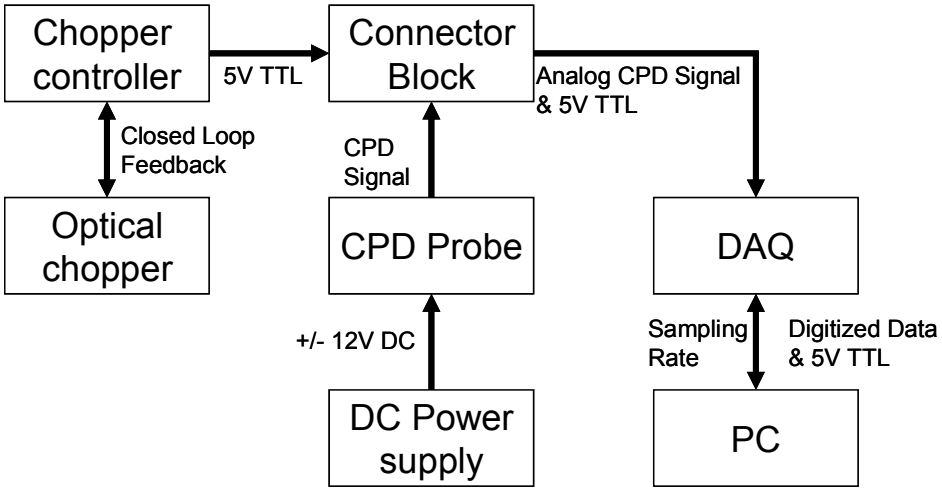

Figure 3-2: Schematic wiring diagram for test system

Test Fixture

The test fixture served to hold in alignment the optical source, the chopper, the target semiconductor substrate, and the osCPD probe and electronics. A linear bearing assembly was made using four pillow block bearings to allow easy, accurate and repeatable positioning of the osCPD probe with respect to the silicon substrate. The bearings constrained motion to the vertical axis only, thus ensuring that the orientation of the osCPD probe tip remained parallel to the test fixture, and to the surface of the silicon substrate. Although absolute parallelism between the probe tip and silicon surface is not strictly required, a constant, fixed orientation is necessary for repeatable measurements.

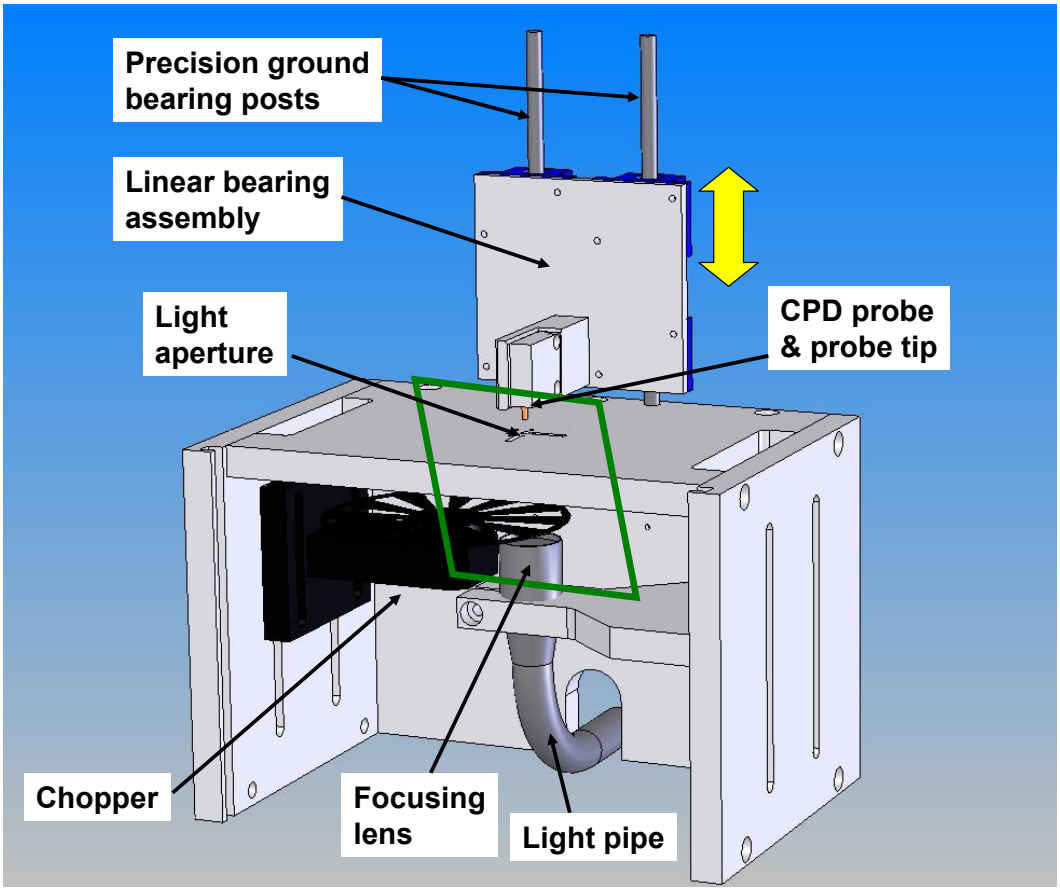

Figure 3-3: Schematic of osCPD test fixture; inset shown in Figure 3-4

Precise alignment of the bearing posts and self-aligning pillow-block bearings allowed the bearing assembly to move freely. Silicon substrates were easily placed and removed from the test fixture by sliding the linear bearing assembly up and down. When the silicon substrate was in position the bearing assembly was lowered and the weight of the bearing assembly provided a moderate and repeatable static down force. This force served to keep the sample securely in position as well as to encourage good electrical contact with a copper grounding strip. The down force from the weight of the bearing assembly also ensured consistent film thickness in the oil sample contained in the sandwich formed by the silicon substrate and mica.

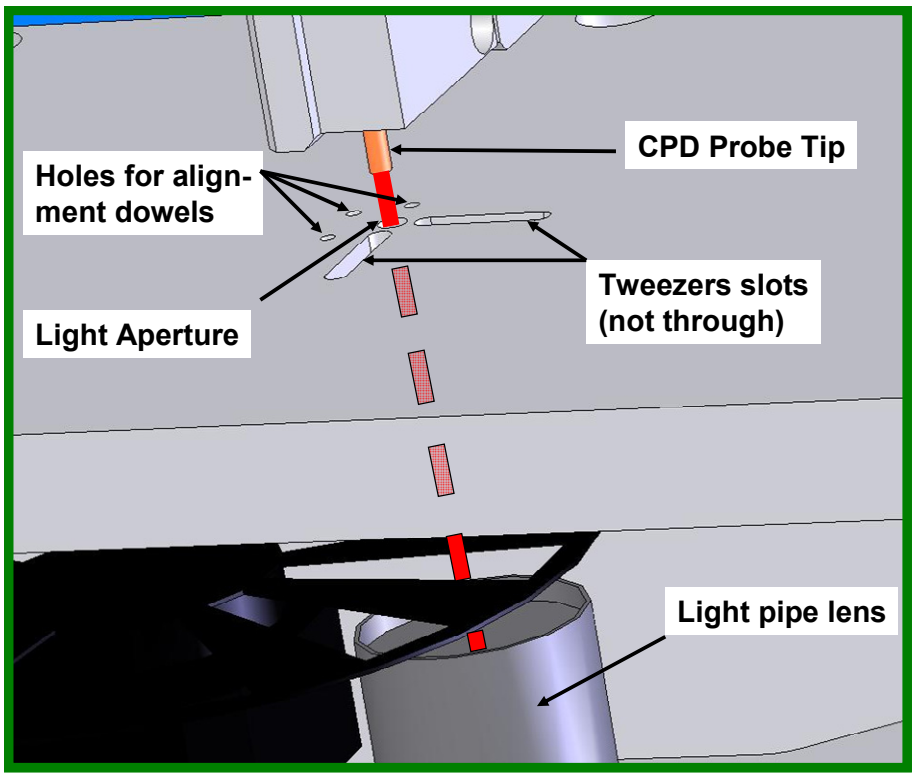

Figure 3-4: Schematic illustration of details of CPD probe alignment with light source

Repeatable positioning and alignment of the silicon substrate was achieved by using three steel dowel pins. The dowel pins were press-fit into alignment holes drilled in the top surface of the test fixture, as shown in Figure 3-4. Rotational alignment of the silicon substrate was not strictly necessary due to the orientation independence of the CPD probe tip and the symmetry of the silicon. However, lateral positioning of the substrate with respect to the light source and probe tip is important to minimize edge effects from minority carrier diffusion. The alignment dowels were positioned so as to ensure that the silicon substrate was centered with respect to the aperture and probe tip.

CPD Probe Tip

The CPD probe and probe tip described in the following section and used in this investigation were designed and built by Dr. Anatoly Zharin. Designs presented by authors in previous studies have concentrated on reducing probe size in an effort to increase spatial resolution. However, the increased spatial resolution incurs a proportional reduction in probe sensitivity. In this investigation, lateral resolution was not deemed important. A probe tip with much larger area than typical was desired to yield an increased signal and enhance analytical capability.

Manufacturing of the probe tip and associated shielding is a complex task for most nvCPD applications. The primary function of guard shield on the probe tip is to increase lateral resolution by minimizing field fringing. As mentioned previously, lateral

resolution was not a concern in this investigation. Therefore, the probe tip used in this investigation was unshielded.

Another concern in CPD probe design is stray capacitance. This is of primary concern at the input to the first stage amplifier. Long electrical leads between the probe tip and the Op-Amp input can act as antennas and adversely affect signal-to-noise ratio. It is also known that leakage currents on the printed circuit board can adversely affect the circuit performance[50]. Most CPD probe designs employ a grounded or biased guard ring around the first stage op-amp input on all layers of the circuit board. This is done to prevent leakage currents (possibly from stray capacitance elsewhere in the circuit) from influencing the input signal.

Stability of the work function of the surface of the probe tip is important for repeatable CPD measurements. In the case of vibrating CPD systems, it is often desirable to use noble metals for the probe tip surface. This allows absolute work function measurements to be made when the CPD probe tip is calibrated against a know reference surface. In the osCPD sensor, the objective is to measure relative changes in the fluid under investigation, not measurement of changes in absolute work function of the target surface. The primary requirement, therefore, is that the probe tip material be relatively stable with respect to the time frame of the experimental measurements.

The primary design considerations for the probe tip to be used in the osCPD sensor were that it should have a relative large probe tip area, a short tip-to-input lead, and that the

surface be comprised of a stable material. As illustrated schematically in Figure 3-5, these objectives were met in a single design solution. The input lead for the first-stage operational amplifier was bent up and away from the printed circuit board, and a resistor was soldered directly to the pin. The flat end of the resistor served as the probe tip. A photograph of the first-stage amplifier and probe tip is shown in Figure 3-6.

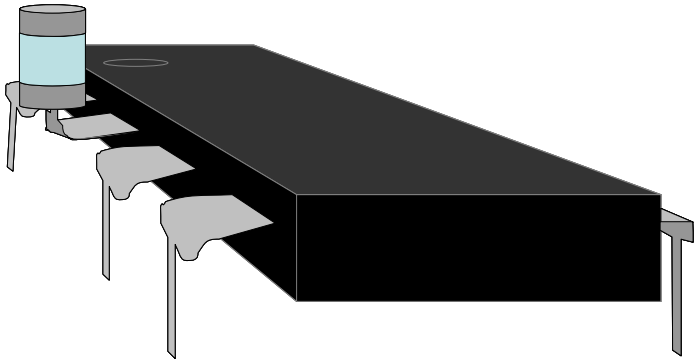

Figure 3-5: Schematic illustration of 1st stage amplifier and direct-lead probe tip

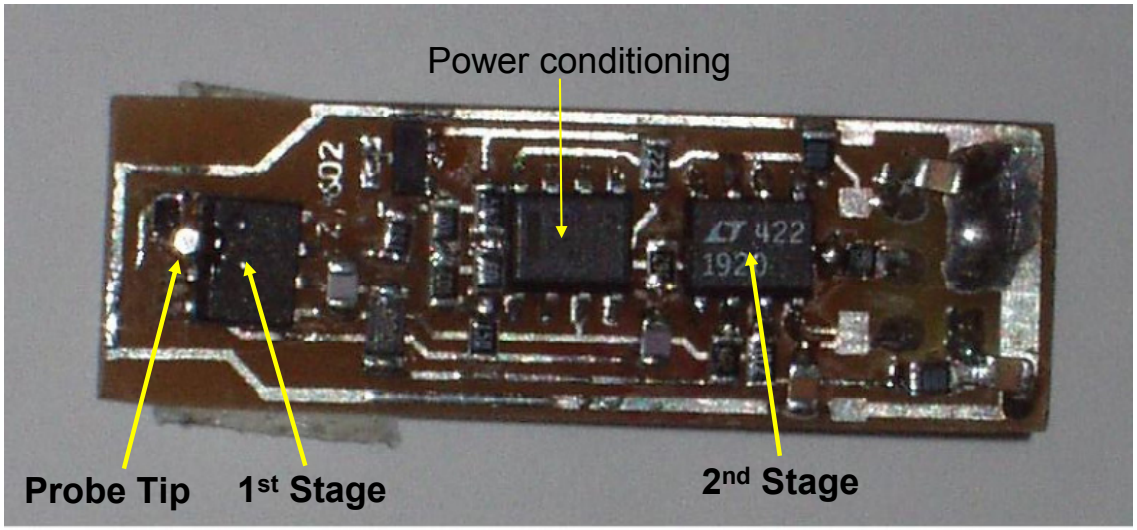

Figure 3-6: Photograph of CPD probe and electronics

CPD Signal Detection & Amplification Circuit

The CPD amplification circuit was designed and fabricated to convert the current generated in the CPD probe tip into a voltage output that was read by the data acquisition system. Primary considerations in the design and construction of the circuit were the temporal response (rise time and settling time), gain, signal to noise ratio, and circuit isolation from the data acquisition system. As shown in Figure 3-7, the circuit had two amplification stages. The first stage consisted of a high-speed precision operational amplifier. The second stage consisted of a single-resistor gain-programmable precision instrumentation amplifier.

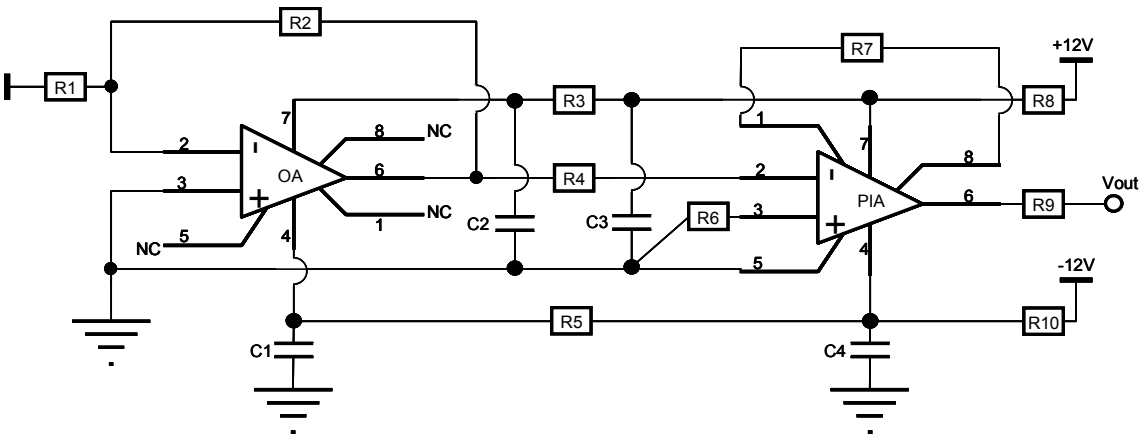

Figure 3-7: Schematic diagram of CPD signal detection and amplification circuit

Table 3-1: CPD Probe as-built discrete component values for circuit in Figure 3-7

R1 = 12kΩ	R6 = 200Ω	C1 = 0.1μF
R2 = 1GΩ	R7 = 5.6kΩ	C2 = 0.1μF
R3 = 100Ω	R8 = 100Ω	C3 = 0.1μF
R4 = 200Ω	R9 = 100Ω	C4 = 0.1μF
R5 = 100Ω	R10 = 100Ω	

Component Values As Built

Note, all discrete component values accurate +/- 5%

The first stage amplifier was a Burr Brown OPA602AU high-speed precision operational amplifier (OA). The second stage amplifier was a Linear Technology LT1920CS8 precision instrumentation amplifier (PIA). The total gain of the CPD probe as designed was approximately 8.2×10^5. Select electrical characteristics for the amplifiers are given in Table 3-2.

Table 3-2: Electrical characteristics for the amplifiers used in the CPD circuit

	1st Stage Amplifier	2nd Stage Amplifier
Manufacturer & model	Burr Brown OPA602AU	Linear Technology LT1920CS8
Gain as assembled	8.3×10^4	9.8
Slew rate	35 V / μs	1.2 V / μs
Settling Time	< 1 μs	14 μs
CMRR – Common mode rejection ratio	100 dB	95 dB

Thermal Noise Considerations

Thermal noise (also known as Johnson-Nyquist noise) is noise that originates from random fluctuations of the electric current inside an electrical conductor due to random thermal motion of electrons[38,51]. Thermal noise is white noise, and is therefore proportional to the bandwidth of the circuit. Thermal noise is also proportional to the operating temperature and resistance of the resistor in the circuit.

Thermal noise can be calculated as:

$$V_n = \sqrt{4kTR_1(\Delta f)} \tag{3.1}$$

where

k is Boltzmann's constant = 1.381 x 10-23 J/K

T is the conductor temperature in degrees Kelvin (in this case 300K),

R_1 is the resistance (in this case 12kΩ as shown in Figure 3-7), and

Δf is the bandwidth in hertz, 290Hz for most experiments.

Since the thermal noise from the probe tip appears as a voltage at the input to the first stage amplifier, it is expected that this noise will be amplified and appear in the output signal. From Table 3-2, the total gain of the amplification circuit is 8.1 x 10^5. The expected thermal noise in the osCPD out signal, V^*_n, is therefore calculated as[39]

$$V^*_n = \left(8.1x10^5\right)\sqrt{4kTR_1(\Delta f)} \tag{3.2}$$

The predicted thermal noise in the output signal, V*n, is therefore calculated to be on the order of

$$V^*_n \cong 0.2V \tag{3.3}$$

This value is significant when compared to the typical peak-to-peak voltage signal of approximately 1.2 V. However, due to the waveform averaging scheme used in data acquisition as described in Chapter 4 the white noise created by the thermal noise of the probe tip is effectively filtered from the signal, leaving only the osCPD waveform. Similar calculations were performed for the feedback resistor on the first-stage amplifier, R2 as shown in Figure 3-7. In this case, only the 2nd-stage amplification of 9.8 applies, and the thermal noise contribution, V^*_n, is predicted to be 6.9x10^{-4} V at the output. Noise from the 1GΩ resistor is therefore not of concern with respect to the final osCPD signal.

CPD Probe Frequency Response

Measurements were made to characterize the frequency response of the CPD probe and amplification circuit. The typical operating frequency of the optical chopper is on the order of 600Hz or less, so the intention of this characterization was to verify that the CPD probe of Figure 3-7 has sufficient bandwidth to adequately capture the osCPD signal. A pattern generator was used to apply a 40mV sinusoidal voltage bias to a copper reference plate. The CPD probe tip was capacitively connected to the reference plate using a 10nF capacitor, and the peak-to-peak output voltage was captured and recorded. As seen in Figure 3-8, the probe shows no sign of roll-off or high-frequency attenuation below 100kHz. Since the osCPD system typically operates below 1kHz, the CPD probe is assumed to have adequate bandwidth to measure the osCPD signal.

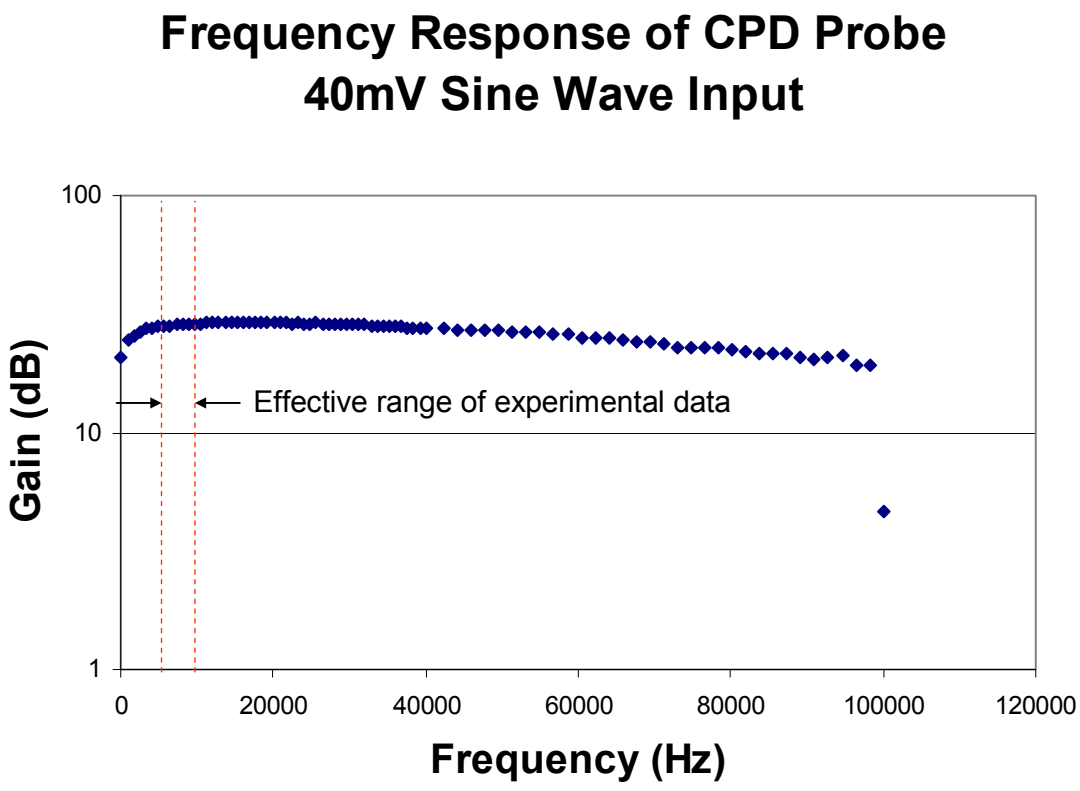

Figure 3-8: Frequency response of CPD probe used in osCPD system

Light Source

A Fostec Ace I DDL illuminator was used as the light source to illuminate the backside of the silicon substrate. The light source contained an internal infra-red filter so that only visible light was emitted from the source. A light pipe consisting of a fiber optic bundle with a focusing lens at the output end was used in conjunction with the illuminator to precisely locate and focus the light at the desired location. Optical band pass filters were placed over the end of the light pipe lens so that the wavelength of light incident on the silicon substrate could be controlled. Due to the combined use of the internal infrared filter and the band pass filters, no infrared light reached the silicon substrate from the light source.

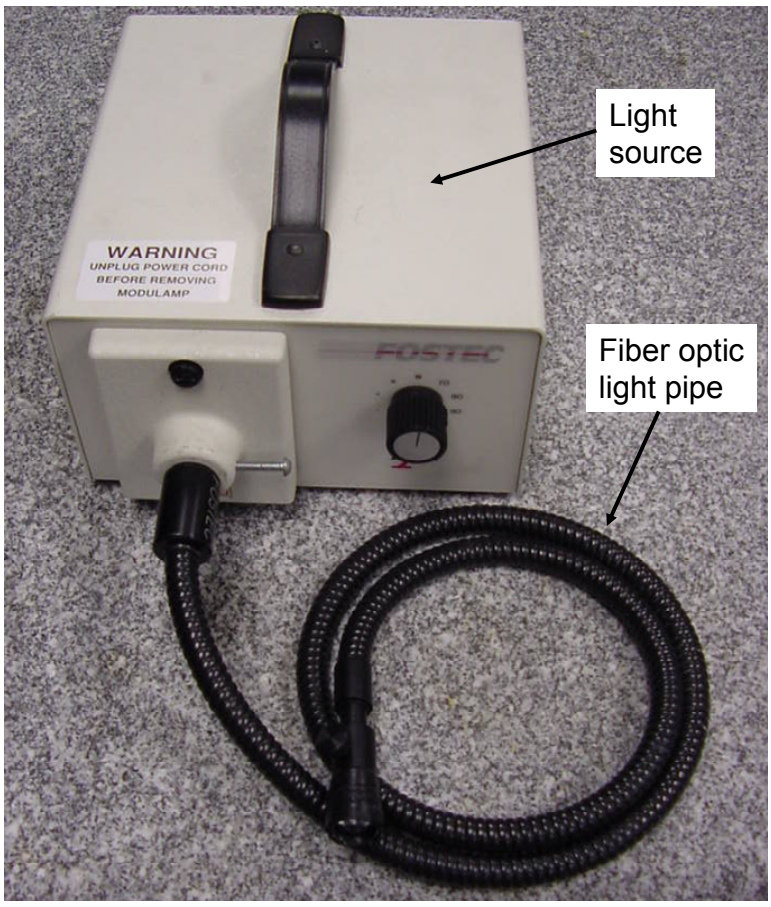

Figure 3-9: Photograph of light source and fiber optic light pipe

Optical Band Pass Filters

Bandpass filters were used to control the wavelength of the light incident on the backside of the silicon substrate. As shown in Figure 3-10, two sets of filters manufactured by Andover Optical provided a contiguous range of bandpass wavelengths covering the near infra-red and visible ranges. The center wavelengths of the filters ranged from 400nm to 1000nm in 50nm increments. The individual filters were 25mm in diameter, and had a bandpass of 40nm (central wavelength +/- 20nm). As shown in Figure 3-11, the optical filters were placed one at a time over the end of the light pipe focusing lens, immediately beneath the optical chopper. The diameter of the filters was larger than that of the lens housing on the end of the light pipe such that the filter was kept securely in place by the frame of the lens.

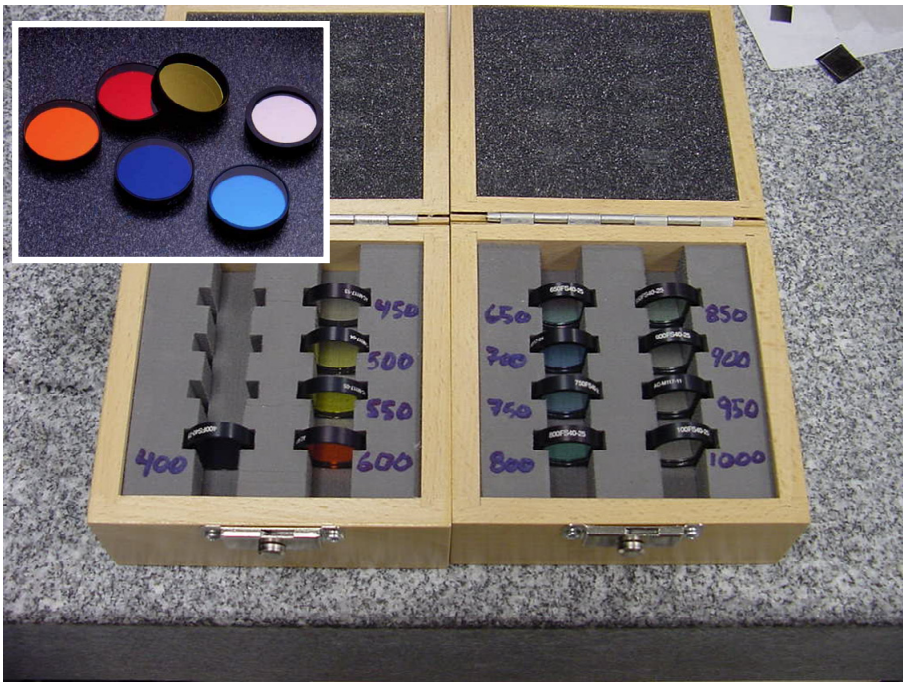

Figure 3-10: Photographs of optical band pass filters – inset from manufacturer's website

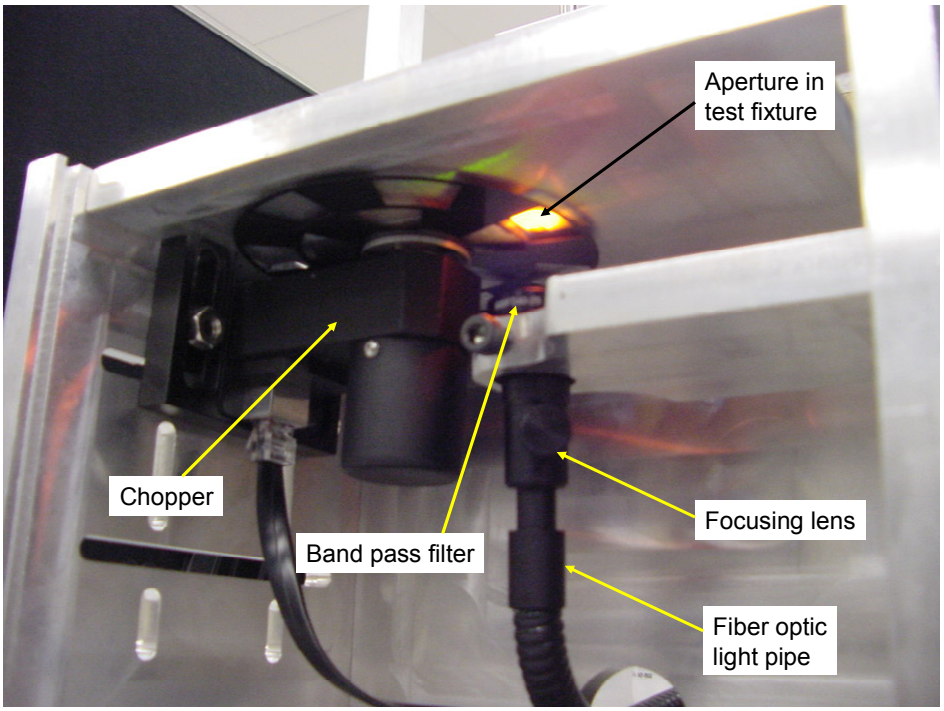

Figure 3-11: Photograph of band pass filter in position on lens of fiber optic light pipe

With the optical filters in place (one at a time), the intensity of light typically reaching the back surface of the silicon substrate through the light aperture was measured using the optical power meter described in the following section. These measurements could not be done with the silicon substrate in place, but repeated measurements of the optical power before and after experimentation confirmed the stability of the light source. The optical head from the power meter was placed over the aperture on the top surface of the test fixture and the power from the light source was set from low to high intensity. Figure 3-12 contains the resulting power spectra. It should be noted that the smoothed lines in the chart have been added for ease of viewing and interpretation. The bandpass filters only allowed light transmission at discrete wavelengths. The corresponding discrete measurements are shown on the chart as individual data points.

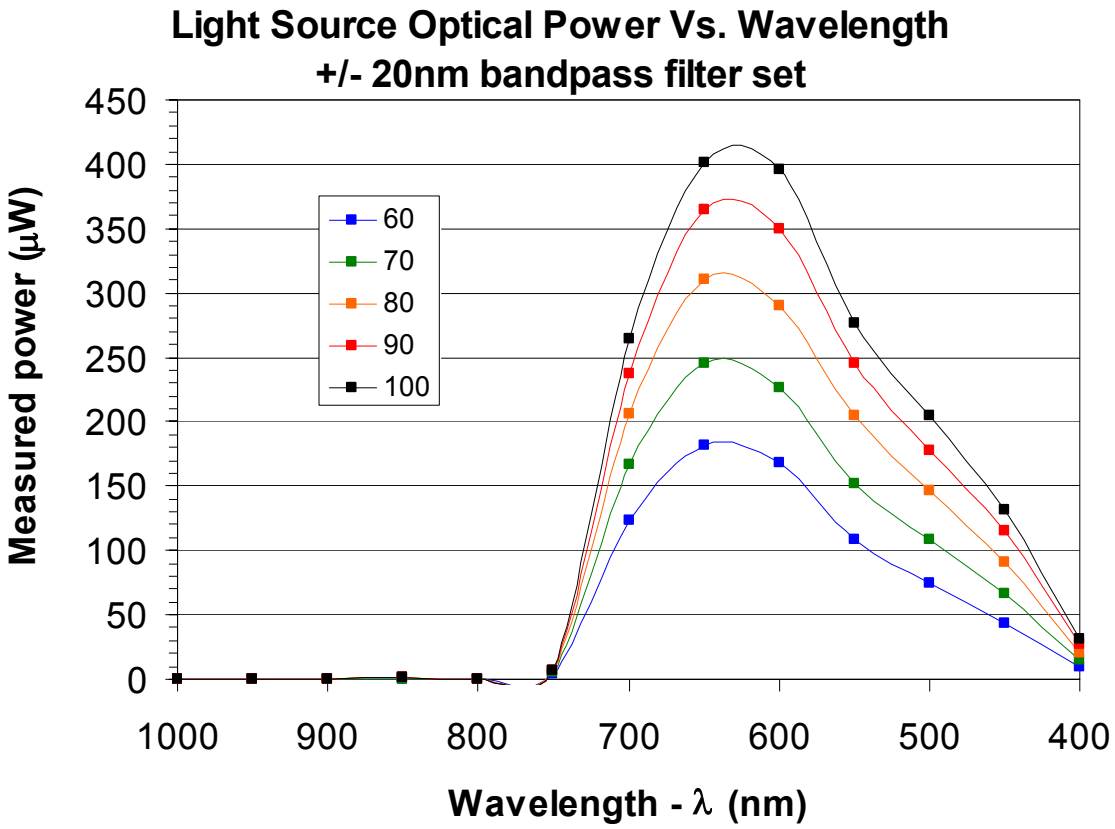

Figure 3-12: Optical power characterization of incident light on silicon substrate

The individual curves in Figure 3-12 represent power settings on the Fostec light source. 60 indicates a nominal 60% power setting, 70 is a 70% power setting, and so on. It is clear from the chart that no significant infrared energy reaches the back surface of the silicon substrate. It is also evident upon closer inspection that the light source dimmer offers nearly linear control of the light intensity.

Optical Chopper

A Thorlabs MC1000A Optical Chopper was used to modulate the intensity of light incident on the backside of the silicon substrate. A mechanical chopper was chosen primarily for experimental convenience (compatibility and interchangeability with a wide variety of light sources and filters). Any modulated visible light source (e.g. LEDs have also been used succesfully) could readily replace the mechanical system used here. The chopper consisted of a control box, a chopper head, and interchangeable chopper blades. The control box provided power and speed control to the chopper, and also served as the user interface by which target frequency was controlled using the integral LED panel display. The indicated frequency on the chopper controller represented the chopping frequency, or number of blades per second that transitioned the light aperture.

As shown in Figure 3-2, the 5V TTL output from the MC1000A was connected directly to the Digital Trigger input of a National Instruments SCB-68 shielded connector block. This allowed direct synchronization of data acquisition with the optical chopper. The MC1000A is capable of using several interchangeable chopper blades. Three blades were used in the course of this research: a 2-slot, 5/7-slot, and 10-slot blade. The frequency ranges available by using these blades ranged from 15 Hz with the 2-slot blade to 1000 Hz with the 10-slot blade. Frequency was controllable in increments of 1Hz for the 7-slot and 10-slot blades. The frequency stability is specified by the manufacturer as <100ppm frequency drift, and 0.2° RMS phase jitter –at 1kHz. This degree of stability greatly reduces concerns about aliasing during waveform acquisition and averaging. This was particularly important in filtering out thermal noise generated by the probe tip which was made from a resistor.

Data Acquisition Hardware

The automated data acquisition hardware consisted of a National Instruments PCI-6052E data acquisition card (DAQ) and a National Instruments SCB-68 shielded connector block. The output voltage signal from the CPD probe was connected directly to the SCB-68 connecter block. All unused analog input channels on the connector block were tied to a common ground to reduce spurious signal generation. The connector block was connected to the PCI-6052E DAQ by a 2-meter shielded cable. The DAQ was inserted in a PCI slot on in an IBM compatible PC running a Windows XP operating system. The DAQ had a maximum sampling rate of 200 kilo-samples per second (200 kS/s). Analog voltage data from the CPD probe was converted to a digital signal by the DAQ, and captured using data acquisition software on the PC.

Data Acquisition Software

A commercially available data acquisition software package was used to capture the osCPD voltage signal. A screen capture image of the primary user interface is shown in Figure 3-13. The software allowed control of the data acquisition rate (sampling rate) as well as control of the sampled data scan length. The scan length here is defined as the number of discrete data points that are captured in a single data string. Due to the frequency stability of the optical chopper, the chopper's 5V-TTL digital trigger signal enabled capture and averaging of multiple scans to obtain nearly noise-free waveforms. This was particularly useful in filtering out any noise in the probe amplification chain.

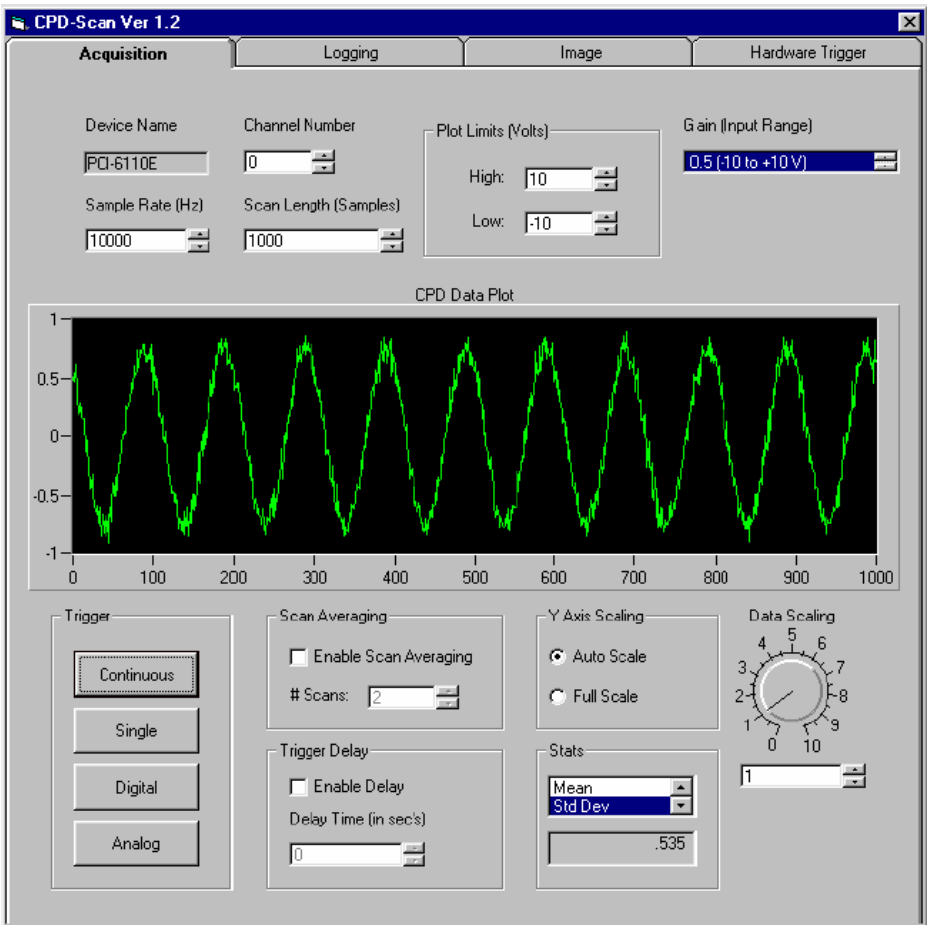

Figure 3-13: Screen capture of data acquisition software GUI from user's manual

DC Power Supply

A clean, stable power source is important for use with operational amplifiers, particularly given the low signal levels typical in CPD applications. An Agilent E3646A dual-channel 60-watt DC power supply was used to provide power to the CPD circuit. The E3646A was selected for its stability and for ease of use due to its digital programming capability. An HP 6168B DC Current source was used to provide power for the DC-biasing experiments. The 6168B is rated for 0-300V and 0-100mA.

Bench-top Ionizer

A Desco 19500 autoset self-balancing bench-top ionizer was used to eliminate charge build-up on the experimental apparatus. Of specific concern was charge buildup that occurred in the mica sheet during cleaning. This charge was not directly evaluated, but was inferred due to the tendency of the mica to "jump" from the test fixture to metallic surfaces when dry. This behavior was mitigated by use of the ionizer. Repeatability of osCPD measurements of dry silicon substrates (i.e. no oil sample present) was also observed to increase when the bench-top ionizer was employed. As shown in Figure 3-1, the ionizer was positioned to provide continuous flow directly to the top surface of the test fixture, the CPD probe, and the silicon substrate, oil sample, and mica.

Precision Glass Spacer Beads

Spacer Grade Glass Microspheres (SGGM) manufactured by Specialty Products were used to accurately control the thickness of the oil film on the surface of the silicon substrate. This was necessary to ensure that the resulting measurements eliminated as nearly as possible the effects of variation due to the amount of oil present, as well as to ensure a constant and repeatable spacing between the osCPD probe tip and the top surface of the silicon substrate.

The spacers were made of borosilicate glass, and therefore expected to be inert when mixed with the oil samples. Three sizes of glass spacers were used. These were 100 mesh, 200 mesh and 400 mesh with corresponding diameters of 38μm, 75μm, and

150μm, respectively. The accuracy of the mean diameter of these spacers as specified by the vendor is +/- 7% for the 35μm spheres, and approximately +/- 5% for the 75μm and 150μm spheres. These particular spacers were chosen for their high sphericity, close size tolerances, mechanical strength, and chemical durability (relatively inert in the oil samples).

Digital Hotplate

A Ciramec EW-04660-10 Ceramic Hotplate was used to thermally oxidize the oil samples. The hotplate had a 4" x 4" heated surface. The hot plate was powered by an internal 120V power supply rated at 410W, and had a temperature range of 5 to 540^{o}C. A digital readout on the front panel of the hot plate in conjunction with internal digital control allowed the temperature to be set in 5C increments. The hotplate also had a magnetic stir which allowed constant agitation of the oil during heating.

Optical Power Meter

As described previously, a Coherent LaserMate-Q optical power meter was used to calibrate the optical power of the Fostec light source. The power meter was used in conjunction with a Coherent LaserMate-Q VIS optical head. Measurement characteristics for the power meter are given in Table 3-3 as well as actual parameters encountered in experimentation.

Table 3-3: Measurements specification for optical power meter

	Specified limits	*Experimental range*
Wavelength range (nm)	400-1064	400-1000
Maximum power	50 mW	< 500 μW
Minimum power	10 nW	10 nW
Accuracy (incl. display)	+/- 3%	-
Max power density	1 W / cm^2	1.67 mW / cm^2

Infrared Thermometer

An Omega OS540 infrared thermometer was used to measure oil temperature during thermal aging. The thermometer had a temperature range of -20C to 420C with a resolution of 1C. The stated repeatability for the thermometer is +/-1C, and the accuracy over the range of temperatures used to heat the oil was +/- 3%. This translates to +/- 12C at the maximum thermal aging temperature of 210C.

Visible Light Spectroscopy

A test system was assembled to allow spectroscopic measurement of the oil samples after thermal aging. As shown in Figure 3-14, the measurement system consisted of the fiber optic light source, band pass filters, and optical power meter, all as previously described. Commercially available spectroscopic cuvettes were used to hold the oil samples, and a temporary fixture was constructed to hold the components in alignment.

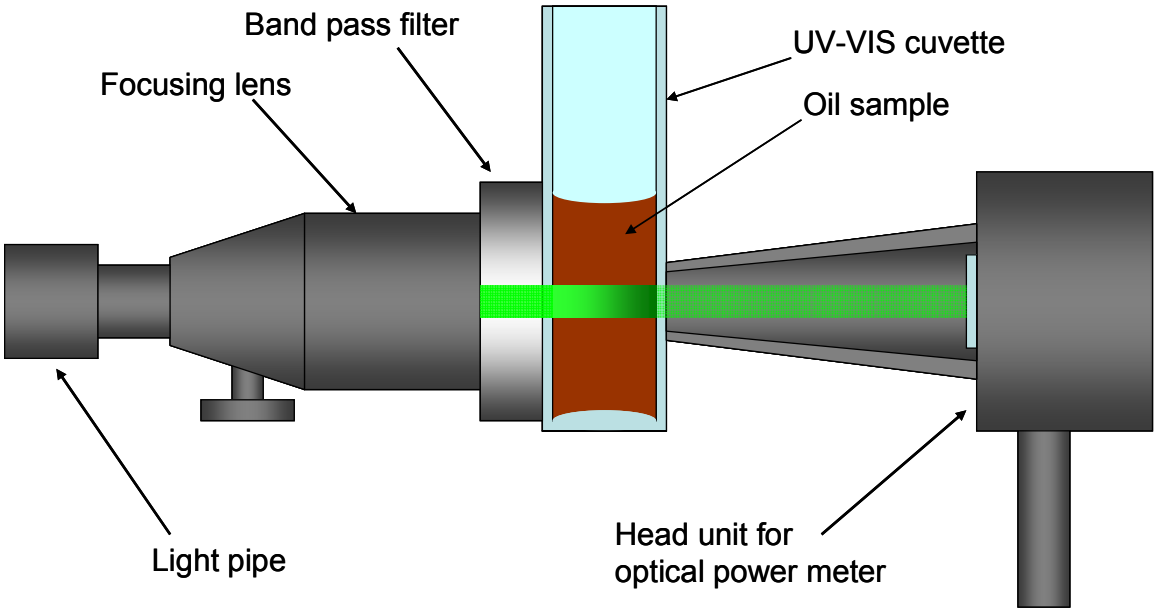

Figure 3-14: Schematic illustration of visible spectroscopy apparatus

CHAPTER 4

EXPERIMENTAL METHODOLOGY

This research involved three primary components: Theoretical modeling, experimentation and analysis of results, and engineering design and modification to the test system. Significant experimentation was conducted to validate the predictive theoretical models as well as to characterize the behavior of the osCPD sensor. This chapter will discuss the experimental approach taken in this investigation, and the methods and procedures used in conducting experiments.

Figure 4-1 contains a flow chart that illustrates the approach of this investigation. The yellow shaded blocks indicate experimental activities. The following sections will focus primarily on experiments conducted on oil samples as indicated in Figure 4-1. The discussion will describe the process of experimentation to include sample preparation, osCPD sensor preparation, experimental execution, and data acquisition. Specific parameters investigated for given sets of experiments are discussed in Chapter 5 along with experimental results. A substantial number of experiments were also performed using third party equipment to provide corollary information and to assist with interpretation of the osCPD sensor data. Some of these tests are described in Appendix II along with the associated results.

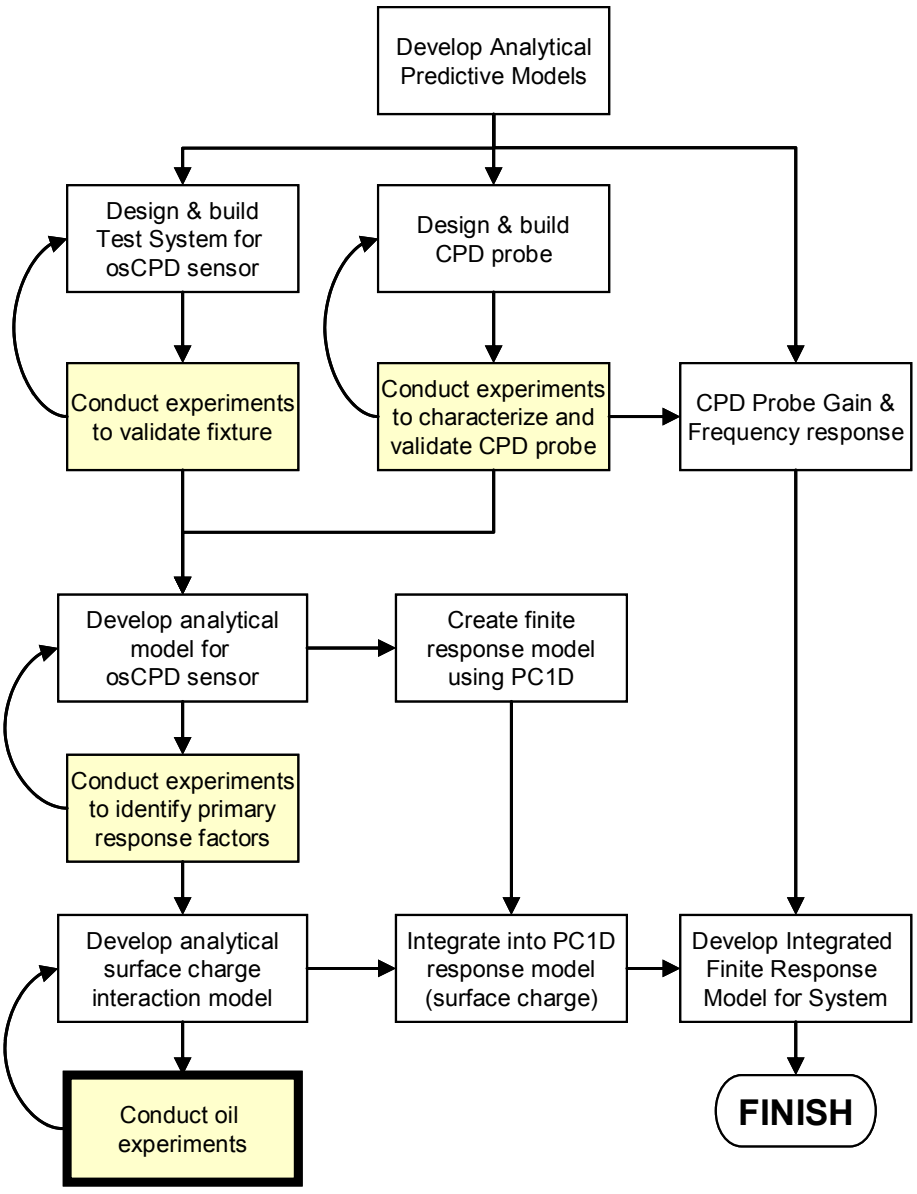

Figure 4-1: Flowchart of modeling, experimentation, and analysis process

Experimental Procedure

The same general procedure was followed for each of the oil experiments. As illustrated in Figure 4-2, the basic experimental procedure began with preparation of the silicon substrate(s), the mica, and the oil samples. Once all materials were prepared, individual samples were measured in the osCPD test system, the silicon and mica were cleaned and prepared for re-use, and the process was repeated until all measurements for a given set of experiments had been obtained. The following sections describe individual steps in the procedure in more detail.

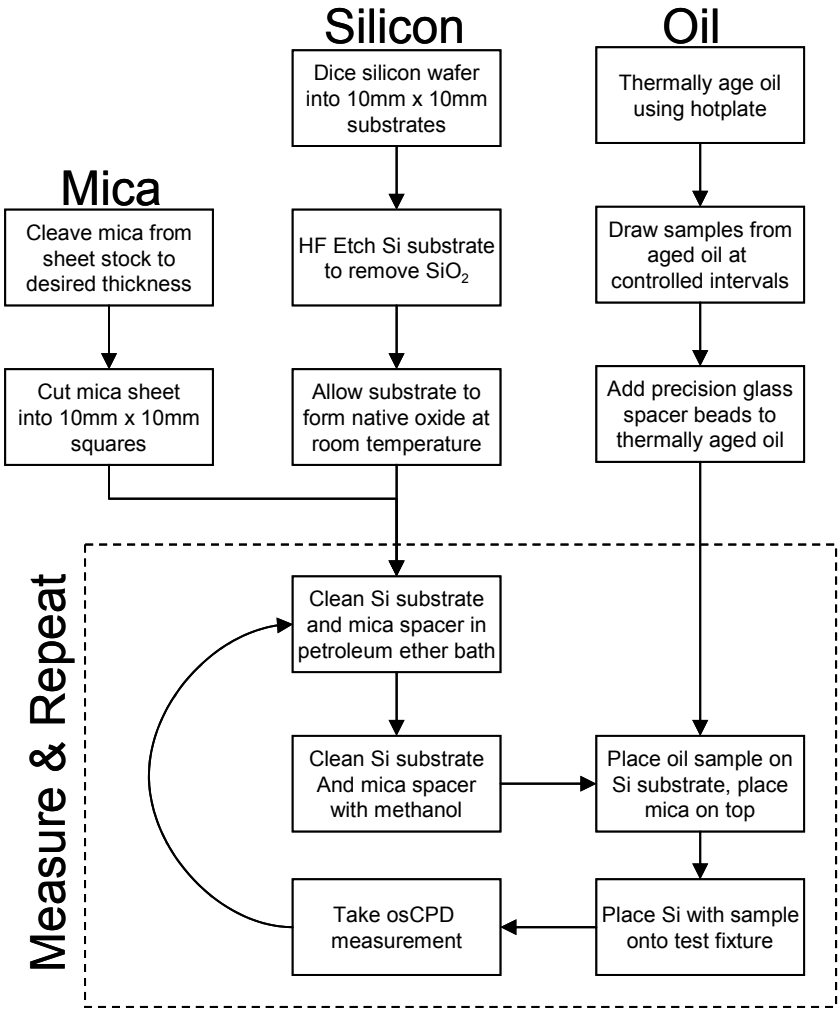

Figure 4-2: Basic experimental procedure for oil measurement

Silicon Substrate Preparation

Commercially available single crystal silicon was used as the osCPD sensor substrate for these experiments. The silicon was diced into 10mm by 10mm square chips, as illustrated in figure 4-3. Typical properties of the silicon used in the experiments are listed in Table 4-1

Table 4-1: Selected material properties of the silicon substrate

Property	*Value*
Growth Method	Cz
Crystallographic Orientation	<111>
Dopant	Boron (p-type); $N_D = 6.8 \times 10^{14} cm^{-3}$
Resistivity	20 ohm-cm
Uncut wafer diameter	125mm
Thickness	625μm
Surface Finish	Double side polished
Oxide	None (native)

After dicing and prior to experimentation, the silicon surface was prepared by etching in HF to remove any oxide layers present. The HF used was diluted with DI water to a concentration of 10%, and the silicon was placed in the diluted HF bath until hydrophobic (typically about 3-5 minutes). After etching, the silicon substrate was allowed to develop a native oxide layer in ambient laboratory conditions. The laboratory

temperature was typically maintained between 21C and 23C. The humidity was not controlled, and ranged between 35% R/H and 50% R/H.

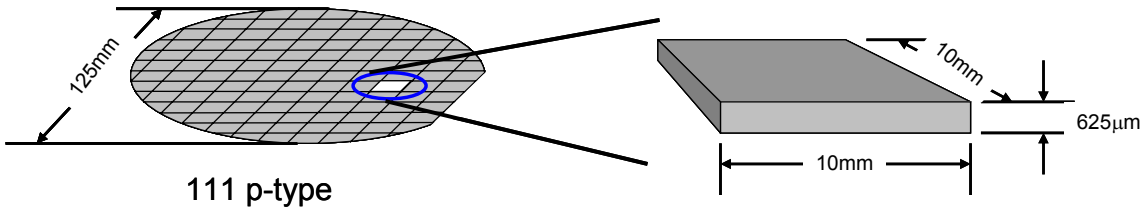

Figure 4-3: Silicon substrate geometry

Measurements of the native oxide thickness before and after etching in HF were made using several ellipsometers. The measurements are summarized in Table 4-2, and represent averaged values for etched and non-etched samples. There was substantial variability in measurements between ellipsometers, but there was no clear distinction in measured oxide thickness with respect to HF etching. It should be noted that the repeatability of the oxide characteristics by this method of preparation are not expected to be repeatable, and that it may be desirable to develop a process or coating with a more stable and repeatable surface (e.g. a Si_3NO_4 surface).

Table 4-2: Native oxide film thickness measurements

Measurements are Before/After HF etch	*Woollam Ellipsometer*	*Nanospec Film Analyzer 3000*	*Plas-Mos Ellipsometer*
Average (Å)	47 / 44	74 / 65	79 / 89
Standard Deviation (Å)	NA / 6	19 / 6	NA / 9

Mica Preparation

Commercially available mica (laminar muscovite sheet) was used as a dielectric insulator to prevent contamination of the CPD probe tip by the oil sample under investigation. A

thin sheet approximately 40μm thick was cleaved from a thicker sheet. The thin sheet was cut into 1cm by 1cm squares. Although thinner sheet would increase the sensitivity of the CPD probe, it was determined through experience that sheets of mica 25μm thick or less proved to be too fragile for repeated use. Additionally, very thin sheets were not rigid enough to adequately maintain uniform spacing under the probe tip when downward pressure was applied.

Oil Sample Preparation

Commercially available engine oils and engine oil base stock were used in the experiments. The engine oils evaluated were Pennzoil 10W-30 and 10W30 Mobil1. The samples were purchased at an commercial auto parts supplier. In order to evaluate the sensitivity of the osCPD sensor to various changes in the oil, samples were prepared either by thermal aging, or by addition of ferric chloride. Ferric chloride is a typical additive used by commercial testing labs to characterize spectroscopic test systems.

Thermal Aging

The intent of thermal aging is to simulate and accelerate the breakdown of oil that might occur in a typical engine application. Thermal aging of oil (oxidation and associated degradation processes) follows an Arrhenius relation with respect to operating temperature. The Arrhenius relation is given as

$$r = Ae^{\left(-\frac{E_a}{kT}\right)} \tag{4.1}$$

where

r is the reaction rate,

A is a thermal constant of proportionality specific to the reactants

E_a is the activation energy

$k = 8.617 \times 10^{-5}$ eV/K is Boltzmann's constant, and

T is the temperature of the system in degrees Kelvin

A commonly accepted acceleration factor is that for every 10C increase above nominal operating temperature, oxidation rates double. In this fashion, if one assumes an average operating temperature for a typical engine, acceleration factors based on thermal aging temperature can be used to calculate equivalent aging times. Equivalent aging times for the range of temperatures used in this investigation are given in Table 4-3. The times in the table represent the nominally equivalent number of hours that the same oil would need to be run in an engine operating at 100C in order to achieve the same level of equivalent thermal aging.

Table 4-3: Calculated equivalent aging time for thermally aged engine oil

Aging Temperature (Oil Sample)	*Acceleration with respect to 100C op. temp.*	*30 minute aging time*	*60 minute aging time*	*90 minute aging time*
160C (Pennzoil 10W30)	64 X	16 hrs	32 hrs	48 hrs
200C (10W30 Mobil1)	1024 X	512 hrs	1024 hrs	1536 hrs

This accelerated aging approach neglects significant effects that might be encountered under actual engine operating conditions. These include localized heating, influx of contaminants such as coolants and suit, and introduction of wear particles and other debris. Although the accelerating aging technique itself and the underlying assumptions used to calculate equivalent aging are simplistic, the intent of the thermal aging

experiments was to create representative samples with a known processing history, not necessarily to replicate actual engine wear. Additionally, all osCPD and third-party characterization measurements were made on the same oil samples. Therefore, errors in reporting of the equivalent aging do not substantially alter the conclusions drawn by comparison of the osCPD measurements to third-party characterizations.

As shown in Figure 4-4, thermal aging was accomplished by heating the oil in an Erlenmeyer flask on a hotplate. The flask was left open to the lab environment throughout the heating process. A magnetic stir driven by the hotplate agitated the oil to encourage oxidation. A surface vortex due to the rotation of the stir can also be seen in the figure. The temperature of the oil was measured using an infrared thermometer. The hotplate temperature was adjusted as necessary to maintain the desired aging temperature as measured with the infrared thermometer.

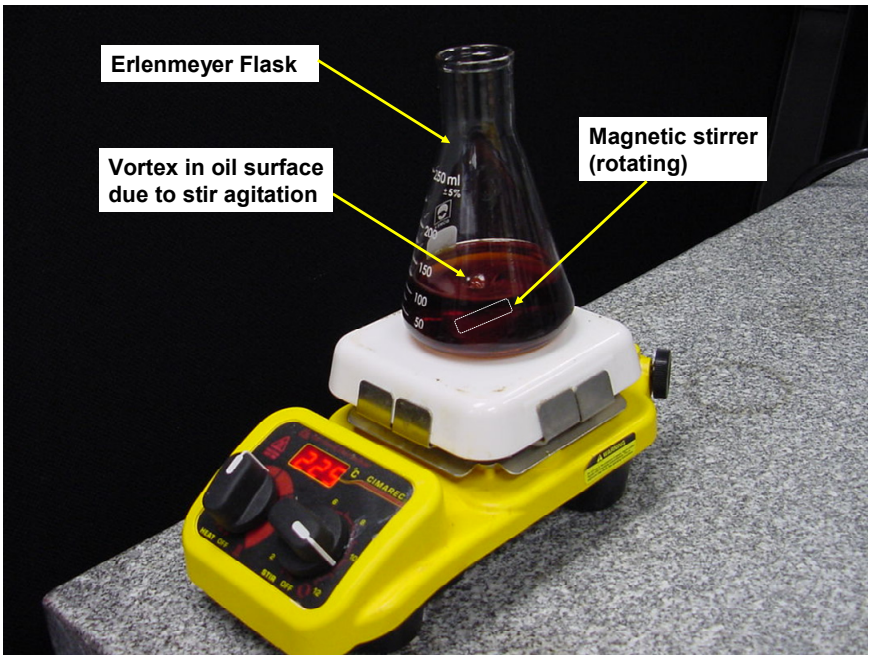

Figure 4-4: Accelerated thermal aging of oil samples

Ferric Chloride

Oil-soluble ferric chloride is commonly used in commercial oil-analysis laboratories to calibrate spectroscopic test equipment. A benefit of using ferric chloride is that very precise concentrations of atomic iron can be added to oil in solution. A major drawback of using ferric chloride in test equipment evaluation is that the oil-soluble formulations are highly proprietary; precise chemical formulations are not made publicly available by the suppliers.

The ferric chloride samples used in these experiments were prepared by Analysts, Inc., located in Norcross, Georgia. Analysts is a commercial testing laboratory that provides lubricant analysis services to industrial segments including manufacturing plant equipment and transportation fleet equipment. Ferric chloride in an oil solution of known concentration was blended with a base stock oil to obtain the desired concentration of 1000ppm. The base stock that was contained a "typical" additive package that included anti-oxidants, dispersants, and rust inhibitors. The precise formulations of the additive packages are also proprietary, although general compositions are known. Mixing the concentrated ferric chloride solution with the base stock resulted in a dilution of the ferric chloride to 1000pm in the base stock. This also resulted in dilution of the additive package in the base stock since the additive package is not present in the ferric chloride solution.

The intent of using the ferric chloride solution was to create two otherwise identical samples of base stock, differing only in iron concentration. However, as a result of the

volume of solution required to raise the iron content in the base stock, significant dilution of the additive package in the base stock also occurred.

Addition of Glass Spacers

After the individual oil samples had been prepared, they were added to vials containing pre-measured quantities of glass spacer beads. As described in Chapter 3, the glass spacers were highly spherical and highly uniform in average diameter. Three spacer diameters were investigated: 38μm, 75μm, and 150μm. Since the glass spacers might affect the capacitance of the sample if present in high concentration, an attempt was made to normalize the concentration of spacers by weight and diameter. The intent was to achieve nominally uniform area concentration of glass spacers when the oil was placed in the silicon-mica sandwich. This was achieved by calculating the volume-to-area ratio for each spacer size, and then measuring a pre-determined amount of each spacer into pre-labeled vials for each oil sample. While the effort was rational in theory, in practice the spacer beads precipitated out of the oil samples very rapidly. The samples were stirred vigorously prior to placement on the silicon substrate, and visual inspection for spacer bead uniformity was made prior to placing the mica on top of the oil samples.

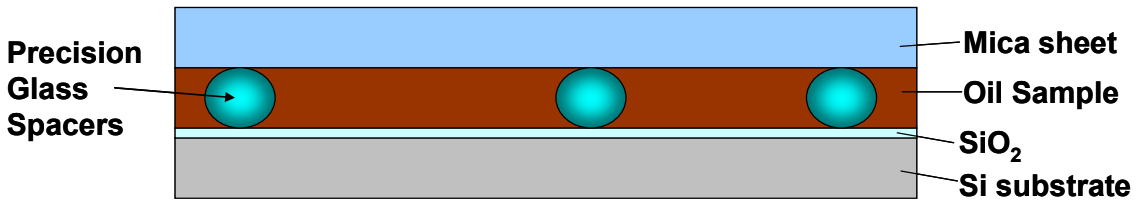

Figure 4-5: Schematic illustration of glass spacer beads in oil sample assembly

Substrate Cleaning and Loading of the Test Samples

The silicon and mica surfaces were cleaned immediately prior to adding the oil samples. After an initial wipe using a Kimwipe and petroleum ether to remove excess oil and spacers from prior experiments, the silicon and mica were placed in a petroleum ether bath as shown in Figure 4-6. The bath used a magnetic stir to agitate the petroleum ether. The silicon and mica were allowed to sit in the bath for 1-2 minutes prior to removal. After removal from the bath, the silicon and mica were allowed to air dry, and then were rinsed with methanol using a spray bottle and Kimwipe. The silicon and mica were again allowed to air dry.

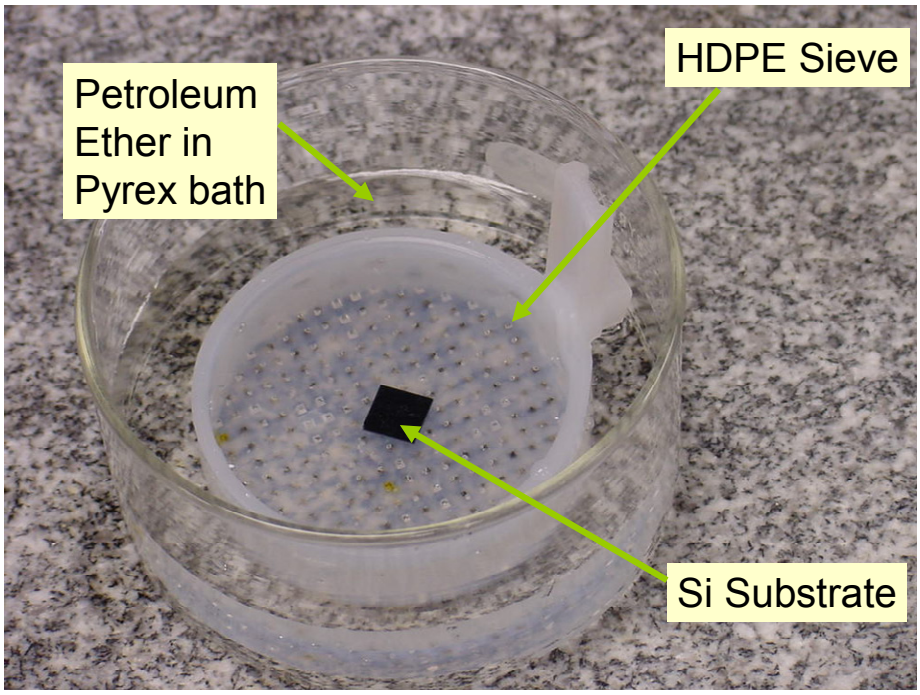

Figure 4-6: Petroleum ether bath used to clean silicon substrate and mica

After the silicon and mica had been cleaned, the oil sample was placed on the silicon substrate using a glass pipette. Separate pipettes were used for each oil sample to avoid cross-contamination of glass spacers or of oil chemistry. The pipettes were also used to

adjust glass spacer bead distribution on the silicon substrate surface as necessary. In experiments that used multiple sets of silicon and mica pairs, the silicon-mica pairs were strictly maintained throughout the given set of experiments. Also, the vertical orientation of the silicon substrate was carefully maintained. That is, the same surface on which the oil samples were place was used throughout a set of experiments.

Once assembled, the silicon-oil-mica assembly was placed onto the test fixture. The sample was located directly over the light aperture by alignment pins in the top surface of the test fixture. The CPD probe was then lowered into position, and gentle down-force was applied by hand to encourage expulsion of excess oil from between the mica and silicon. As illustrated in Figure 4-5, this ensured that the oil film thickness was controlled by the glass spacer bead diameter.

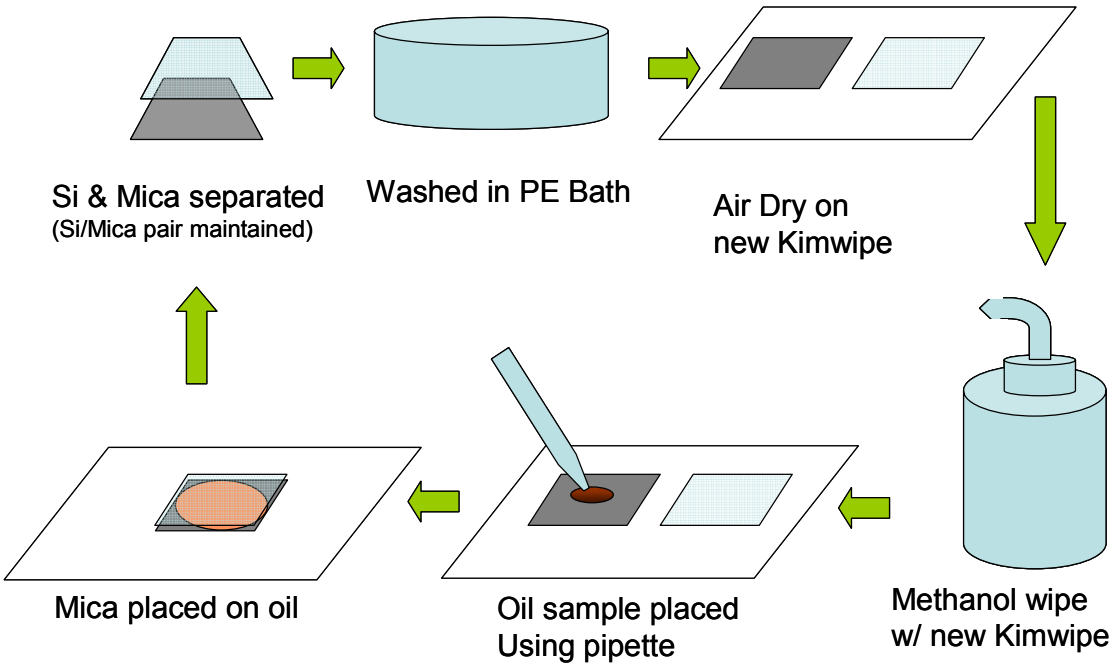

Figure 4-7: Schematic illustration of sample preparation procedure

Test Fixture Configuration

The optical stimulus applied to the back surface of the silicon substrate had three selectable parameters: photon wavelength, intensity, and frequency of intensity modulation. The wavelength of the incident light was controlled by placing an optical bandpass filter over the end of the light pipe from the visible light source. This restricted light incident on the silicon substrate to a selected central wavelength plus or minus 20nm. The intensity was controlled by the Fostec visible light source. Intensity measurements for a given bandpass filter were made by placing the optical power meter head over the aperture in the test fixture. In this way, a measurement for light actually incident on the back surface of the silicon substrate was obtained. Although this measurement was not performed in-situ, measurements of the light intensity before and after experiments confirmed the stability of the light source.

The frequency of intensity modulation was controlled by the Thorlabs optical chopper. The chopping frequency was set directly using the control unit for the chopper. The chopping frequency is the rate at which the light cycles on and off as individual chopper blades pass over the aperture in the test fixture. The rate of transition of light intensity is a function of the geometry of the test fixture and chopper blade. A chopper with few blades but chopping at the same frequency would actually have a faster intensity ramp rate since the chopper blades must necessarily be rotating at a faster angular velocity to attain the same chopping frequency. The faster angular velocity translates to a faster linear velocity of the chopper blade as it crosses the aperture. Locating the aperture farther from the center of rotation of the optical chopper has the same effect since the

linear velocity is the product of the angular velocity and the radial distance. Both of these effects were utilized to maximize the rate of intensity transition.

Data Acquisition Software Configuration

Once the oil sample was placed in the test fixture and the optical intensity, chopping frequency, and wavelength had been set, the system was ready to take measurements. Data acquisition was controlled by the CPD-Scan data acquisition software. The front-panel GUI for this software is shown in Figure 4-8. The primary control parameters that were set using the data acquisition software are listed and defined in Table 4-4.

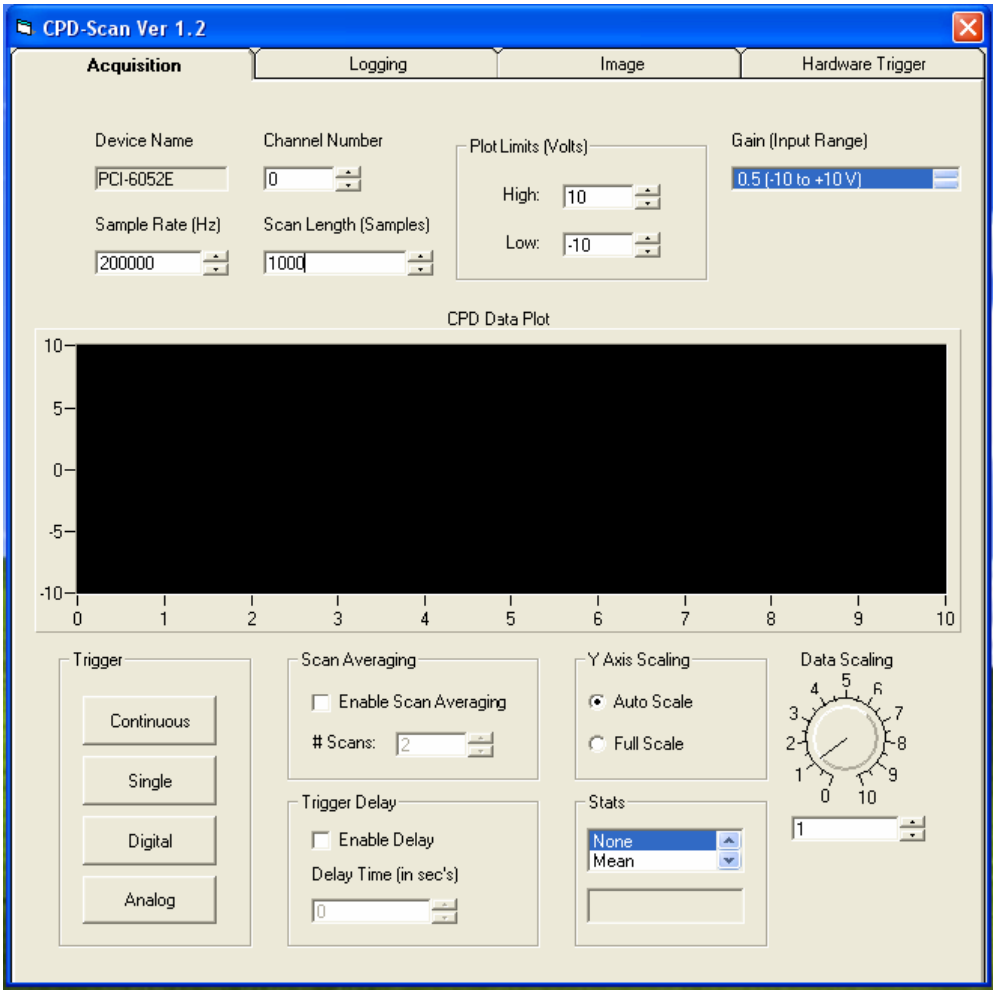

Figure 4-8: CPD-Scan data acquisition software

Table 4-4: CPD Scan software typical data acquisition settings

Parameter	*Definition*	*Range (typical setting)*
Sample Rate	This is the rate at which the data acquisition hardware sampled the output voltage from the CPD probe	1Hz – 200kHz (200kHz)
Scan Length	Data was acquired in multi-point strings. Scan length defines how many successive data points are captured in a given string.	1 – 10,000 (600 – 2000)
Digital Trigger	This enabled the software to initiate data acquisition based on a digital trigger signal from the data acquisition hardware. In this case, the trigger signal was the 5V TTL signal provided by the optical chopper.	ON / OFF (ON)
Scan Averaging	Determines whether a single data string is captured, or whether a specified number of subsequent strings are averaged prior to being written to file	ON / OFF (ON)
# Scans	This determined the number of successive data strings that were captured and averaged	2 – 100 30 / 100

The frequency stability of the chopper in conjunction with the digital trigger output allowed the data acquisition system to operate as a lock-in amplifier. A minimum of 30 and up to 100 waveforms were typically averaged during experimentation. The resulting signals obtained were therefore extremely stable and virtually free of noise. This was particularly important in that the data acquisition software was able to filter the thermal noise present at the first stage amplifier input due to the use of a resistor as the CPD probe tip. Since thermal noise is white noise and therefore random[38,39], averaging multiple waveforms has the effect of removing the thermal noise from the osCPD signal, leaving only the desired osCPD waveform.

CHAPTER 5

EXPERIMENTAL RESULTS

Chapter 4 presented the experimental methodology employed in conducting experiments with the osCPD sensor. This chapter will present data that was obtained from the osCPD sensor in the evaluation of thermally aged engine oil samples. The primary objective of experimentation was to determine the fundamental mechanism of osCPD signal generation. As illustrated in Figure 5-1, successive experiments built upon the findings and observations from prior experiments until a conclusive understanding of the mechanism of signal generation was reached. The final series of experiments allowed validation of the predictive model created for the osCPD sensor. A predictive sensor response model is developed in Chapter 6 and compared with experimental results.

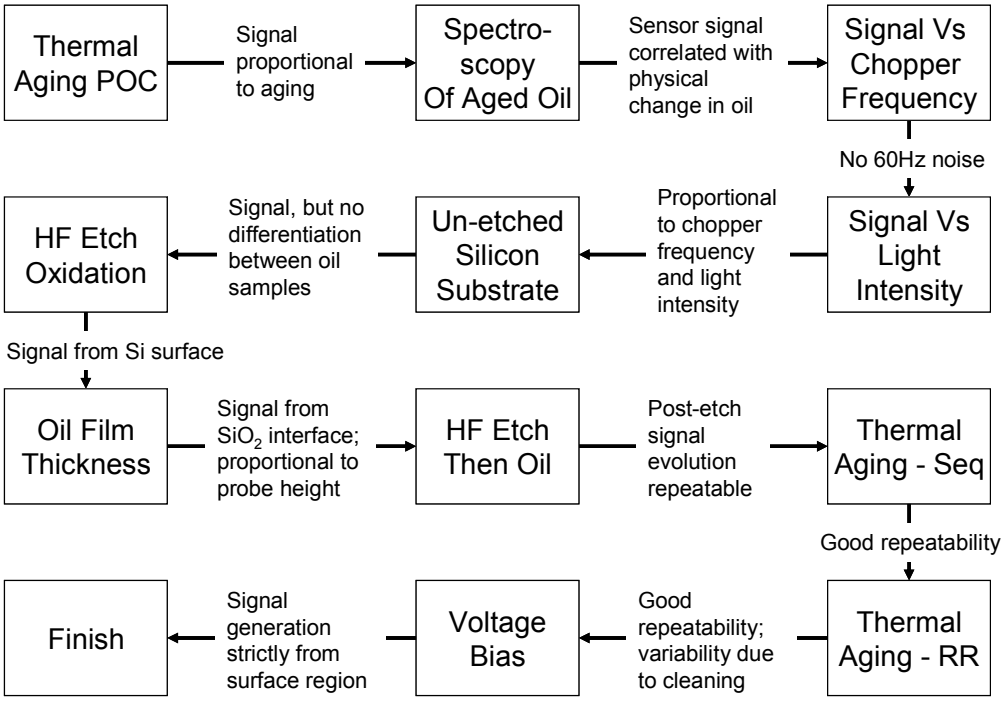

Figure 5-1: Experimental flowchart

Thermal Aging Proof of Concept

An experiment was conducted to determine the capability of the osCPD sensor to detect thermal aging in commercial engine oil. In this experiment, Pennzoil 10W-30 motor oil was thermally aged at 160C, and oil samples were drawn at 30 minute intervals. The samples were placed in pre-labeled sample vials using individual pre-marked pipettes for each oil sample to prevent cross-contamination of the samples.

The test apparatus used was similar to that described in Chapter 3 with several exceptions. Rather than the digital hotplate, a Teflon-coated deep fryer with electronic temperature control was used to thermally age the oil, and a QCept A250F500 CPD probe was used rather than the custom-built probe described in Chapter 3. Also, a prior-generation test fixture was used that was functionally equivalent to that shown in Chapter 3. Major test parameters are listed in Table 5-1.

Table 5-1: Experimental parameters for thermal aging proof of concept

Equipment/ Parameter	*Description / Settings and comments*
Oil Sample	Pennzoil 10W-30; thermally aged @ 160C
Glass Spacers	None
CPD Probe	QCept A250F500
Light Source	450 nm, +/- 10nm; 0.97mW intensity
Optical Chopper Settings	10-blade chopper; 400 Hz chopping frequency
Voltage Bias	None / grounded

A single (111) p-type silicon substrate and matching mica spacer were used throughout the entire set of experiments. The silicon substrate and mica were washed with

petroleum ether using a Kimwipe, and then allowed to air dry. This was followed by rinsing with methanol and Kimwipe. The optical chopper was set to 400 Hz, and the light intensity was set to maximum. The DAQ was set to a 100kHz sampling rate using the digital trigger from the optical chopper. The sample scan length was set to 400 data points, which corresponded to approximately two (2) complete CPD waveforms. The data acquisition software was set to average 100 sample scans to provide a nearly noise-free signal as seen in Figure 5-1. The peak-to-peak voltage of the CPD signal, V_{PP}, was calculated from the scanned waveform data, and is presented in Figure 5-2.

As seen in Figure 5-1, the osCPD sensor showed good sensitivity to thermal aging of the oil samples. The waveforms decrease monotonically in magnitude as a function of thermal aging time. Additionally, the individual waveforms show excellent signal-to-noise ratio. A single typical osCPD waveform exhibits a positive peak and a negative peak. As shown in Figure 5-2, the first peak (positive peak) corresponds to the chopper blade transitioning over the aperture (when the light turns "off"). The second peak (negative peak) corresponds to the chopper blade transitioning off of the aperture (when the light turns "on").

Although similar in form and magnitude, closer inspection of the peaks shows that they are not symmetric: The peak when the light turns "on" has a steeper ramp rate due to the minority carrier diffusion process that drives the signal. The peak when the light turns "off" has a slightly longer response due to the slower time constant of the recombination process and decay of the space charge region at the top surface of the silicon substrate.

These processes will be discussed in further detail in Chapter 6. Inspection of the waveform also indicates that the signal after the positive peak (after the light turns off) just barely settles before the negative peak begins (when the light turns on). This suggests that chopping at a sufficiently high frequency would lead to signal aliasing due to the response time of the system.

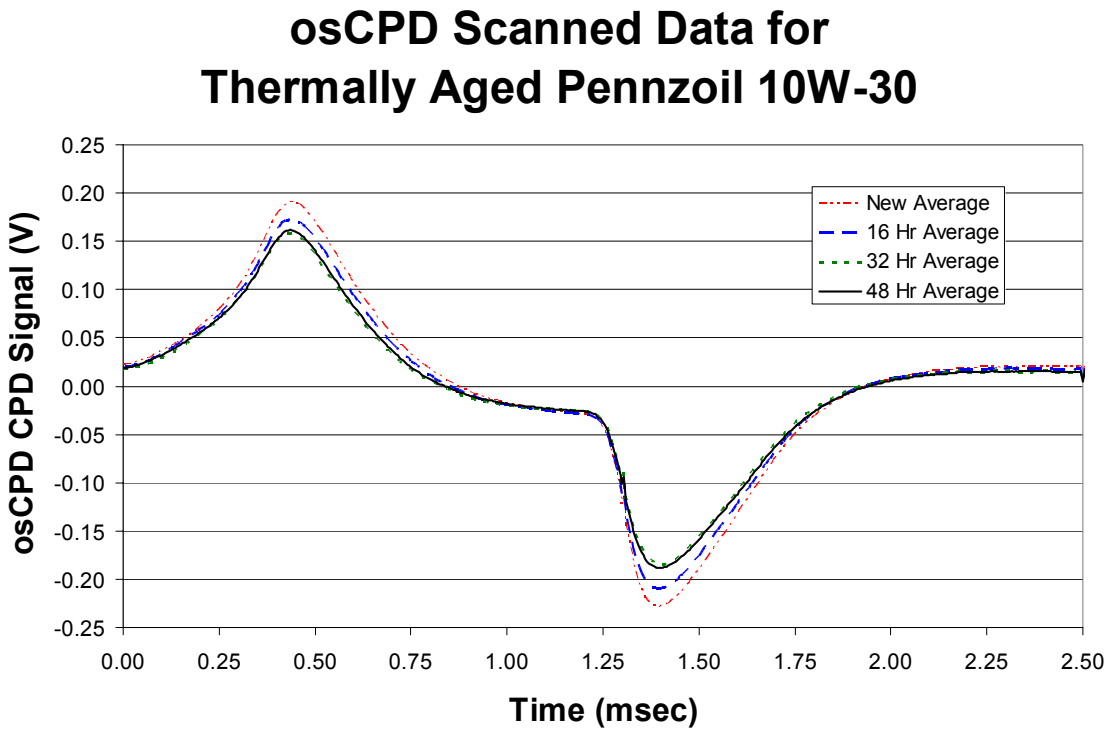

Figure 5-2: Scanned waveform data for thermally aged Pennzoil 10W-30

The waveforms presented in Figure 5-2 were evaluated for peak-to-peak voltage, and the resulting values are plotted in Figure 5-3. The correlation between time of thermal aging and decreasing osCPD signal is again evident. The osCPD signal appears to saturate after 32 hours of equivalent thermal aging (60 minutes of aging at 160C). Given the

small standard deviation between measurements, this is not likely due to measurement resolution, but is in fact a saturation of the osCPD sensor response due to some chemical process asymptotically approaching a final value in the oil (e.g. depletion of some additive).

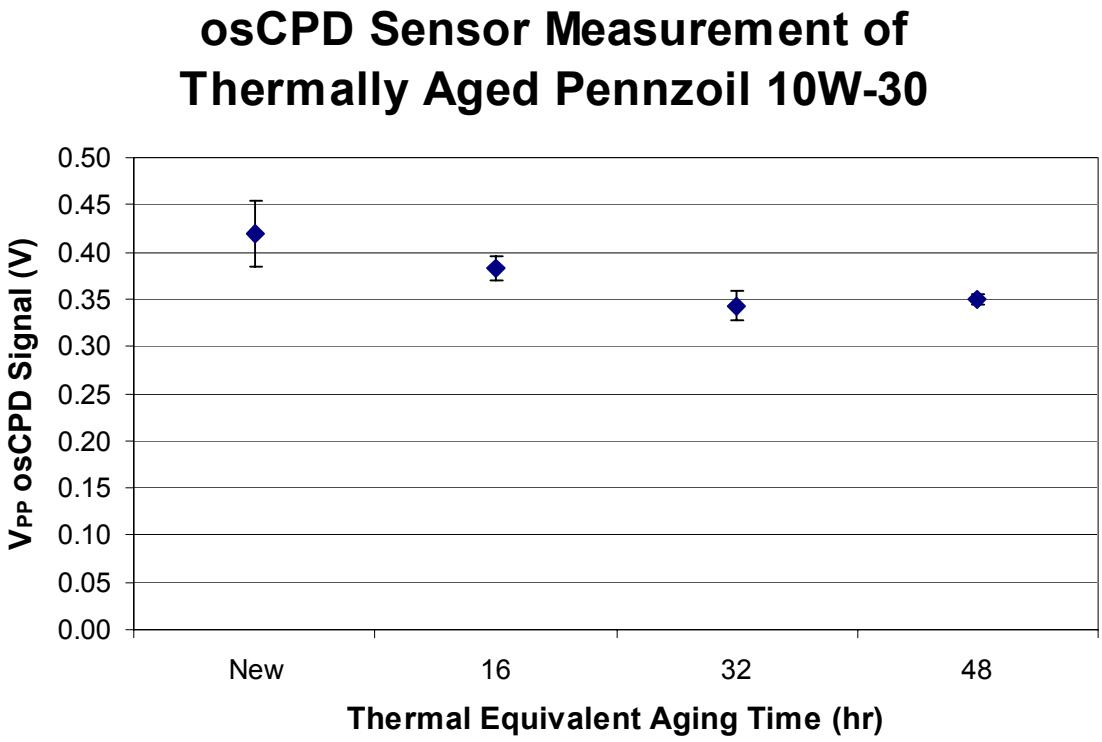

Figure 5-3: Peak-to-peak voltage data for thermally aged Pennzoil 10W-30

The primary conclusions from this experiment were that the osCPD sensor is capable of detecting thermal aging in oil, and that it shows good resolution with respect to oil sample differentiation. Also, the output signal is inversely proportional with respect to aging time until some saturation event occurs in the oil.

Thermal Aging Analysis – Visible Light Spectroscopy

In order to determine whether some physical change occurred in the oil samples as a function of thermal aging, spectrographic measurements were performed. Visible absorption spectra for the thermally aged 10W30 Mobil1 samples were obtained using the apparatus shown in Figure 3-13. As seen in Figure 5-4, light absorption decreases with increased thermal aging for the range of thermal aging shown. This would suggest some physical change is taking place in the oil whereby the concentration of some species responsible for absorption is being depleted or consumed. The trend in this data correlates with the trend in the osCPD data. It should be noted that the absorption for all wavelengths increases gradually beyond 1024 hours of equivalent aging.

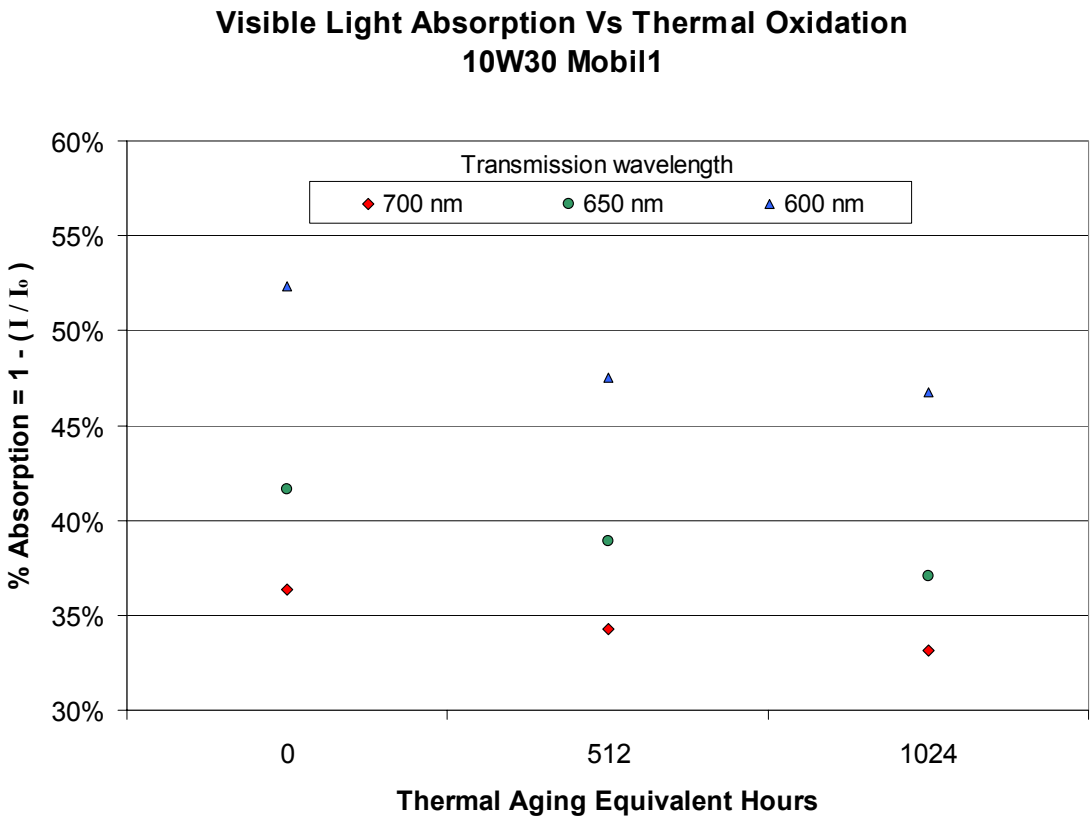

Figure 5-4: Visible light spectroscopy of 10W30 Mobil1 Samples

osCPD Signal Versus Chopping Frequency

A set of measurements was conducted with a 7-slot chopper blade in which the chopping frequency was varied between 15Hz and 135Hz in 1Hz increments. The intention of the experiment was to determine the effect of chopping frequency on signal amplitude, and to determine the sensitivity of the osCPD test system to 60Hz noise that might be present from power supplies, ambient environment, etc. As seen in Figure 5-5, the sensor does not show signs of sensitivity to 60Hz noise or resonance at multiples thereof, nor is there any evidence of noise at any other frequencies (the only exception being a single outlying point at 55Hz which was likely due to experimental error). Also evident in the data is the proportional dependence of the osCPD signal on chopping frequency. This is due to the faster rate of transition from minimum to maximum light intensity that accompanies the faster rotational speed. Since the transition time of the chopper blade over the aperture is inversely proportional to the linear velocity of the blade past the aperture, for a fixed radial location of the aperture with respect to the chopper blade, higher rotational speeds translate directly into higher linear velocities, faster intensity transitions, and thus larger osCPD signals. This was confirmed by a second set of measurements shown in Figure 5-6 in which different chopper blades were used: 2-blade, 7-blade, and 10-blade. All three blades had a 50% duty cycle. The osCPD signal increases with reduced number of chopper blades since the radial velocity necessarily increases with fewer blades.

Table 5-2: Experimental parameters for chopping frequency experiment

Equipment/ Parameter	*Description / Settings and comments*
Oil Sample	None
Glass Spacers	None
CPD Probe	Custom-built as described in Chapter 3
Light Source	Source 700 nm, +/- 20nm; 75μW intensity
Optical Chopper Settings	2,7, & 10-blade chopper; 15-1000 Hz chopping frequency
Voltage Bias	None / grounded

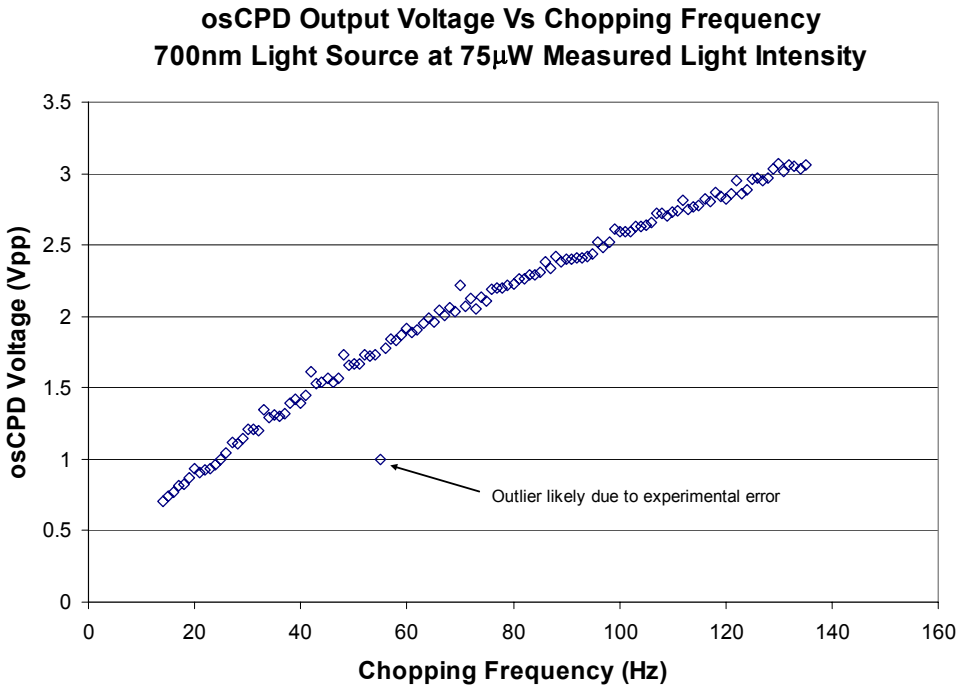

Figure 5-5: osCPD signal versus chopping frequency

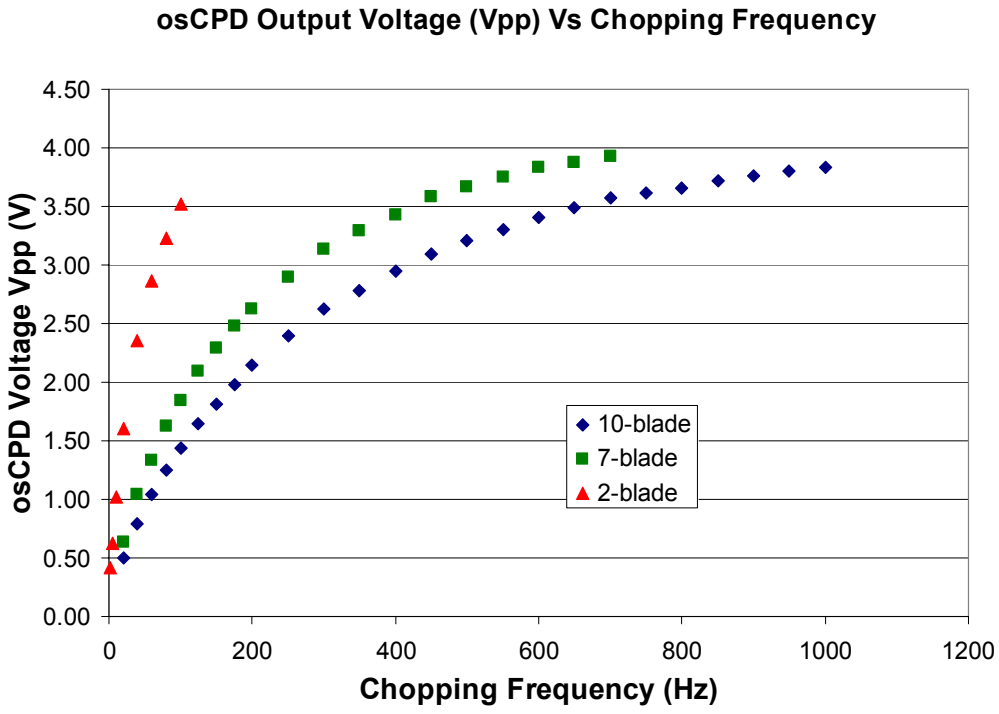

Figure 5-6: osCPD signal versus chopping frequency and number of chopper blades

osCPD Signal Versus Light Intensity and Chopping Frequency

A set of measurements was conducted in which the incident light intensity on the back surface of the silicon substrate was varied, and the chopping frequency was varied between 60Hz and 1000Hz (in 100Hz increments above 100Hz). The intention of the experiment was to determine the influence of light intensity on the signal amplitude, and to determine whether this was independent of chopping frequency.

The measurements were performed on a bare silicon substrate (no oil sample) with the usual mica spacer. The light intensity was set at either maximum or minimum intensity prior to making a measurement. As seen in Figure 5-7, the osCPD signal is in all cases larger for the higher intensity setting than for the lower intensity. It can also be seen that intensity and chopping frequency are independent factors for this range of testing. That is, the ratio of the osCPD signal between high and low intensity remains constant throughout the range of frequencies evaluated, even after the signal has saturated. As expected, the sensor signal saturates above some frequency, in this case approximately 400Hz.

Table 5-3: Experimental parameters for chopping frequency and intensity experiment

Equipment/ Parameter	*Description / Settings and comments*
Oil Sample	None
Glass Spacers	None
CPD Probe	QCept A250F500
Light Source	450 nm, +/- 10nm; 0.97mW & 0.42mW intensity
Optical Chopper Settings	10-blade chopper; 15-1000Hz chopping frequency
Voltage Bias	None / grounded

The key outcomes of this experiment were that the osCPD signal was shown to be proportional with light intensity, and that the light intensity and chopping frequency are independent variables with respect to the osCPD signal.

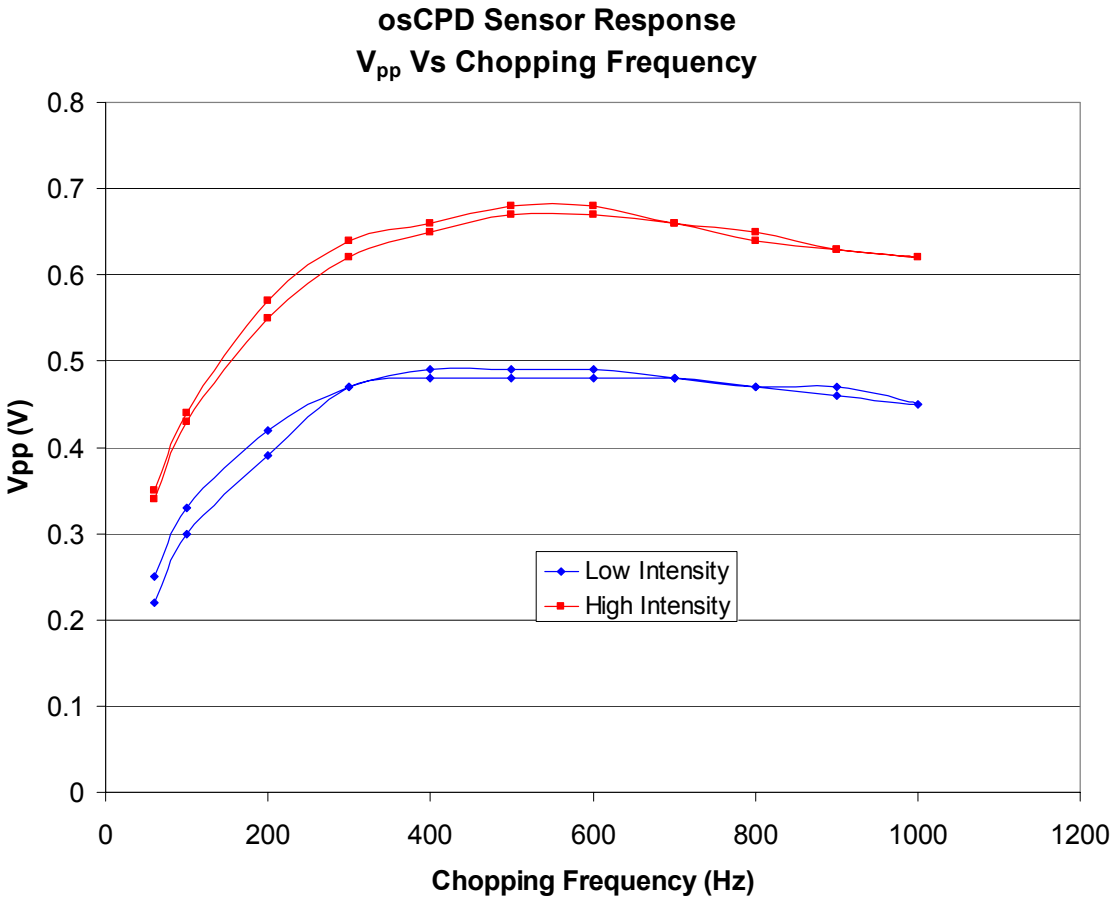

Figure 5-7: osCPD signal versus light intensity and chopping frequency

osCPD Measurements using Un-Etched Silicon Substrates

Experiments were conducted using silicon substrates that had not been etched in HF. These experiments were conducted to determine the influence of the HF etching process on the osCPD signal. Use of HF is extremely dangerous, and therefore not desirable. Additionally, the oxidation process after HF etching was not controlled in these experiments, and so led to a possible source of experimental variation. Thermally aged Pennzoil 10W-30 samples were evaluated using the sample preparation and measurement procedure described previously with the only exception being that the silicon substrates were not etched in HF prior to use.

In all cases, the osCPD signal exhibited the typical waveform as shown, for example, in Figures 5-2, 5-12, and 5-14. However, there was no differentiation in the measurements between oil samples: The peak-to-peak voltage was constant regardless of oil sample. Although it is known that the capacitance of oil samples changes as a function of oxidation, it is not suspected that change in capacitance is a contributory mechanism to sample differentiation for the set of oil samples investigated in this research. This is based on the inability of the sensor to differentiate between samples in the absence of HF etching. This may be due to a relatively small change in capacitance of the oil samples over the range of thermal aging evaluated. Since no difference in osCPD measurements between samples was observed for the un-etched silicon substrates, it was further assumed that changes in capacitance of the oil samples (either in the bulk or at the substrate surface) did not contribute to measurements made on etched silicon substrates. This assumption was explicitly invoked in the models developed in Chapter 6.

HF Etch and osCPD Signal Evolution in Air

An experiment was conducted whereby a silicon substrate was etched in HF, and then monitored continuously using the osCPD sensor. The intention of the experiment was to determine the effect of the HF etch on the silicon substrate. The silicon substrate was first etched in HF until hydrophobic, cleaned with petroleum ether and methanol in the usual fashion, and then mated with a mica sheet. The silicon-mica stack was then placed in the osCPD test fixture without an oil sample. osCPD measurements were begun on the silicon substrate approximately 30 minutes after the HF etch had been performed. Subsequent measurements were made at approximate 10 minute intervals for the next three hours. The sample was not moved, the test fixture was not disturbed between measurements, and no changes were made to the data acquisition hardware or software.

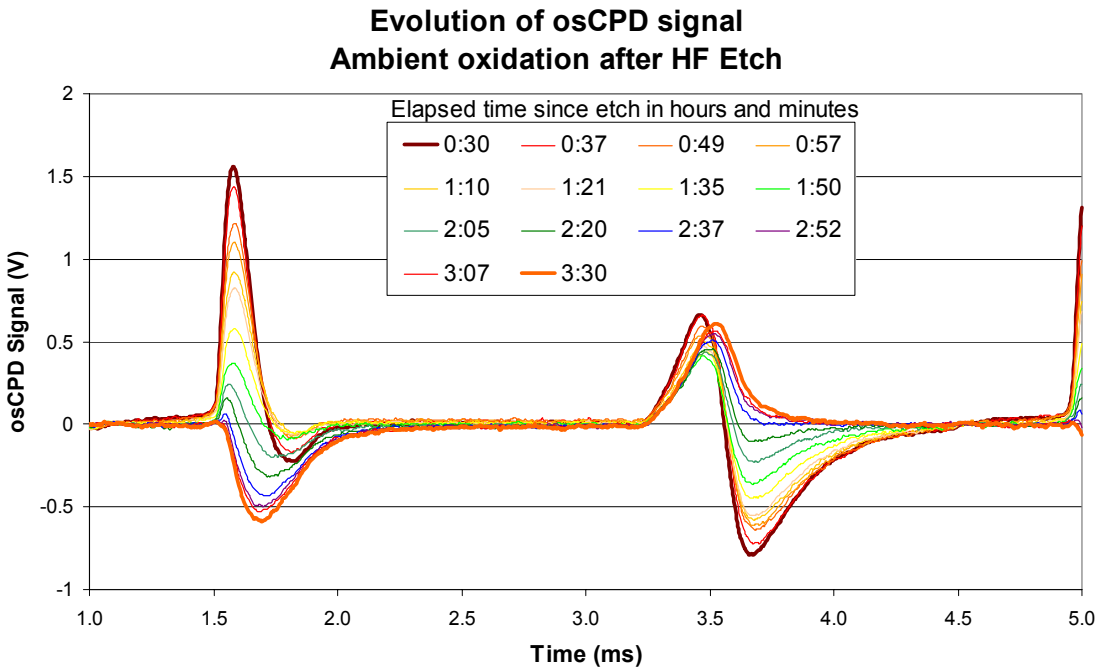

Figure 5-8: osCPD signal evolution after HF etch – oxide formation in air

As shown in Figure 5-8, the osCPD signal changes significantly within the first three hours after the HF etch, and eventually stabilizes to a more ”typical” osCPD waveform. For clarity, the beginning and ending osCPD waveforms from Figure 5-8 are shown in Figure 5-9 with all intermediate waveforms removed. Since the only change occurring in the osCPD test system over this period of time is the oxide formation at the silicon surface, it can be inferred that the osCPD signal generation is occurring at the surface of the silicon. It can also be observed that the signal must be generated at the top surface of the silicon substrate: In prior experiments, the oil samples are only placed on the top surface of the silicon, but there is clear differentiation between samples.

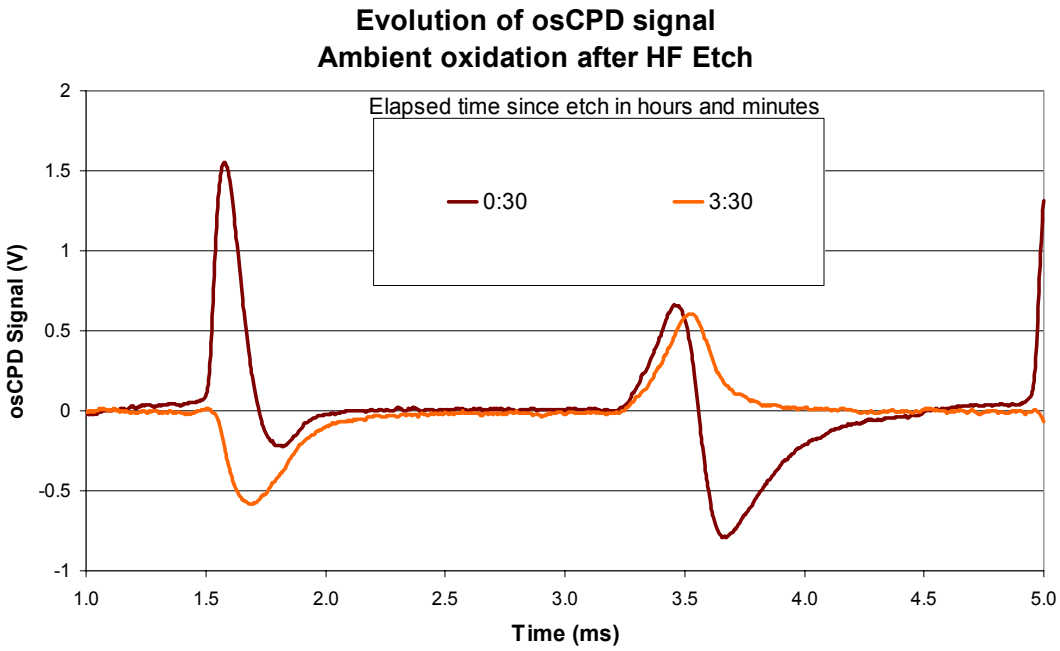

Figure 5-9: osCPD signal evolution after HF etch – initial and final waveform

Although a complete explanation of the osCPD waveform evolution is beyond the scope of the current investigation, it is believed to be associated with the evolution of a trapped charge layer at the Si-SiO_2 interface during room-temperature oxidation.

Thermal Aging & Variable Oil Film Thickness

An experiment was conducted using precision glass spacer beads to control the film thickness of the oil samples during evaluation. The intention was to evaluate the effect of oil film thickness on the osCPD sensor signal. In this experiment, Pennzoil 10W-30 motor oil was thermally aged at 160C. After aging, precision glass spacers beads were mixed with the oil. Three spacer diameters were investigated: 38 μm, 75 μm, and 150 μm. Oil without spacer beads added was also tested. In an effort to normalize the fractional area occupied by the spacer beads in each oil sample, the diameter to weight ratio of each spacer was utilized to calculate the amount of spacer to add to a given oil sample. The spacer beads were placed in new pre-marked vials for each thermally aged oil sample. Using marked pipettes, a measured, consistent volume of oil was added to the vials containing the spacer beads. Major test parameters are listed in Table 5-4.

Table 5-4: Experimental parameters for thermal aging and variable oil film thickness

Equipment/ Parameter	*Description / Settings and comments*
Oil Sample	Pennzoil 10W-30; thermally aged @ 160C digital hotplate
Glass Spacers	38μm, 75μm, and 150μm
CPD Probe	QCept A250F500
Light Source	450 nm, +/- 10nm; 0.97mW intensity
Optical Chopper Settings	10-blade chopper; 400 Hz chopping frequency
Voltage Bias	None / grounded

A single (111) p-type silicon substrate and matching mica spacer were used throughout the entire set of experiments. The silicon substrate and mica were soaked in an agitated petroleum ether bath for several minutes to remove the prior oil sample. The optical

chopper was set to 400 Hz, and the light intensity was set to maximum. The DAQ was set to a 100kHz sampling rate using the digital trigger from the optical chopper. The sample scan length was set to 400 data points, which corresponded to approximately two (2) complete CPD waveforms. The data acquisition software was set to average 100 sample scans to provide a nearly noise-free signal. The peak-to-peak voltage of the CPD signal, V_{PP}, was calculated from the scanned waveform data, and is presented in Figure 5-10.

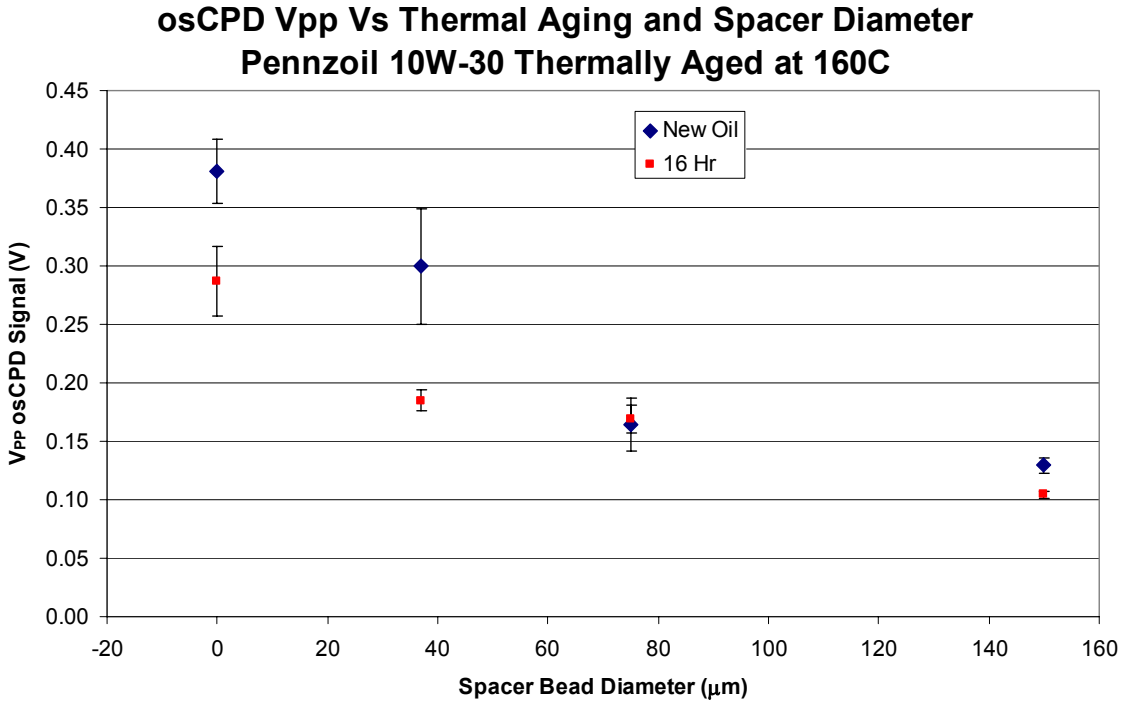

Figure 5-10: osCPD data for thermal aging and varying oil film thickness

As expected, the osCPD peak-to-peak voltage decreased as the oil film thickness increased. This confirms that the probe is sensing the silicon surface, and not the bulk of the oil or some other intermediate interface. It can also be seen that in all cases except for the 75µm spacer, the osCPD signal decreased significantly after thermal aging. This

is consistent with the prior thermal aging experiment. The magnitude of the peak-to-peak voltage (V_{PP}) is also similar to the proof-of-concept thermal aging experiments. The new oil without spacer beads in the current set of experiments showed V_{PP} = 0.38V versus V_{PP} = 0.42V in the prior experiment.

The thermally aged oil in the current experiment was aged for 30 minutes at 160C, and roughly repeats the aging of the 16-hour equivalent aging sample from the proof-of-concept experiment. The 16-hour oil without spacer beads in the current set of experiments showed V_{PP} = 0.29V versus V_{PP} = 0.38V in the prior experiment. Although the magnitude of the two points are not in agreement, it must be recognized that the conditions of thermal aging were not likely identical. More importantly, the trend of a decreasing osCPD signal is maintained between the two experiments.

Another conclusion drawn from this set of experiments is that both signal magnitude and signal differentiation were favorably large for the 38μm glass spacer beads. For this reason, 38μm glass spacers were chosen as the standard size for all subsequent experiments.

HF Etch and osCPD Signal Evolution in Oil

The prior post-etch signal evolution experiment was repeated, but this time new 10W30 Mobil1 was applied to the silicon substrate following the usual sample cleaning and preparation procedure. The intention of this experiment was to determine the influence of the oil samples on the osCPD signal evolution after HF etching.

Table 5-5: Experimental parameters for surface charge evolution after HF in oil

Equipment/ Parameter	*Description / Settings and comments*
Oil Sample	New 10W30 Mobil1
Glass Spacers	38μm
CPD Probe	Custom-built as described in Chapter 3
Light Source	Source 600 nm, +/- 20nm; 1.67mW intensity
Optical Chopper Settings	7-blade chopper; 290 Hz chopping frequency
Voltage Bias	None / grounded

The silicon substrate was first etched in HF until hydrophobic, cleaned with petroleum ether and methanol in the usual fashion, and then mated with a mica sheet. The silicon-mica stack was then placed in the osCPD test fixture with a new 10W-30 Mobil1 oil sample that contained 38μm glass spacers. After a measurement was made, the sample stack was removed from and returned to the test fixture for a repeat measurement. This was repeated six times per oil sample. After the first set of six measurement was made, the sample assembly was allowed to rest for 10 minutes, and then another set of 6 measurements was made. These are shown in Figure 5-11 as "New Oil-1 Avg," and "New Oil-2 Avg." The sample stack was then disassembled, and the silicon substrate and mica sheet were cleaned using the agitated petroleum ether bath followed by a

methanol wipe. The oil sample was then re-loaded, and the next set of measurement was taken. The data is shown as “New Oil-3 Avg,” and ”New Oil-4 Avg.” This was repeated a final time and resulted in the waveforms “New Oil-5 Avg,” and ”New Oil-6 Avg.”

As shown in Figure 5-11, the osCPD signal showed a nearly identical waveform evolution to that described in the air-only experiments above. It is critical to note that this waveform was detected using a different CPD probe from that shown previously, and that the silicon substrate in this case was repeated removed from the fixture, cleaned, and replaced. As seen in Figure 5-11, the osCPD waveform was fairly stable within a set of measurements for a given oil sample, but changed substantially after the petroleum ether bath and methanol wipe. The evolution of the waveform seems to have been accelerated by the repeated cleaning and sample-loading cycles.

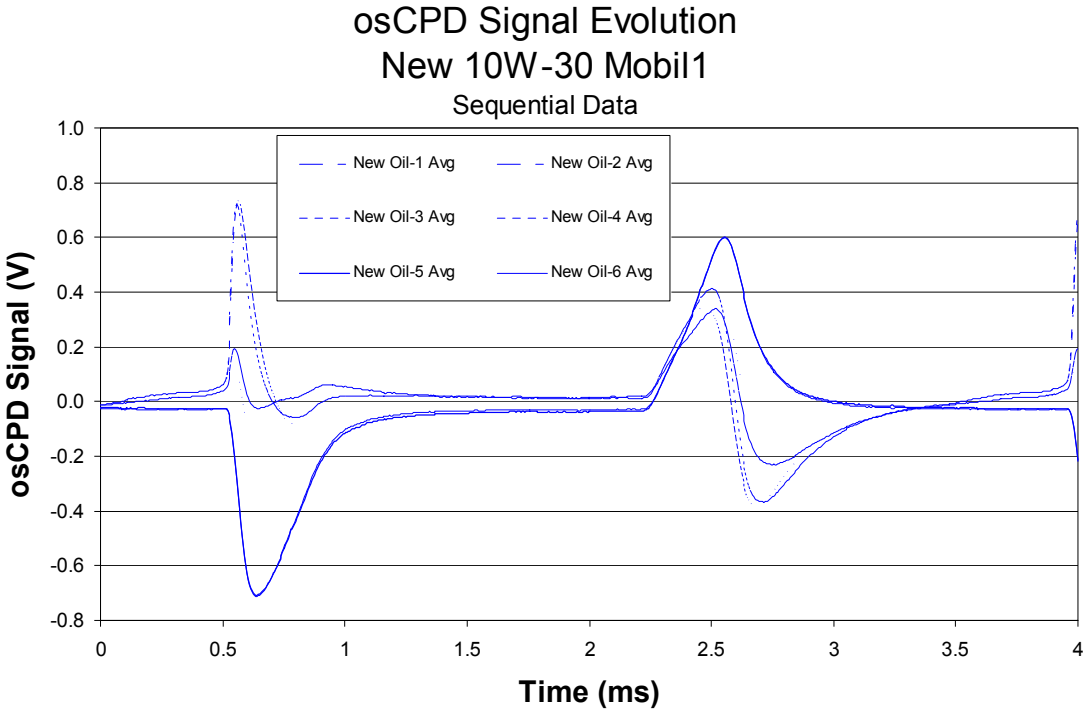

Figure 5-11: osCPD signal evolution after HF etch and exposure to oil

Thermal Aging: Sequential Experimental Order

An experiment was conducted to validate the predictive response model of the osCPD sensor. In this experiment, 10W30 Mobil1 was thermally aged at 210C, and oil samples were drawn at 30 minute intervals. After aging, 38μm precision glass spacer beads were mixed with the oil in new pre-marked vials for each thermally aged oil sample. Major test parameters are listed in Table 5-6.

Table 5-6: Experimental parameters for Mobil1 thermal aging - sequential

Equipment/ Parameter	*Description / Settings and comments*
Oil Sample	10W30 Mobil1; thermally aged @ 210C on digital hotplate
Glass Spacers	38μm
CPD Probe	Custom-built as described in Chapter 3
Light Source	Source 600 nm, +/- 20nm; 1.67mW intensity
Optical Chopper Settings	7-blade chopper; 290 Hz chopping frequency
Voltage Bias	None / grounded

A single (111) p-type silicon substrate and matching mica spacer was used throughout this set of experiments. This set of experiments was conducted immediately following the prior investigation of the effect of oil on osCPD waveform evolution, and used the identical silicon substrate. The silicon substrate and mica were soaked in an agitated petroleum ether bath for several minutes to remove the prior oil sample. Care was taken to maintain the vertical orientation of the silicon substrate (so that only the top surface was exposed to oil samples).

The oil samples were measured sequentially, in order of increasing equivalent thermal age: The new oil was measured first, followed by oil samples in order of increasing equivalent thermal age. The oil sample was loaded into the silicon-mica stack, and placed on the test fixture. After a measurement was made, the sample stack was removed from and returned to the test fixture for a repeat measurement. This was repeated six times per sample. The average waveform for the six measurements of the first new oil sample is shown in Figure 5-11 as the data series "New Oil-5 Avg." This is the identical waveform that is shown in Figure 5-11 (these experiments were preformed in immediate succession).

The silicon substrate and spacer were then washed and re-loaded with the second new oil sample, and six measurements were taken as described above. The average waveform for these six individual measurements is shown in Figure 5-12 as the data series "New Oil-6 Avg." Again, this is the identical waveform that is shown in Figure 5-10. The process of removal, cleaning, and reloading was then repeated for the 512-hour and 1024-hour equivalent aging samples as indicated by the series "512 Hr-1 Avg," "512 Hr-2 Avg," "1024 Hr-1 Avg," and "1024 Hr-2 Avg," The peak-to-peak voltage of the CPD signal, V_{PP}, was calculated from the scanned waveform data, and is presented in Figure 5-13.

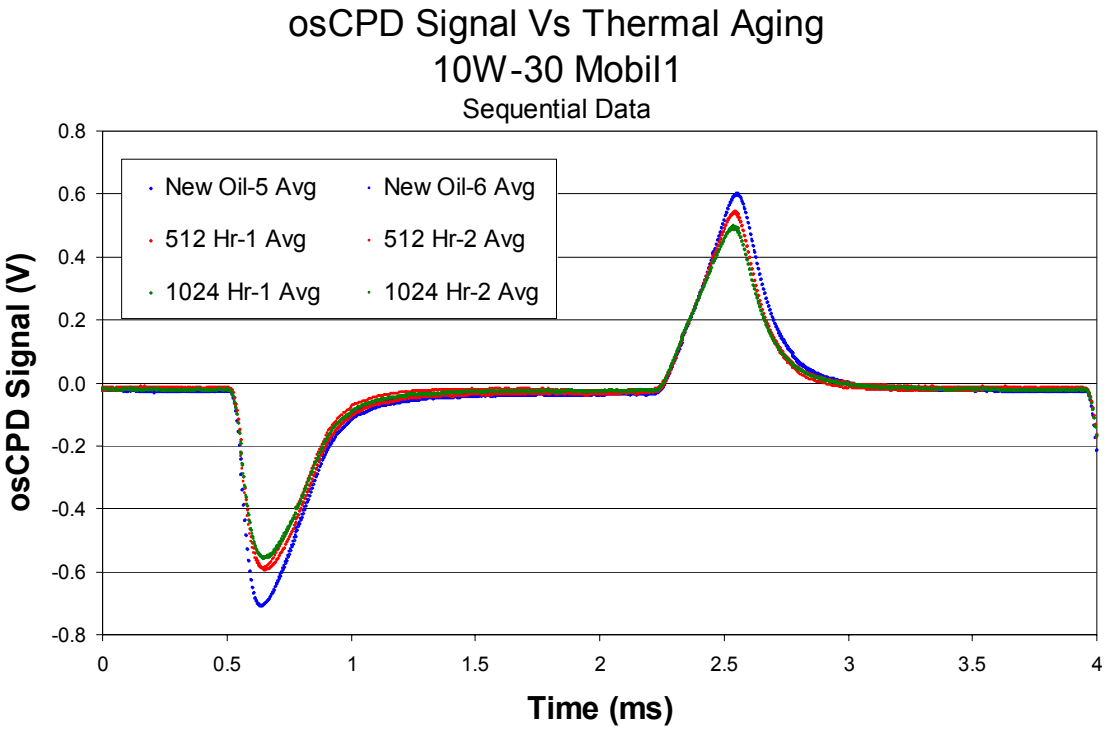

Figure 5-12: Scanned waveform from Mobil1 thermal aging - sequential

As seen in Figure 5-12, the osCPD waveform exhibits the typical two-peak pattern, with the negative peak corresponding to the light turning "on", and the positive peak corresponding to the light turning "off." The data shows excellent repeatability between measurements of a given oil sample with the average waveforms for the New and 1024-hour samples being nearly indistinguishable. A slight variation between samples in the 512-hour waveforms can just be seen in the negative peak.

Several key differences between the waveforms in Figure 5-12 and Figure 5-2 can be observed. These differences are related to the differences in experimental parameters. The waveforms in Figure 5-12 can be seen to be significantly larger in magnitude. The waveforms also exhibit faster rise times and longer settled periods between peaks. These differences are due to the combined effects of the improved CPD probe used in the

current experiments, the more powerful light source, and the use of a 7-bladed optical chopper rather than the 10-bladed chopper used in the initial experiments. The present experiments were conducted at a chopping frequency of 290Hz as compared to 400Hz in the initial experiments. The reduced number of blades results in an slightly increased rotational velocity of the chopper blades in the current experiment, and thus a larger signal amplitude. Additionally, the increased width of the chopper blades relative to the light aperture served to allow longer signal settling periods between peaks.

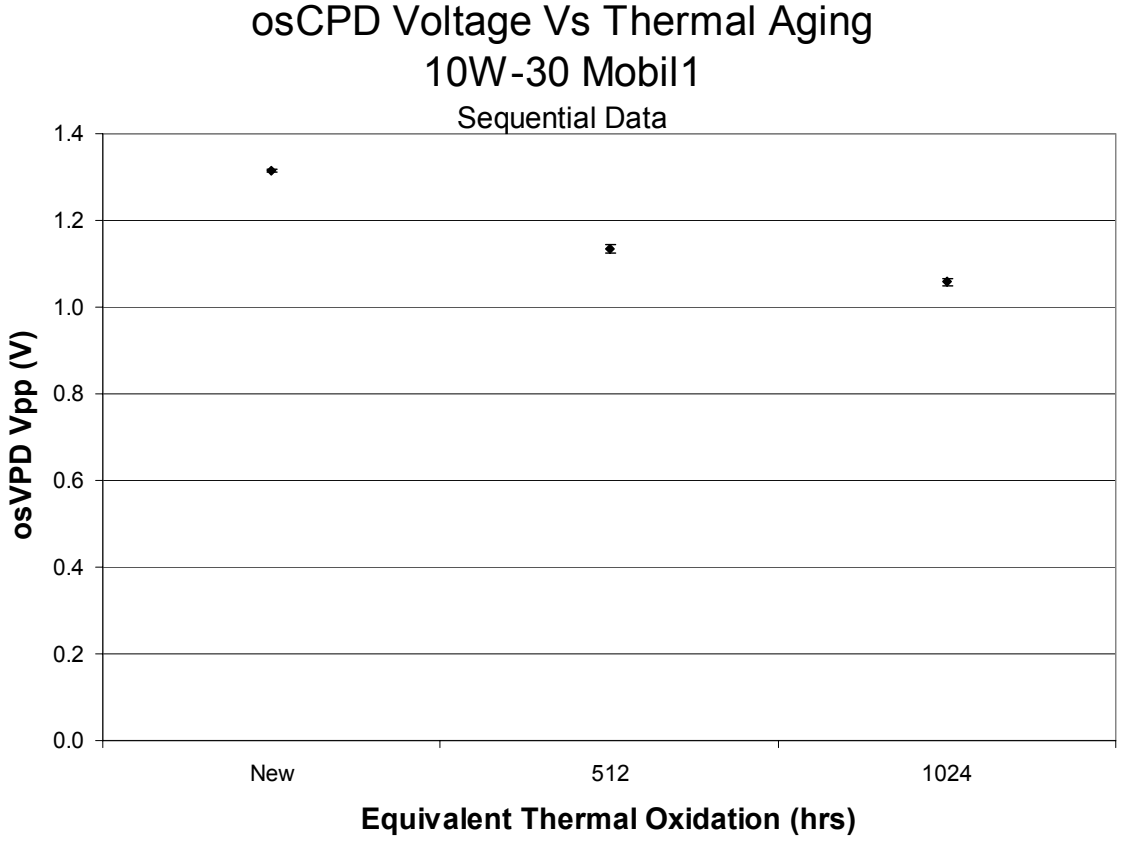

Figure 5-13: Peak-to-peak voltage data from Mobil1 thermal aging - sequential

Thermal Aging: Round-Robin Experimental Order

A second set of experiments to measure the thermally aged 10W30 Mobil1 was conducted in an effort to repeat the results obtained previously. The intention was to verify that the signal was due to the thermal aging of the oil sample, and to determine the contribution of experimental factors to measurement variability. Given that the prior experiments were conducted in order of thermal aging, there was concern that the trend in the data may be an artifact due to a change in the silicon substrate over the course of the experiments, rather than being due to differences in the oil samples. The oil samples prepared for the prior experiment were used again in the present experiment. Major test parameters are listed in Table 5-7.

Table 5-7: Experimental parameters for Mobil1 thermal aging – round-robin

Equipment/ Parameter	*Description / Settings and comments*
Oil Sample	10W30 Mobil1; thermally aged @ 210C on digital hotplate
Glass Spacers	38μm
CPD Probe	Custom-built as described in Chapter 3
Light Source	Source 600 nm, +/- 20nm; 1.67mW intensity
Optical Chopper Settings	7-blade chopper; 290 Hz chopping frequency
Voltage Bias	None / grounded

Six individual (111) p-type silicon substrates and matching mica spacers were used in conducting the individual sets of experiments. The silicon substrates and mica were soaked in an agitated petroleum ether bath for several minutes to remove the prior oil sample. Individual silicon-mica pairs were maintained, and care was taken to maintain the vertical orientation of the silicon substrate (so that only the top surface was exposed

to oil samples). The oil samples were measured in round-robin order in three rounds of measurements. The six substrates were loaded in pairs of two with the new oil, 512-hour oil, and 1024-hour oil, respectively. Each sample stack was placed on the test fixture, and a single measurement was made. After each sample stack was measured, the silicon-mica pairs were disassembled and cleaned. In the second round of measurements, the six substrates were loaded in groups of two with the 512-hour oil, 1024-hour oil, and new oil respectively. After measurement and cleaning, the oil samples were rotated one final time with respect to the silicon-mica pairs. This scheme is indicated in Table 5-8

Table 5-8: Round robin experimental sequence for thermal aging

Measurement Round	***Substrates 1 & 2***	***Substrates 3 & 4***	***Substrates 5 & 6***
1	New Oil	512-Hour	1024-Hour
2	512-Hour	1024-Hour	New Oil
3	1024-Hour	New Oil	512-Hour

As seen in Figure 5-15, the peak-to-peak voltage data from the round-robin experiments compares very favorably with the data from the sequential experiment shown in Figure 5-13. The average values are nearly identical. This would suggest that the mechanism of signal generation is due to adsorption as opposed to a chemical reaction at the surface of the SiO_2. If there had been substantial chemical reaction involved, one might expect the average peak-to-peak voltages for the different samples to collapse towards some common value. The standard deviation for each sample is substantially larger in the round-robin data than in the sequential data. This is likely due to incomplete cleaning of silicon substrates between samples.

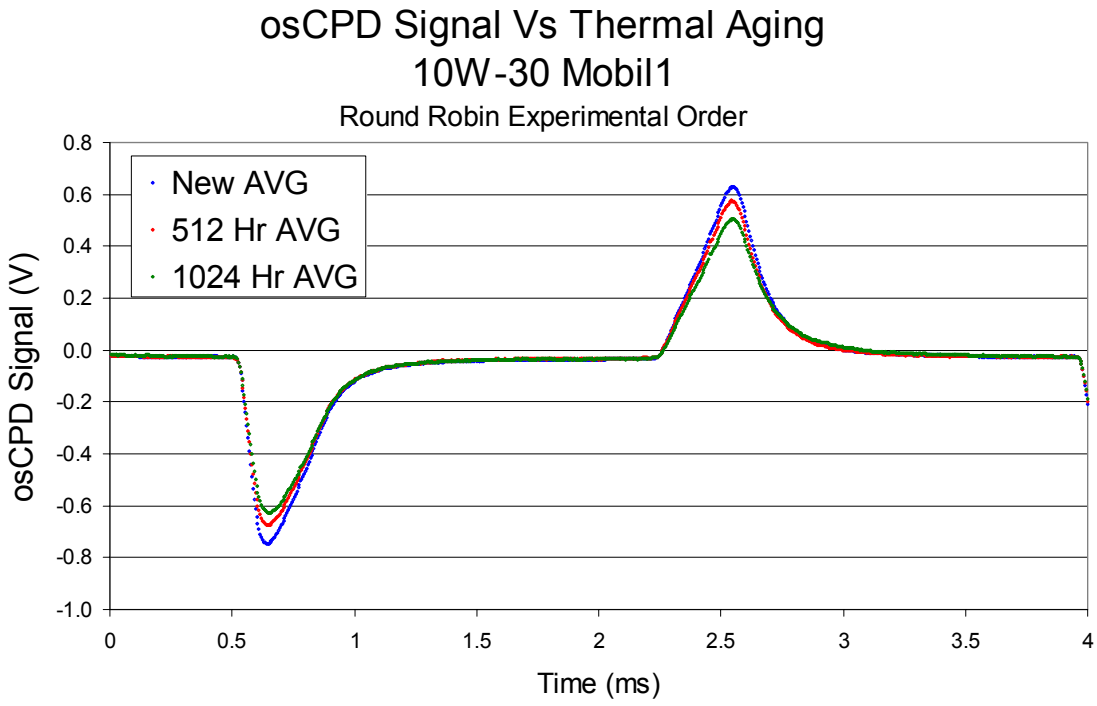

Figure 5-14: Scanned waveform from Mobil1 thermal aging – round-robin

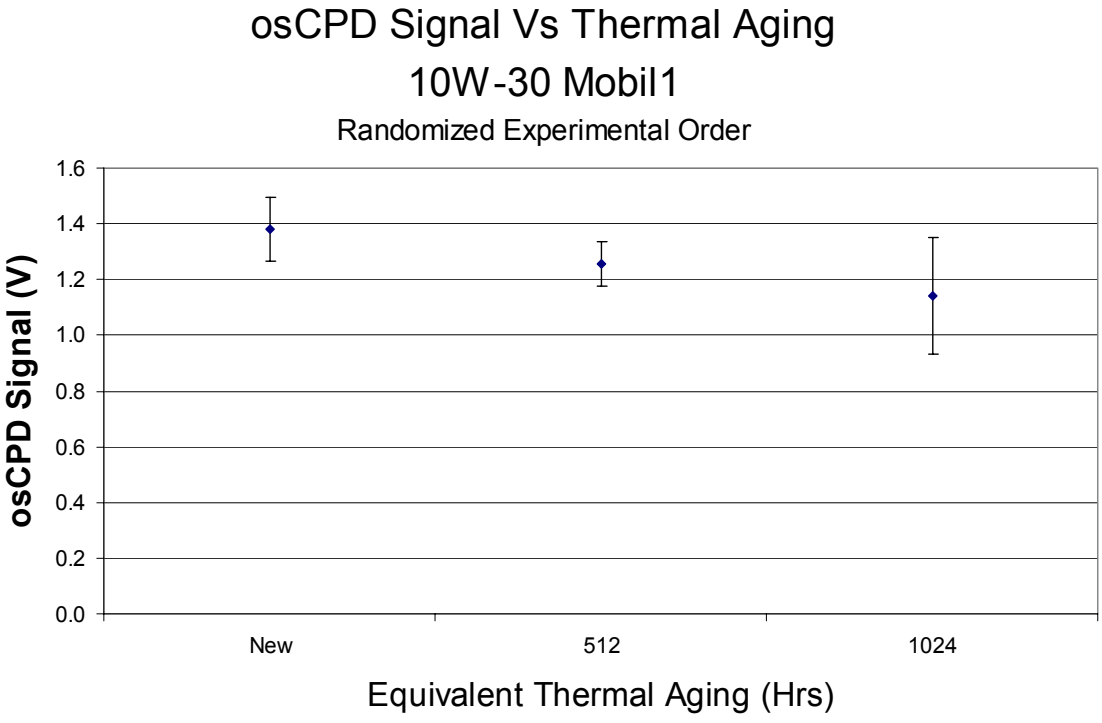

Figure 5-15: Peak-to-peak voltage data from Mobil1 thermal aging – round-robin

DC Voltage Bias Experiments

An experiment was conducted in which a DC bias voltage was applied to the back surface of the silicon substrate via the copper grounding strip. The intention of the experiment was to determine whether the osCPD sensor would respond analogously to sensors based on a MOSFET architecture. The power supply to the CPD probe and the bias voltage supply shared a common ground so that the full applied potential existed between the CPD probe tip and the back surface of the silicon substrate. A standard sample assembly containing new 10W30 Mobil1 and 35mm glass spacer beads was placed on the test fixture, and measurements were taken in the presence of an applied bias. It should be noted that the potential drop, therefore, is expected to occur across the mica, oil, and SiO_2 layers which lie between the top surface of the silicon and the probe tip. This means that there is not a significant field present in the body of the silicon itself.

Table 5-9: Experimental parameters for DC Bias experiment

Equipment/ Parameter	*Description / Settings and comments*
Oil Sample	New 10W30 Mobil1
Glass Spacers	38μm
CPD Probe	Custom-built as described in Chapter 3
Light Source	Source 600 nm, +/- 20nm; 1.67mW intensity
Optical Chopper Settings	7-blade chopper; 290 Hz chopping frequency
Voltage Bias	+ / - 350V DC

As shown in Figure 5-16, a first set of measurements was conducted with a supply capable of applying +/- 50V DC as indicated by the blue diamond-shaped data markers. A more substantial power supply was used for a second set of measurements in which the

bias voltage was varied between 0V and -350V in 50V increments, and then reduced back to 0 in 50V increments. The measurements taken in this way were repeatable, and showed no indications of hysteresis. The power supply was then set to +350V. The second set of measurements showed the same trend as the first set of measurements in that the application of a substantial voltage bias did not significantly influence the osCPD signal. The waveforms exhibited in all of the measurements were typical with respect to osCPD measurements, and showed no signs of distortion over the range of voltages tested.

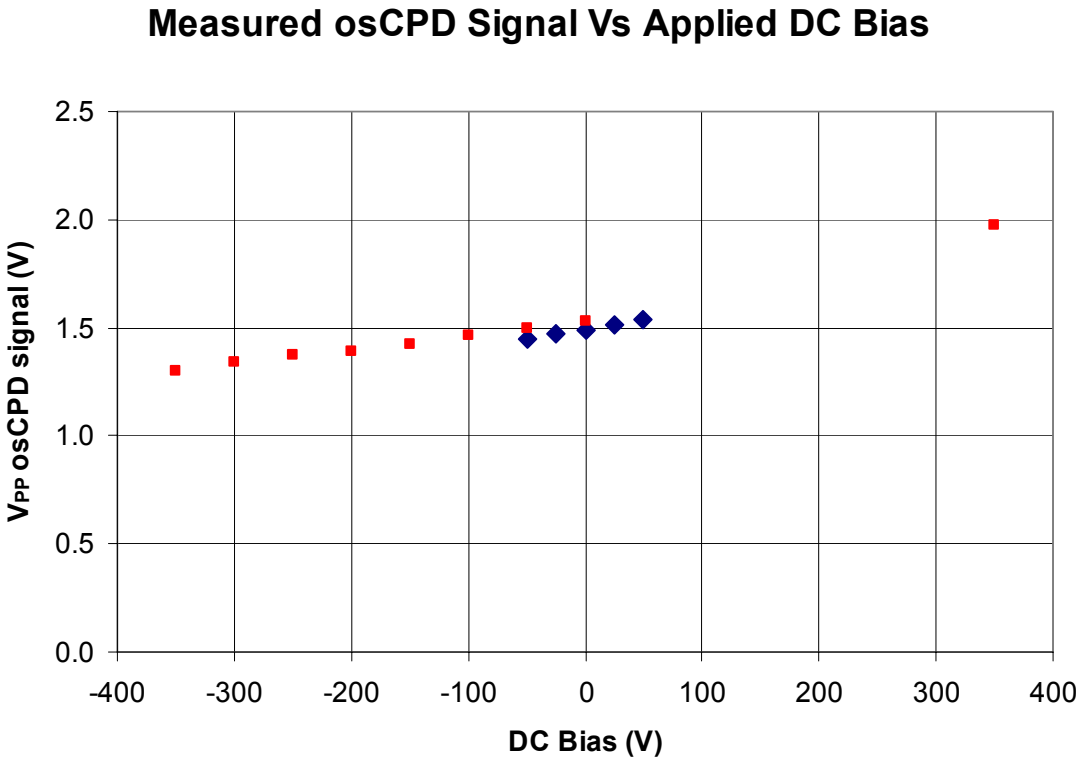

Figure 5-16: DC Bias voltage experimental data

Due to the small influence of the applied bias voltage, it can be inferred that the osCPD signal must be generated at the top surface of the silicon substrate.

Experimental Summary

This chapter presented and reviewed a series of experiments that were performed to establish the mechanism of signal generation in the osCPD sensor. A summary of the experiments and the primary outcomes is listed in Table 5-10. The signal was shown to be due to a surface charge interaction occurring at the top surface of the silicon substrate. osCPD measurements of thermally aged engine oil correlate with physical measurements made on the oil samples using spectroscopy. The signal response was shown to increase in amplitude with optical chopping frequency and incident light intensity. The presence of the osCPD waveform in the absence of an oil sample indicates that the signal occurs at the silicon substrate surface, not in the bulk of an oil sample. The lack of differentiation between oil samples on a non-etched silicon substrate suggests dependence on a surface charge interaction between the oil sample and the silicon substrate, and not changes in the dielectric properties of the oil sample. Finally, the probe response is shown to have excellent measurement resolution within an experiment and good repeatability between experiments. With respect to the final two sets of experiments conducted on the thermally aged 10W30 Mobil1, the osCPD sensor exhibited a signal-to-noise ratio, or *SNR*, of 42dB where the signal-to-noise ratio is calculated as

$$SNR = 20 \cdot \log 10\left(\frac{V_{pp}}{V_{noise}}\right) \tag{5.1}$$

Here, V_{noise} is defined by the peak-to-peak voltage measured during steady-state probe response (when the signal should be constant). It should be noted that the noise to first order does not appear to scale with light intensity, so that higher values of SNR may be achievable with a higher intensity light source. It should also be noted that the noise level cited corresponds to the *averaged* osCPD signal, as described in Chapter 4.

Table 5-10: Summary of experiments

Experiment	***Description***	***Principle Outcomes***
Thermal Aging POC	Proof of concept, Pennzoil 10W30 aged at 160C	osCPD sensitive to thermal aging
Spectroscopy of Aged Oil	Visible absorption using improvised test fixture	Good correlation with osCPD measurements
Chopping Freq.	60Hz Noise sensitivity assay	No 60Hz noise detected
Light Intensity	osCPD sensor response evaluated Vs light intensity and optical chopping freq.	signal is proportional to light intensity and is proportional to chopping frequency
Non-etched Si Substrate	Thermal aging experiments repeated with un-etched Si	osCPD waveform similar to prior experiments, but no differentiation between samples
HF Etch then Surface Charge Evolution in Air	Silicon substrate monitored immediately after HF-etch.	osCPD signal generated at Si-SiO_2 interface; correlation with trapped charge evolution.
Thermal Aging & Variable Oil Film Thickness	Pennzoil 10W30 aged at 160C and mixed with glass spacers of varying diameter	osCPD signal and trend repeatable. Signal is from silicon substrate surface
HF Etch then Surface Charge Evolution with Oil	Oil placed on silicon substrate and monitored immediately after HF-etch.	More rapid stabilization of signal with repeated cleaning cycles.
Thermal Aging: Sequential	10W30 Mobil1 aged at 210C, 35μm spacer beads. Measurements made sequentially starting with respect to thermal aging	Measurements are very repeatable and strongly correlated with thermal aging. Good correlation with FTIR and visible spectroscopy
Thermal Aging: Randomized	10W30 Mobil1 aged at 210C, 35μm spacer beads. Random measurements order with respect to oil thermal aging.	Signal trend and magnitude repeatable, variability influenced by randomized order. Signal is reversible: adsorption dominates
Voltage Bias	Si Substrate Biased +/-350V	Negligible influence on signal
Ferric Chloride (See Appendix I)	Base stock mixed with oil soluble ferric chloride to obtain 1000ppm sample	Strong sample differentiation; hysteresis suggests chemical reaction at SiO_2 surface then reversible adsorption

CHAPTER 6

ANALYSIS

The previous chapter presented the results obtained from measurements made on oil samples using the osCPD sensor. The sensor showed repeatable response to measurements of oil samples that were thermally degraded under laboratory conditions, as well as to samples obtained from actual degradation in an automobile engine. The osCPD data also shows good correlation with spectroscopic measurements of the oil samples. This chapter will begin by developing predictive models that relate the properties of the fluid under investigation, in this case thermally aged oil, to the osCPD sensor response signal. Subsequent sections will present comparisons of the modeling results and the experimental data. The chapter will conclude with extension of the osCPD models and data to predictions regarding certain physical properties of the oil sample after thermal degradation.

The osCPD Sensor: Mechanisms of Signal Generation

The process of osCPD signal generation can roughly be broken into four primary stages with each stage's behavior predicted by an underlying fundamental mechanism. The four components (or stages) of osCPD signal generation are photon absorption and photo-generation, minority carrier diffusion and the formation of a space charge region, adsorbed dipole layer interaction with the space charge region, and CPD probe response. The sections that follow develop the fundamental models that were used to predict the osCPD sensor response as well as analyze and interpret the experimental results. Many of these models are based on silicon device physics or have been presented in previous sections; detailed derivations are therefore not provided.

Photon Absorption and Photogeneration

Light incident on silicon is absorbed if the photon energy (hν) is greater than the band gap energy of silicon (1.12eV). The distance that a photon travels into silicon before being absorbed is wavelength dependent and is related to incident intensity by[40]

$$I = I_o e^{-\alpha x} \tag{6.1}$$

Where

I_o is the intensity of the light just inside the silicon surface

α is the wavelength-dependent absorption coefficient (a material property)

x is the depth of penetration into the silicon

The percentage of photons reflected, R_n, at normal incidence to the silicon surface is[41]

$$R_n = \frac{\left(n^* - 1\right)^2 + k^{*2}}{\left(n^* + 1\right)^2 + k^{*2}} \tag{6.2}$$

Here, n^* and k^* are the real and imaginary components of the refractive index. Table 6-1 contains the range of visible wavelengths that were used in conducting the experiments, as well as the associated absorption and reflection coefficients. The table also contains a characteristic absorption length, L, which is arbitrarily calculated for 95% absorption of incident light.

Table 6-1: Typical values for incident light used in osCPD sensor

λ (nm)	E (eV)	n*	k*	R_n	α (1/cm)	L (μm)
750	1.56	3.6	0.00	32%	1000	30
700	1.67	3.7	0.04	33%	2000	15
650	1.80	3.8	0.08	34%	3000	10
600	1.95	3.9	0.12	35%	5000	6
550	2.13	4.0	0.16	36%	7000	5
500	2.34	4.1	0.20	37%	10000	3
450	2.60	4.3	0.24	39%	30000	1
400	2.93	4.5	0.28	41%	100000	0.3

As illustrated in Figure 6-1, the back surface of the silicon substrate is illuminated and the dielectric specimen (oil) sits on the front surface. The typical silicon substrate used in the osCPD sensor was approximately 600μm thick; the number of photons reaching the top surface of the silicon substrate is inconsequential. This eliminates photon interaction with the dielectric fluid under investigation as a mechanism for signal generation.

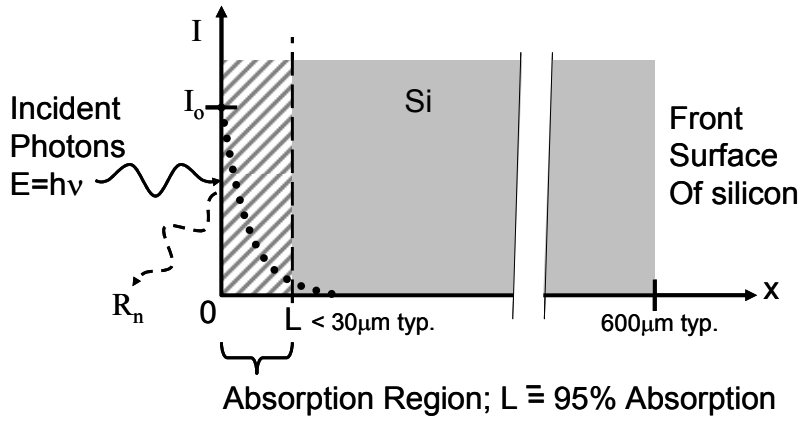

Figure 6-1: Schematic illustration of photon absorption in silicon substrate

Most absorbed photons result in the one-to-one creation of an electron-hole pair, or EHP. At steady state illumination the generation rate, $G_{L,}$ can be written as[41]

$$G_L(x,\lambda) = (1 - R_n) N_p \alpha \cdot e^{-\alpha x} \tag{6.3}$$

Where

N_p is the incident photon flux, and

R_n is the percentage of photons that are reflected, as above

Electron-hole pair generation is a symmetric process so that an identical number of electrons and holes are created:

$$\Delta n = \Delta p \tag{6.4}$$

The difference in carrier concentrations, Δn for electrons and Δp for holes, is given with respect to the equilibrium state before the light was turned on (flat-band condition). In p-type silicon since there is an abundance of holes (acceptors) prior to illumination, the additional holes generated by photon absorption are relatively insignificant. As the minority carrier in p-type silicon, the number of electrons can be increased by several orders of magnitude.

Low-intensity illumination is also referred to as low-level photon injection. Assuming low-level injection of photons into p-type silicon, the number of holes, p, and electrons, n, due to photo-generation can be approximated by[40]:

$$p = p_o + \Delta p \cong p_o \tag{6.5a}$$

$$n = n_o + \Delta n \cong \Delta n \tag{6.5b}$$

Where

$\mathbf{p_o}$ is the equilibrium condition concentration of holes

$\mathbf{n_o}$ is the equilibrium condition concentration of electrons

Therefore, in p-type silicon low-level injection implies that

$$\Delta n << p_o . \tag{6.6}$$

The light intensity in the osCPD test system is modulated by the chopper blades between full intensity, I_o, and nearly zero intensity. As illustrated in Figure 6-2, the light intensity as a function of time can be shown to be a series of piecewise continuous functions of the form

$I(t) = 0$ when the chopper blade blocks the aperture (6.7a)

$I(t) = I_o \cdot A(t)$ as the blade uncovers the aperture (6.7b)

$I(t) = I_o$ when the aperture is fully exposed (6.7c)

$I(t) = I_o \cdot \left[1 - A(t)\right]$ as the next blade moves back over the aperture (6.7d)

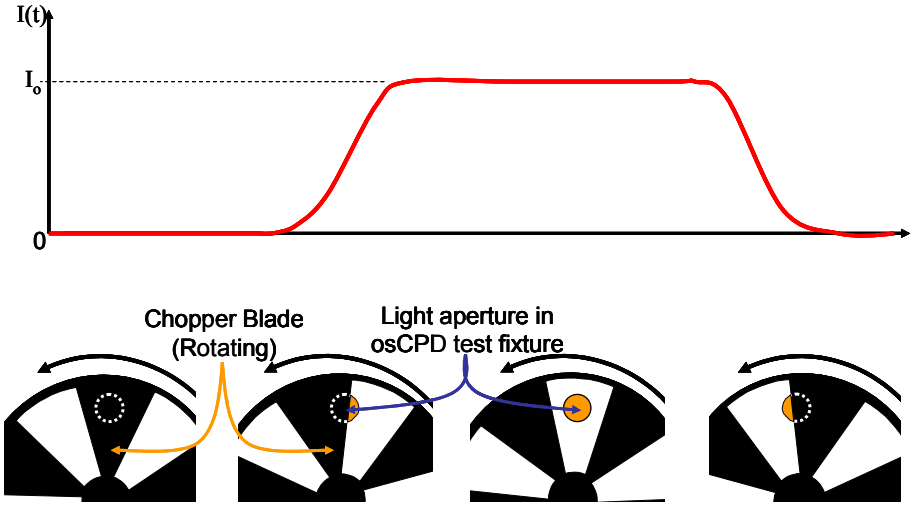

Figure 6-2: Schematic of light intensity modulation by chopper blade

As a result, the generation rate, G_L, and the change in minority carrier concentration, Δn, are expected to be functions of time of similar form and proportional to Equations 6.7.

Minority Carrier Diffusion and Space Charge Region Formation

As schematically illustrated in Figure 6-3, the relatively high concentration of electrons in the photon absorption layer at the illuminated surface leads to electron diffusion into the silicon substrate according to[42]:

$$J_{N-diff} = -qD_N \nabla n \tag{6.8}$$

Where

$J_{N\text{-}diff}$ is defined as the electron diffusion current

D_N is the diffusion coefficient for electrons

q is the fundamental charge of an electron

∇ **n** is the gradient of volume density of electrons

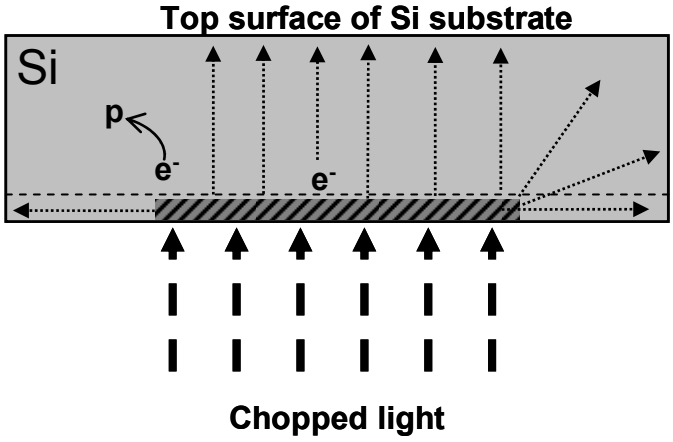

Figure 6-3: Schematic illustration of diffusion of minority carriers

The diffusion coefficient is related to the carrier mobility of the substrate by the Einstein Relationship. For electrons this is given as[42]

$$\frac{D_N}{\mu_n} = \frac{kT}{q} \tag{6.9}$$

where

D_N is the diffusion coefficient for electrons

μ_n is the electron mobility

k = 1.38 x 10-23 J/K is the Boltzmann constant

T is the temperature in degrees Kelvin, and

q = 1.60 x 10-19C is the fundamental charge of an electron.

While EHPs are created by generation, recombination is a process whereby EHPs are annihilated. Recombination can occur by a variety of processes including band-to-band recombination, Auger recombination and R-G center recombination[41]. These processes are the mechanisms by which the excess carriers (electrons and holes) generated by some external perturbation (in this case, light) return to the equilibrium levels. Recombination of the electron-hole pairs (mutual annihilation of excess electrons and holes) is occurring in parallel with generation according to[40]

$$\left.\frac{\partial n}{\partial t}\right|_{\substack{i-thermal \\ R-G}} = -\frac{\Delta n}{\tau_n} \tag{6.10}$$

Here, the average lifetime, τ_n, of an electron in p-type silicon can be calculated as[42]

$$\tau_n = \frac{1}{c_n N_T} \tag{6.11}$$

where

$\mathbf{c_n}$ is the electron capture coefficient

$\mathbf{N_T}$ is the volume density of R-G centers (number/ cm^3)

The diffusion of excess electrons in p-type silicon is given by[40]

$$\frac{\partial \Delta n_p}{\partial t} = D_N \frac{\partial^2 \Delta n_p}{\partial x^2} - \frac{\Delta n_p}{\tau_n} + G_L \tag{6.12}$$

At steady state illumination,

$$\frac{\partial \Delta n_p}{\partial t} = 0 \tag{6.13}$$

By substituting Equation 6.13 into Equation 6.12, at steady state illumination

$$\frac{\Delta n_p}{\tau_n} = G_L \tag{6.14}$$

Continuity of charge carriers requires that[40]

$$\frac{\partial n}{\partial t} = \frac{1}{q} \nabla \cdot J_N + \left.\frac{\partial n}{\partial t}\right|_{\substack{thermal \\ R-G}} + \left.\frac{\partial n}{\partial t}\right|_{Other}. \tag{6.15}$$

Where J_N is the total electron current given by[42]

$$J_N = J_{N-drift} + J_{N-diff}. \tag{6.16}$$

$J_{N\text{-}drift}$, the electron current due to electric field is[42]

$$J_{N-drift} = q\mu_n n\varepsilon \tag{6.17}$$

where ε is the electric field in the silicon. In the case of the osCPD sensor, there is typically no voltage bias applied to the silicon substrate and therefore no electric field so that drift current in the osCPD sensor is negligible. The total electron current, J_N, reduces

to $J_{N\text{-}diff}$ as given in Equation 6.8. Also, assuming that there are no other processes by which carriers are injected or removed from the system,

$$\left.\frac{\partial n}{\partial t}\right|_{Other} = G_L \tag{6.18}$$

By substitution of Equations 6.8 and 6.18 into 6.15, the continuity equation can be written as

$$\frac{\partial n}{\partial t} = -\nabla \cdot D_N \nabla n - \frac{\Delta n_p}{\tau_n} + G_L \tag{6.19}$$

The time rate of change of electrons in the silicon substrate is a function of the generation, diffusion, and recombination of electrons (and their associated holes). As shown in Figure 6-4, the test fixture and probe tip used in the osCPD sensor were constructed in such a way that the probe tip is centered on the light aperture in the test stand. Furthermore, the diameter of the probe tip is significantly smaller than that of the aperture, and the silicon substrate is relatively thin compared to the diameter of the probe tip and light aperture. It is therefore reasonable to envision diffusion of electrons as a planar front, and to treat the system as one-dimensional for purposes of analysis.

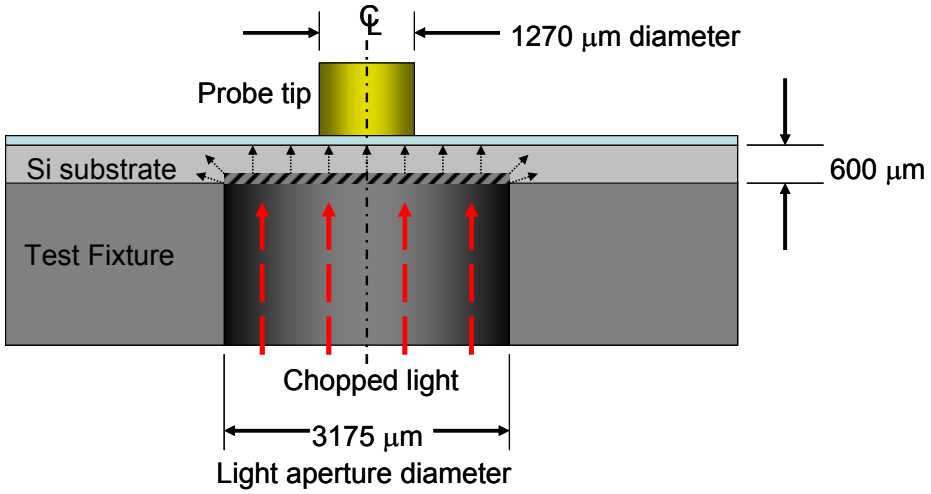

Figure 6-4: Schematic diagram of light aperture and probe tip geometry

Given an initial concentration of excess carriers, n_o, an incident photon flux, N_p, and assuming one-dimensional analysis an infinitely thick body of silicon, electron density as a function of depth into the silicon, x, and time, t, can be calculated as[42]

$$n(x,t) = \frac{N_p}{\sqrt{4\pi D_N t}} \exp\left(-\frac{x^2}{4D_N t} - \frac{t}{\tau_n} \right) + n_o \tag{6.20}$$

The Fermi energy in the bulk of a semiconductor is related to the doping of the semiconductor. Under equilibrium conditions, the number of carriers is related to the Fermi level by[40]

$$n_o = n_i e^{(E_F - E_i)/kT} \tag{6.21a}$$

$$p_o = n_i e^{(E_i - E_F)/kT} \tag{6.21b}$$

where E_i is the Fermi level of intrinsic (undoped) silicon. In the bulk of the silicon substrate, the potential due to doping is given as[40]

$$\phi_F = \frac{1}{q}\left[E_{i(bulk)} - E_F \right] \tag{6.22}$$

In the absence of a space charge region and without external perturbation (i.e. when there is no incident light) the surface potential is equal to the bulk potential:

$$\phi_s = \phi_F \tag{6.23}$$

However, due to the injection of minority carriers by diffusion resulting from photo illumination, a space charge region (SCR) is induced at the top surface of the silicon substrate. The distribution of carriers in the space charge region is different from the

concentration of carriers in the bulk of the silicon. This leads to localized shifts in the energy band structure (band bending). A localized Fermi level (or quasi-Fermi level) associated with the band bending is created. The quasi-Fermi level is related to the carrier concentrations in the space charge region. For electrons, this can be calculated by rearranging Equation 6.21a as

$$E_{i(surface)} = F_N = E_i + kT \ln\left(\frac{n_{surface}}{n_i}\right) \tag{6.24}$$

Here, the electron density at the surface, $n_{surface}$, can be determined by solution of Equation 6.20 as a function of incident light intensity. Finally, the surface potential due to localized band bending caused by carrier injection from illumination can be expressed as

$$\phi_s = \frac{1}{q}\left[E_{i(bulk)} - F_N\right] \tag{6.25}$$

Thus, the surface potential of the front surface of the silicon substrate is related to the carrier density in the immediate vicinity of the silicon surface. As light intensity is modulated on the back surface of the silicon substrate, electron diffusion leads to a time-varying concentration of carriers, and the creation of a time-varying space charge region at the front surface of the substrate. As a result, the surface potential is modulated between the bulk potential, ϕ_F, and the surface potential, ϕ_s, given by Equation 6.26. The modulation of surface potential by the chopped light is the fundamental mechanism by which the CPD signal is created. As will be discussed in detail in subsequent sections, the induced current in the CPD probe tip is proportional to the time rate of change of the suface potential of the silicon substrate:

$$i_{CPD}(t) \propto \frac{\partial \phi_s(t)}{\partial t}. \tag{6.26}$$

Trapped Charge at the Si-SiO_2 Interface

As discussed in Chapter 2, a static space charge region can be formed by the presence of a charge layer at the Si-SiO_2 interface[33]. Trapped charges are created in the oxide of the silicon substrate by the HF etch surface preparation of the silicon substrate[43]. After etching, the substrate is allowed to oxidize at room temperature (300K). Oxidation at low temperature leads to the introduction of ionized silicon into the oxide layer near the silicon surface[40]. As shown in Figure 6-5, trapped surface-state charges on the order of $10^{10} - 10^{12}/cm^2$ are typical[43]. Since the silicon substrates used in the osCPD sensor were allowed to oxidize at room temperature (300K), initial post-oxidation surface charge in excess of $10^{12}/cm^2$ would be expected.

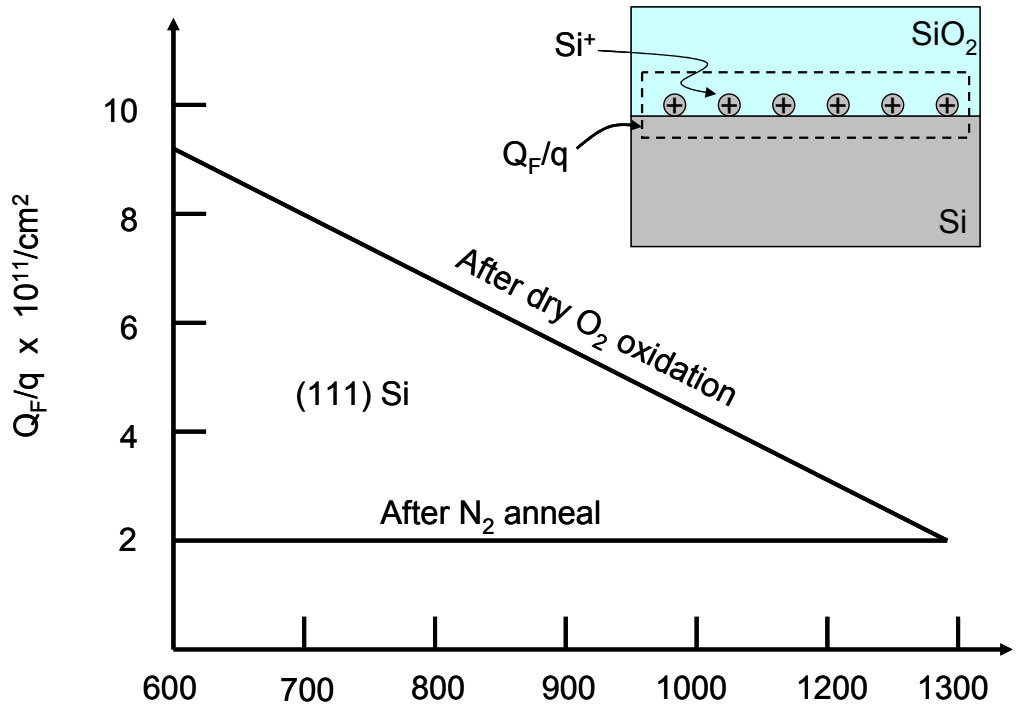

Figure 6-5: Trapped charge at Si-SiO_2 interface after oxidation (adapted from Deal[43])

As schematically illustrated in Figure 6-6 for p-type silicon, the presence of trapped charges at the Si-SiO_2 interface leads to the creation of a static depletion region and localized band bending at the silicon surface. The injection of excess carriers into the space charge region results in modulation of the quasi-Fermi level as the light intensity is modulated. As will be discussed further in the following sections, the combined effect of the static surface charge and the modulation of surface potential by the chopped light is the by which the osCPD sensor differentiates between samples.

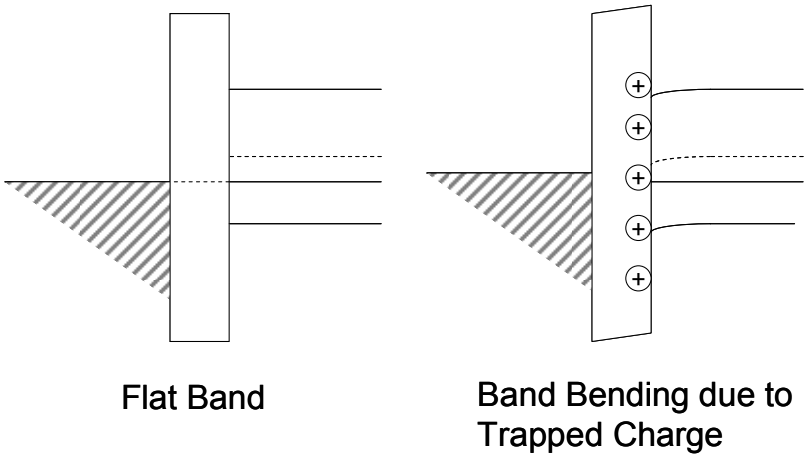

Figure 6-6: Schematic of trapped charge induced SCR

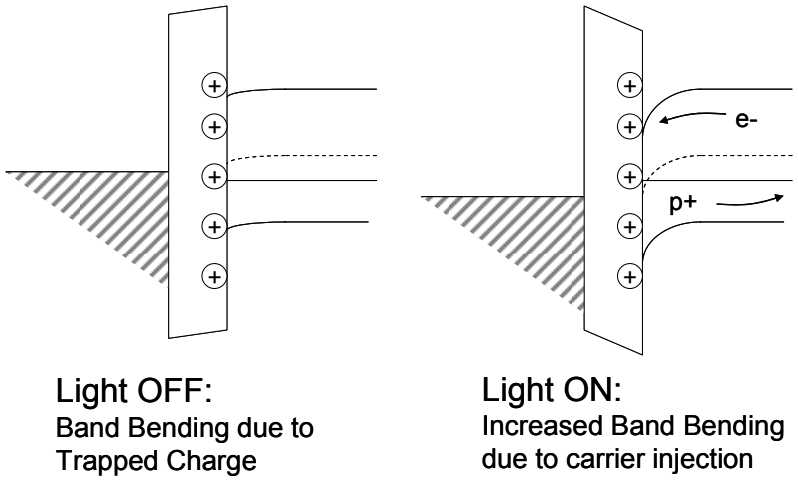

Figure 6-7: Schematic of energy bands with trapped charge and carrier injection

Adsorbed Dipole Interaction with the Space Charge Region

When oil samples are placed on the prepared silicon substrate, additives from the oil preferentially adsorb to the SiO_2 surface. The additives as well as the base oil can be visualized as long-chain molecules with polar end-groups. Molecular adsorption is known to modify the work function of a surface. As reviewed in Chapter 2, the polar end-groups dominate the adsorption process and the associated effect on the surface work function[27]. The Helmholtz equation predicts the change in work function, $\Delta\Phi$, at an interface as a function of the dipole moment and concentration of the adsorbate species as

$$\Delta\Phi = \frac{\mu_p N}{\varepsilon_0 \varepsilon_r}\theta . \tag{6.27}$$

Here,

μ_p is the perpendicular component of the dipole moment of the end-group

N is the number of adsorption sites

θ is the fractional area of coverage with respect to available adsorption sites, and

ε_r is the relative dielectric of the adsorbate.

As described in the previous section, the surface of the silicon substrate has a substantial trapped charge at the interface. Molecules with polar end-groups adsorb to the SiO_2 surface and interact with the space charge region created by the trapped charge at the Si-SiO_2 interface. The surface potential of the silicon substrate is modified by the presence of the adsorbed species according to the Helmholtz equation, Equation 6.27.

As schematically illustrated in Figure 6-8, a surface initially of potential ϕ_{s1} is affected by the presence of the adsorbed dipole layer by

$$\phi_{s2} = \phi_{s2} + \Delta\Phi \tag{6.28}$$

where $\Delta\Phi$ as defined previously is the change in work function due to adsorption. Therefore, the amplitude of surface charge modulation is a function of the concentration of adsorbed species. Since the current in the CPD probe tip varies according to

$$i_{CPD}(t) = \frac{C}{|e|}\frac{\partial\phi_s(t)}{\partial t}, \tag{6.29}$$

adsorption changes the value of the surface potential, ϕ_s, thereby modulating the amplitude of the CPD signal.

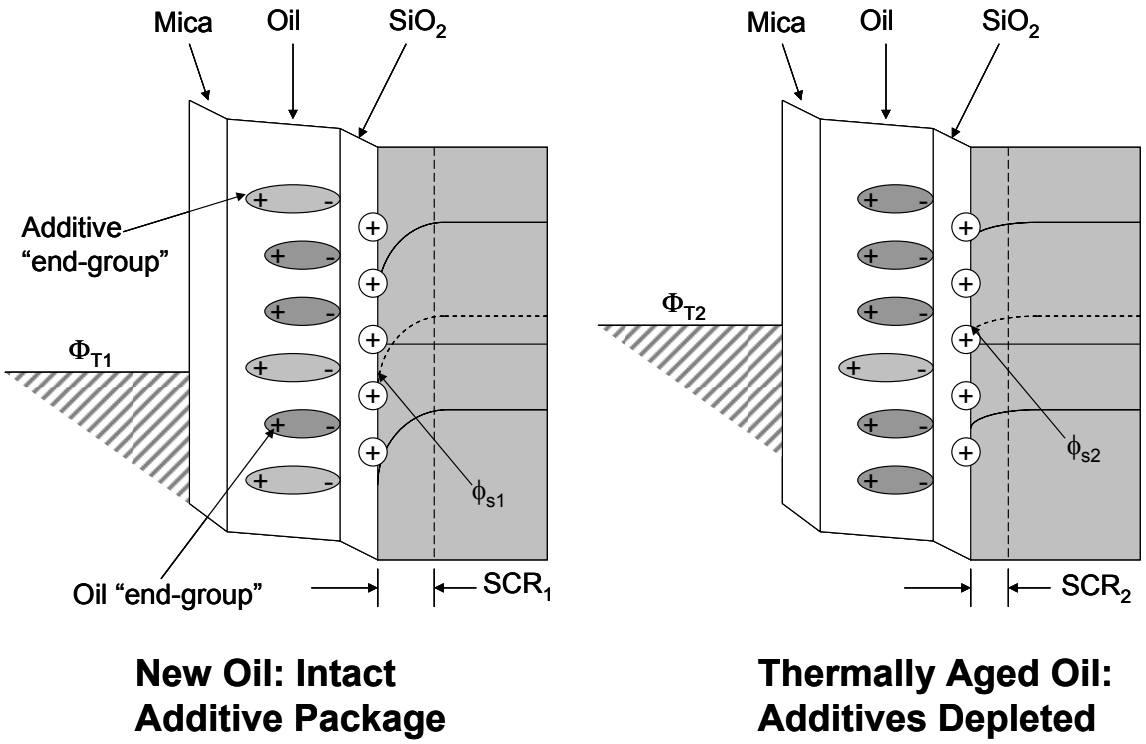

Figure 6-8: Effect of additive depletion on silicon substrate surface potential

CPD Probe Tip Response

The probe tip and the silicon substrate of the osCPD sensor effectively form an MIS-C structure with the metal gate replaced by the probe tip. As discussed previously in Chapter 2, rather than driving the surface potential of the silicon with an applied gate voltage, in the osCPD sensor, the CPD probe tip potential is driven by the surface potential of the Silicon. As illustrated in Figure 6-9, modulation of the quasi-Fermi level at the silicon surface drives the surface potential of the probe tip.

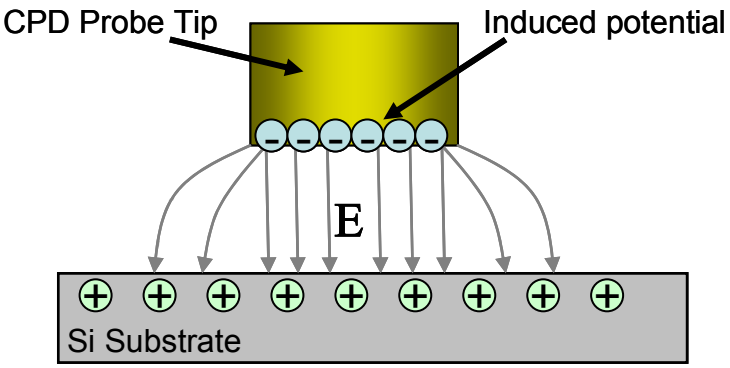

Figure 6-9: Schematic illustration of silicon surface potential driving probe tip potential

In general, the signal generated in a CPD probe is given by[19]

$$i_{CPD}(t) = C\frac{\partial V_{CPD}}{\partial t} + V_{CPD}\frac{\partial C}{\partial t} \tag{6.30}$$

Since the geometry of the osCPD sensor is fixed, the capacitance is constant with respect to time. Therefore, equation 6.30 can be reduced to

$$i_{CPD}(t) = C\frac{\partial V_{CPD}}{\partial t} \tag{6.31}$$

Taking Φ_T as the work function of the probe tip, ϕ_F as the flat band potential of the silicon substrate, and ϕ_s as the light-induced surface potential of the silicon substrate, the contact potential difference between the probe tip and the silicon surface can be expressed as

$$V_{CPD-FB} = \frac{\Phi_T - \phi_F}{|e|} \tag{6.32}$$

when the light intensity is zero, and

$$V_{CPD-ON} = \frac{\Phi_T - \phi_s}{|e|} \tag{6.33}$$

when the light is on.

As the chopper blade exposes the light aperture and the incident intensity on the back surface of the silicon substrate varies from zero to some maximum, the contact potential difference between the probe tip and the silicon substrate changes from $V_{CPD\text{-}FB}$ to $V_{CPD\text{-}ON}$, respectively. The time rate of change of the contact potential difference is dependent on the rotational speed and geometry of the optical chopper, and can be expressed as

$$\frac{\partial V_{CPD}}{\partial t} \cong \frac{\Delta V_{CPD}}{\Delta t} = \frac{V_{CPD-FB} - V_{CPD-ON}}{\Delta t} \tag{6.34}$$

Inserting Equations 6-32 and 6-33 into Equation 6-34 yields

$$\frac{\partial V_{CPD}}{\partial t} \cong \frac{1}{|e|}\left(\frac{\left(\Phi_T - \phi_F\right) - \left(\Phi_T - \phi_s\right)}{\Delta t}\right) \tag{6.35}$$

By inspection, the work function of the probe tip cancels leaving

$$\frac{\partial V_{CPD}}{\partial t} = \frac{\partial \phi_s(t)}{|e|\partial t} \cong \frac{(\phi_s - \phi_F)}{|e|\Delta t} \tag{6.36}$$

It is important to note that once again, the work function of the probe tip itself, Φ_T, does not directly contribute to the final signal. As illustrated in Figure 6-10, the capacitance between the CPD probe tip and the silicon surface is defined by the series capacitances of the mica, the oil sample, and the native oxide layer.

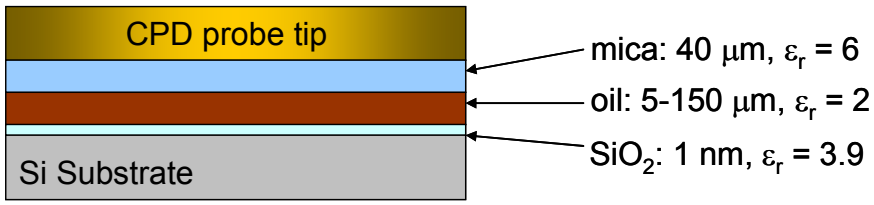

Figure 6-10: Schematic diagram of capacitive structure of osCPD sensor

The equivalent capacitance of the osCPD sensor, C_{eq}, can therefore be calculated as

$$\frac{1}{C_{eq}} = \frac{1}{C_{SiO_2}} + \frac{1}{C_{oil}} + \frac{1}{C_{mica}} \tag{6.37}$$

Calculated values for the individual layers as well as the equivalent capacitance, C_{eq}, are given in Table 6-2. These values reflect experimental conditions, and were used to predict the osCPD sensor response. It is important to note that the capacitance of the oil was explicitly assumed to be invariant between samples based on experimental results obtained using non-etched substrates as described in Chapter 5. This may not be an accurate assumption over a broader range of samples. Combining the expression for dV_{CPD}/dt from Equation 6.36 with the expression for the equivalent capacitance, C_{eq}, the induced current in the CPD probe tip can be rewritten as

$$i_{CPD}(t) = \frac{C_{eq}}{|e|}\frac{\partial \phi_s(t)}{\partial t} \quad . \tag{6.38}$$

Table 6-2: Calculated capacitance of osCPD sensor in Farads (F)

		Oil Film Thickness (spacer bead diameter)		
Layer	ε_r	**35μm**	**75μm**	**150μm**
Oil	2	2.6×10^{-12}	1.2×10^{-12}	6.0×10^{-13}
SiO_2	3.9	1.7×10^{-7}	1.7×10^{-7}	1.7×10^{-7}
Mica	6	6.7×10^{-12}	6.7×10^{-12}	6.7×10^{-12}
	$\mathbf{C_{eq}}$	5.1×10^{-13}	2.7×10^{-13}	1.4×10^{-13}

Silicon Substrate Photovoltaic Response – Computational Simulation

It has been shown that the CPD signal in the osCPD sensor is driven by the surface potential of the silicon, $\phi_s(t)$. Calculation of the surface potential requires simultaneous solution of the equations of state previously presented subject to the boundary conditions determined by the presence of the static surface charge on the top of the silicon substrate, Q_{ss}, as well as the intensity of the incident light on the back surface of the silicon substrate, $I(t)$. Similar calculations are commonly performed in solar cell device analysis using commercially available simulation software. One such simulation software package, PC1D Version 5.6, was used to calculate the energy band bending and surface potential of the silicon for given values of surface charge and light intensity.

Effect of Trapped Charge at Si-SiO_2 interface

The calculated energy bands for the silicon substrates used in the osCPD sensor as a function of measured light intensity are shown in Figure 6-11. Material properties of the silicon substrate and parameters describing the incident light and experimental conditions that were used as input to the PC1D simulation model are listed in Table 6-3.

Table 6-3: Selected input parameters used in PC1D simulation software

Input Parameter	*Value / Range*
Temperature	300K
Steady state intensity	0 to 1.67 x 10^{-3} W / cm^2
Monochromatic wavelength	600 nm
Reflectance	35 %
Bulk recombination ($\tau_n = \tau_p$)	1000 µs
Surface recombination velocity ($S_n = S_p$)	1 x 10^5 cm / s
Resistivity, p-type doping	20 Ω-cm
Thickness	600 µm
Surface charge (front = rear)	0 to 1 x 10^{13} / cm^2
Voltage bias (applied to back surface)	0 to 350V

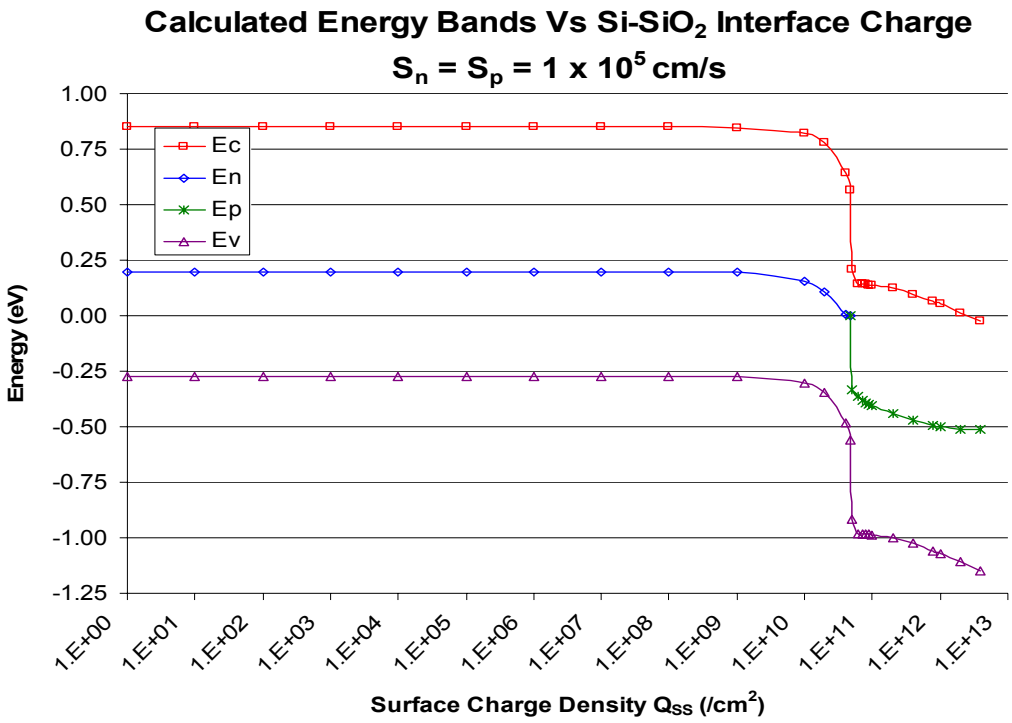

Figure 6-11: Calculated energy bands in silicon substrate

The calculated energy bands shown in Figure 6-11 are given for steady-state illumination using 600nm light at a maximum light intensity of 1.67mW/cm^2. There are several distinct regions of interest that govern the behavior of the osCPD sensor which are related to the biasing conditions at the top surface of the silicon substrate. These regions are listed in Table 6-4, and illustrated schematically in Figure 6-12. The biasing regions are dependent upon the surface charge, *Qss*, in the silicon substrate.

Table 6-4: Energy band biasing regions based on trapped surface charge

Region and Description	*Range of Surface Charge, Q_{ss}*
I. Flat Band	$0 < Q_{ss} < 1 \times 10^9$ / cm^2
II. Depletion	1×10^9 / cm^2 $< Q_{ss} < 4 \times 10^{10}$ / cm^2
III. Onset of Inversion	$Q_{ss} = 4 \times 10^{10}$ / cm^2
IV. Inversion	4.8×10^{10} / cm^2 $< Q_{ss} < 4 \times 10^{12}$ / cm^2
V. Degeneracy	$Q_{ss} > 4 \times 10^{10}$ / cm^2

Dependency of Predictive Model on PC1D Results

It should be noted that the accuracy of the calculations of the PC1D software are dependent upon the accuracy of the material properties and boundary conditions. The absolute value of predicted surface potential is therefore questionable for any given model. However, the overlying trend in the behavior of the silicon substrate with respect to photovoltaic response and dependency upon trapped charge is consistent within the range of parameters evaluated. That is, although the absolute numbers calculated for this set of parameters may be in error, the behavior and magnitude of the relative change in osCPD signal due to changes in the fluid sample are accurately predicted by this method. Results and conclusions should therefore be interpreted as relative changes, and not absolute measurements.

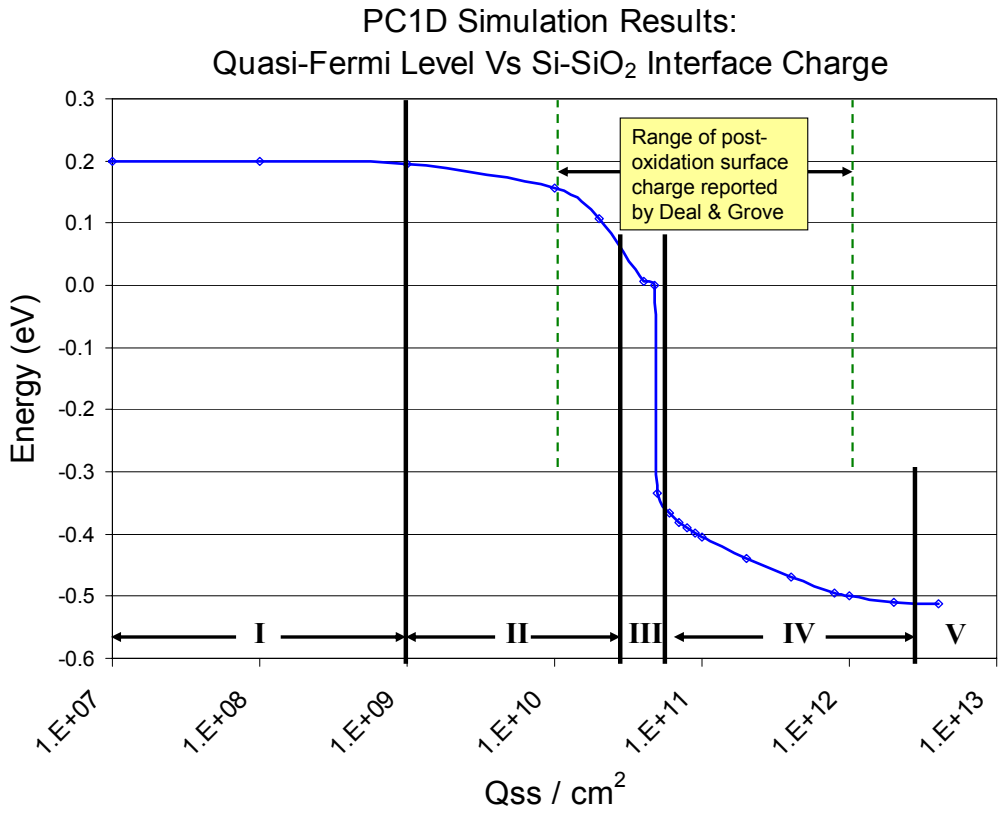

Figure 6-12: Light-induced quasi-Fermi level as a function of surface charge

Effect of Incident Light Intensity

Simulations were also conducted that varied the intensity of the incident light for a given surface charge. As seen in Figure 6-13, the electron quasi-Fermi level varies logarithmically with incident light intensity. However, the analysis as performed assumed quasi-static conditions (i.e. steady-state). In actuality, the response of the surface charge to time varying light intensity would be less abrupt due to the physical response of the system. Therefore, linear proportionality was used to approximate the relationship between light intensity and surface charge. In the finite response model

developed in the following sections, it is implicitly assumed that the surface potential is linearly proportional to intensity.

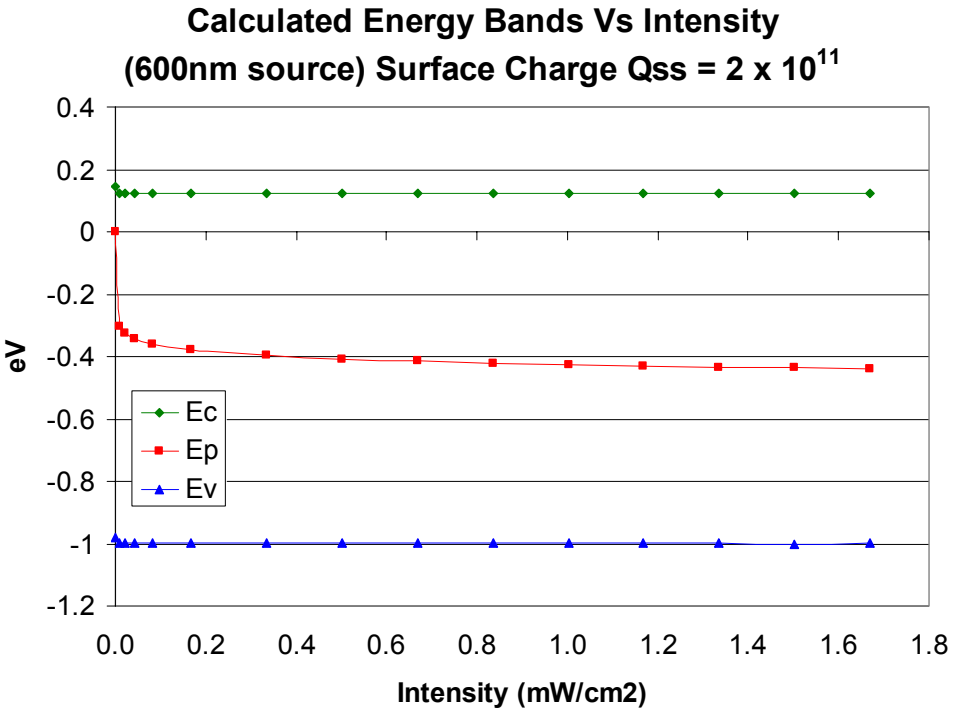

Figure 6-13: Calculated quasi-Fermi level as a function of incident light intensity

Effect of Applied Voltage Bias

The effect of an applied voltage bias to the rear surface of the silicon substrate was simulated using PC1D. The primary effect of the applied bias is to shift the entire band structure of the silicon substrate. Since the response of the probe tip is due to the modulation of the quasi-Fermi level, it is not expected that application of a voltage bias would affect the osCPD sensor signal. This is in agreement with the results presented in Chapter 5 in which the osCPD signal varied linearly between a minimum offset of -0.25V with respect to unbiased response, and a maximum of approximately +0.5V for corresponding applied voltage biases of -350V and +350V, respectively.

CPD Probe Tip Finite Response Model

As shown previously, the current in the CPD probe tip, i_{CPD}, is given by

$$i_{CPD}(t) = \frac{C_{eq}}{|e|}\frac{\partial \phi_s(t)}{\partial t} \tag{6.39}$$

In order to create a finite response model, this can be approximated by the discrete series

$$i_{CPD}(t) = C_{eq} \cdot \frac{\Delta \phi_s}{|e|\Delta t} \tag{6.40}$$

Discrete values for ϕ_S can be calculated for given surface charge and light intensity using the PC1D simulation tool. The light intensity as a function of time depends on the rotational speed and geometry of the chopper blades. As the chopper rotates, individual blades move past the aperture. The amount of light that is incident on the back surface of the silicon substrate is directly proportional to the fractional area of the aperture that is exposed, so the intensity can be expressed in terms of the area of the aperture as

$I(t) = 0$ when the chopper blade blocks the aperture (6.41a)

$I(t) = I_o \cdot A(t)$ as the blade uncovers the aperture (6.41b)

$I(t) = I_o$ when the aperture is fully exposed (6.41c)

$I(t) = I_o \cdot [1 - A(t)]$ as the next blade moves back over the aperture (6.41d)

Figure 6-14 shows the calculated intensity profile based on the experimental parameters used in the measurement of thermally aged Mobil1. The intensity varies between a minimum of 0 mW/cm^2 when the chopper blade completely covers the aperture, and 1.67 mW/cm^2 when the aperture is fully exposed (as measured with the optical power meter).

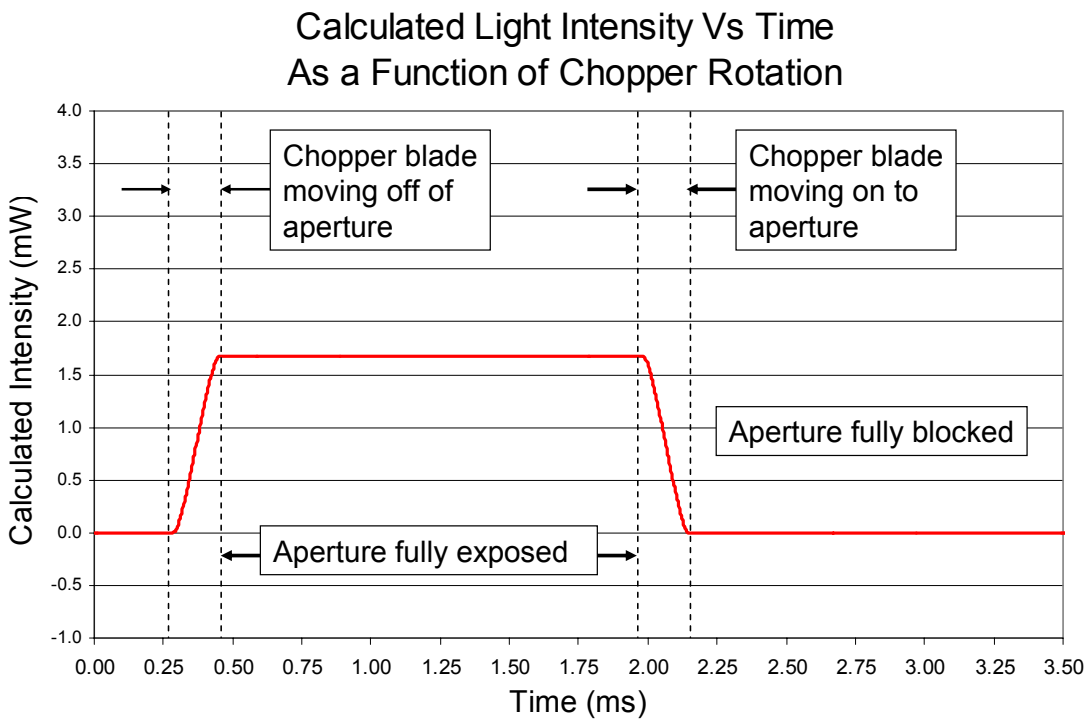

Figure 6-14: Calculated intensity profile based on experimental parameters

As seen in Figure 6-14, the intensity profile is assumed to be completely symmetric. That is, the rate of increase in intensity as the chopper blade exposes the aperture is implicitly assumed to be identical to the rate of decrease in intensity as the chopper blade covers the aperture. As discussed previously, ϕ_s is assumed to be a linear function of intensity, and can be expressed as

$$\phi_s(t) \cong \phi_{so} \cdot I(t) \tag{6.42}$$

where ϕ_{so} is the steady-state value for maximum light intensity calculated using PC1D and $I(t)$ is the calculated intensity profile shown in Figure 6-14. A typical calculated profile for $\phi_s(t)$ is shown in Figure 6-15.

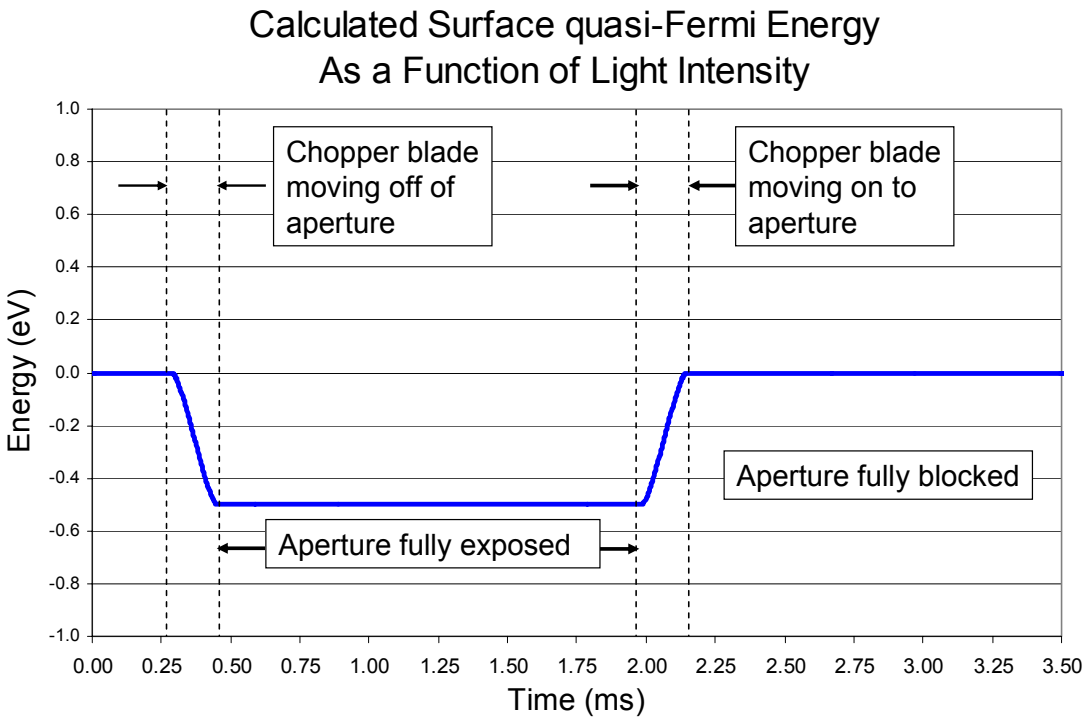

Figure 6-15: Calculated quasi-Fermi energy based on light intensity profile

Combining Equations 6.40 and 6.42, the final discretized expression for the induced current in the CPD probe tip is therefore predicted to be

$$i_{CPD}(t) = C_{eq} \cdot \frac{\left[\phi_{so} \cdot I(t_{n+1}) - \phi_{so} \cdot I(t_n)\right]}{|e| \cdot \left[t_{n+1} - t_n\right]} \tag{6.43}$$

CPD Current to Voltage Conversion and Amplification

The CPD current at the probe tip surface, i_{CPD}, is converted to a voltage at the 1st stage amplifier input by the resistance of probe tip itself by

$$V_{input} = i_{CPD} \cdot R1 \tag{6.44}$$

where $R1$ is the probe tip resistance, 12kΩ, as shown in Figure 3-7. The output signal from the CPD amplification electronics, V_{signal}, is related to the input voltage, V_{input}, by

$$V_{signal} = V_{input} \cdot A_1 \cdot A_2 \tag{6.45}$$

Here,

$\mathbf{V_{input}}$ is the voltage at the input to the 1st stage amplifier,

$\mathbf{A_1}$ = 8.3 x 10^4 is the 1st stage gain of the CPD electronics, and

$\mathbf{A_2}$ = 9.8 is the 2nd stage gain of the CPD electronics.

The data acquisition software artificially amplified the data by a factor of 10 for ease of viewing so that the final voltage signal as recorded by the data acquisition software is

$$V_{osCPD} = V_{signal} \cdot 10 \tag{6.46}$$

The overall gain of the osCPD system including the CPD electronics and the artificial gain of the software can be calculated as

$$G = R1 \cdot A1 \cdot A2 \cdot 10 = 9.8x10^{10} \tag{6.47}$$

The final voltage signal, V_{osCPD}, can therefore be expressed in terms of the total gain as

$$V_{osCPD}(t) = G \cdot i_{CPD}(t) \tag{6.48}$$

Substituting the discrete expression for $i_{CPD}(t)$ presented in Equation (6.36), a finite response model for the osCPD sensor output can be expressed as

$$V_{osCPD}(t) = G \cdot C \cdot \frac{\left[\phi_{so} \cdot I(t_{n+1}) - \phi_{so} \cdot I(t_n)\right]}{|e| \cdot \left[t_{n+1} - t_n\right]} \tag{6.49}$$

Predicted osCPD Sensor Waveform

Equation 6.49 was used to simulate predicted osCPD sensor response using a Microsoft Excel spreadsheet. Inputs to the spreadsheet were taken from results from the PC1D simulation model, as well as from physical measurements of the experimental system. The resulting predicted waveform is shown in Figure 6-16. The symmetry of the positive

and negative peaks is due to the underlying assumption that the surface potential is linearly proportional to incident light intensity. For reasons previously discussed, this is not strictly the case either in light-on or in light-off transition. It should also be recalled that the capacitance of the oil was assumed to be invariant between samples based on experimental data for the range of samples evaluated. This may not be an accurate assumption over a broader range of samples.

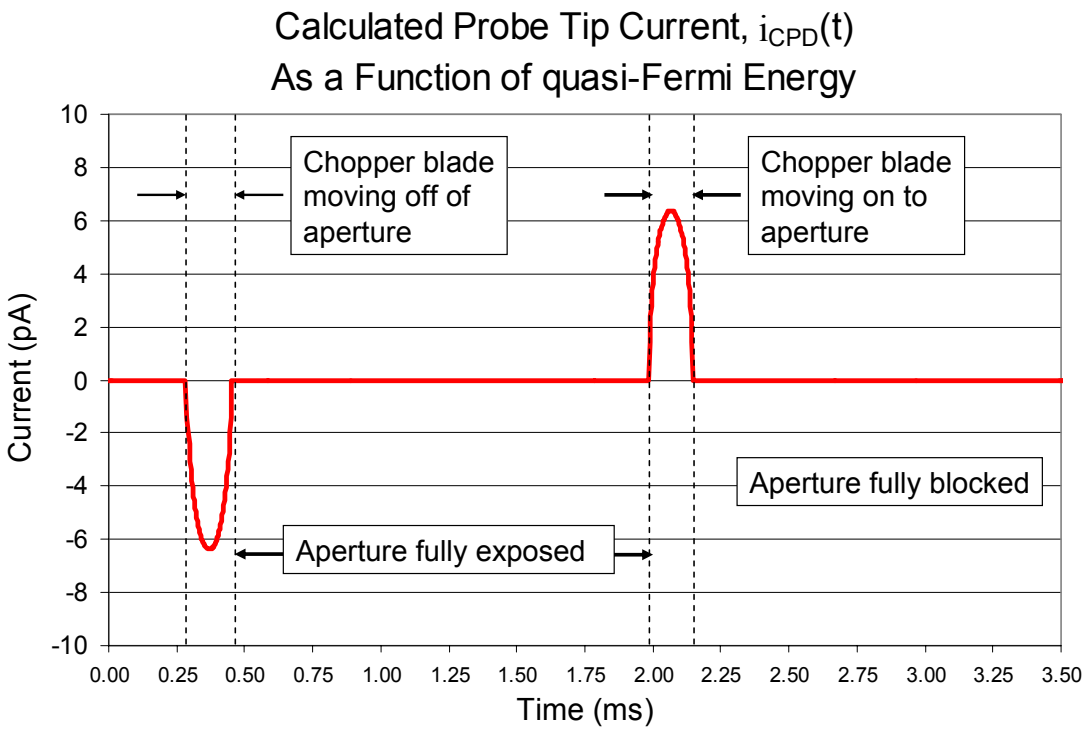

Figure 6-16: Calculated probe tip current based on quasi-Fermi energy

Once all of the optical, geometric and material parameters have been loaded into the Excel model, the only parameter that remains variable is the energy of the quasi-Fermi level at the silicon surface. This value is adjusted until amplitude of the predicted waveform matches the amplitude of the osCPD signal. In this fashion, a predicted value for the magnitude of trapped surface charge, Q_{ss}, is inferred.

Comparison of Predictive Models with Experimental Results

Using the methodology described in the previous sections, predicted waveforms for the 10W30 Mobil1 experiments were created using the Excel Spreadsheet model. The experimental parameters were used as input to the model, and the magnitude of the quasi-Fermi level of the silicon surface was adjusted until the amplitude of the predicted waveform equaled the magnitude of the osCPD sensor waveform for a given oil sample. The predicted versus actual waveforms are shown in Figures 6-17, 6-18, and 6-19 for New, 512-hour, and 1024-hour equivalent thermal aging, respectively.

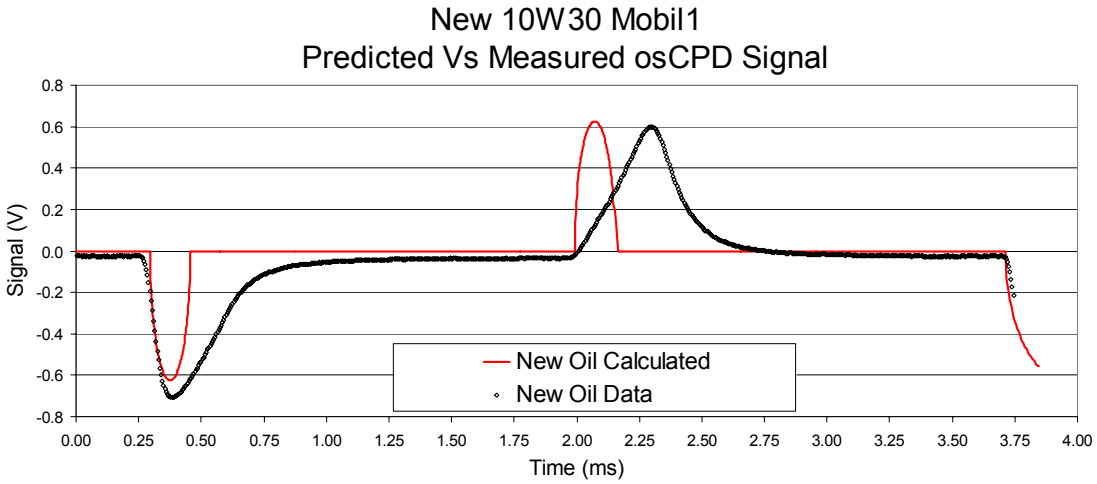

Figure 6-17: Comparison of osCPD model with data – new oil

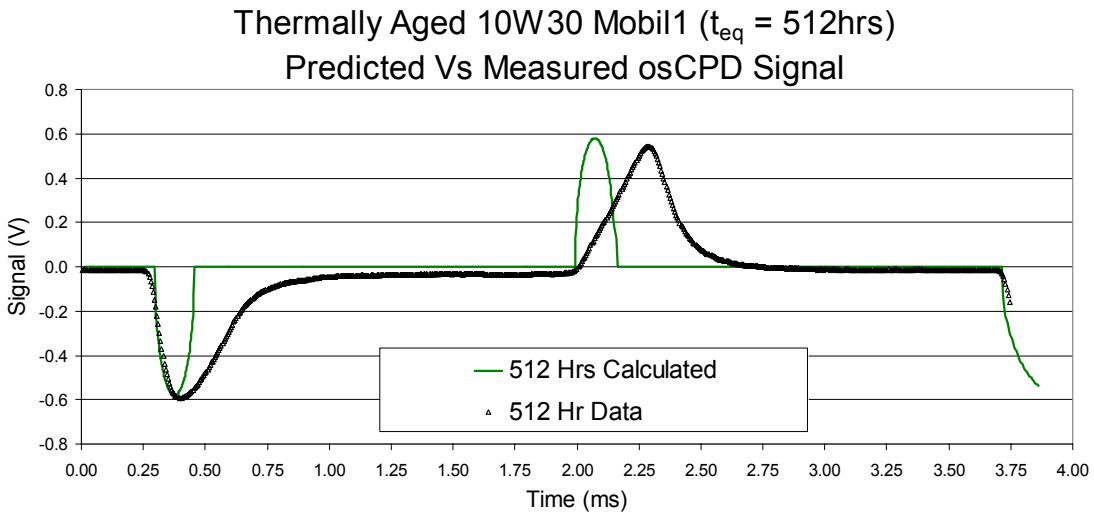

Figure 6-18: Comparison of osCPD model with data – 512hr oil

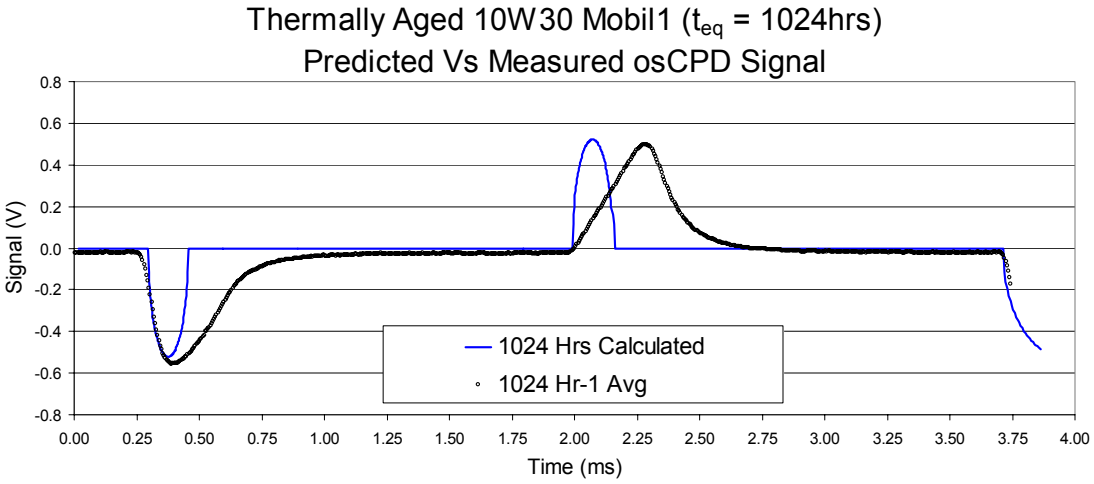

Figure 6-19: Comparison of osCPD model with data – 1024hr oil

Calculated peak-to-peak voltages, V_{pp}, from the preceding charts are presented in Figures 6-20 and 6-21. The excellent correlation between the predicted values and actual data is due to the previously described method for selecting the surface potential to match the amplitude of the osCPD data. Since there was no change in the oil sample between the two experiments, no change was made to the model. The predicted value for Vpp is identical in Figure 6-20 and in Figure 6-21. The deviation between the predicted and actual values seen in Figure 6-21 is indicative of the slight variability in measurements between the two sets of experiments. The repeatability appears to be very good.

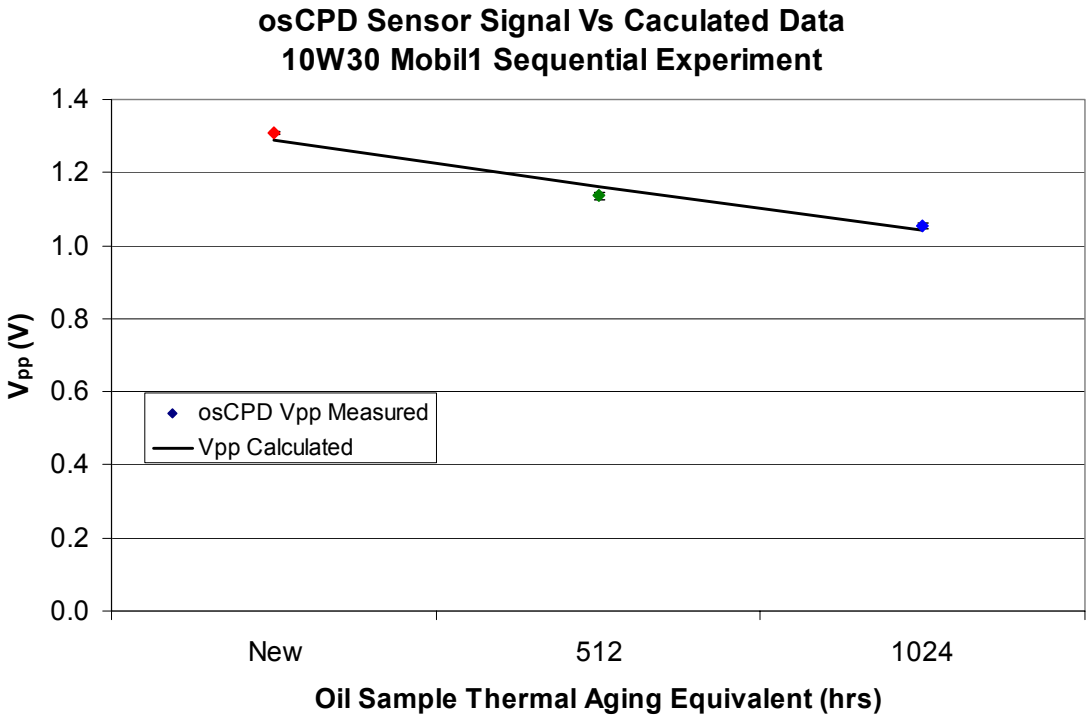

Figure 6-20: Model comparison with data for sequential experiments – V_{pp} Summary

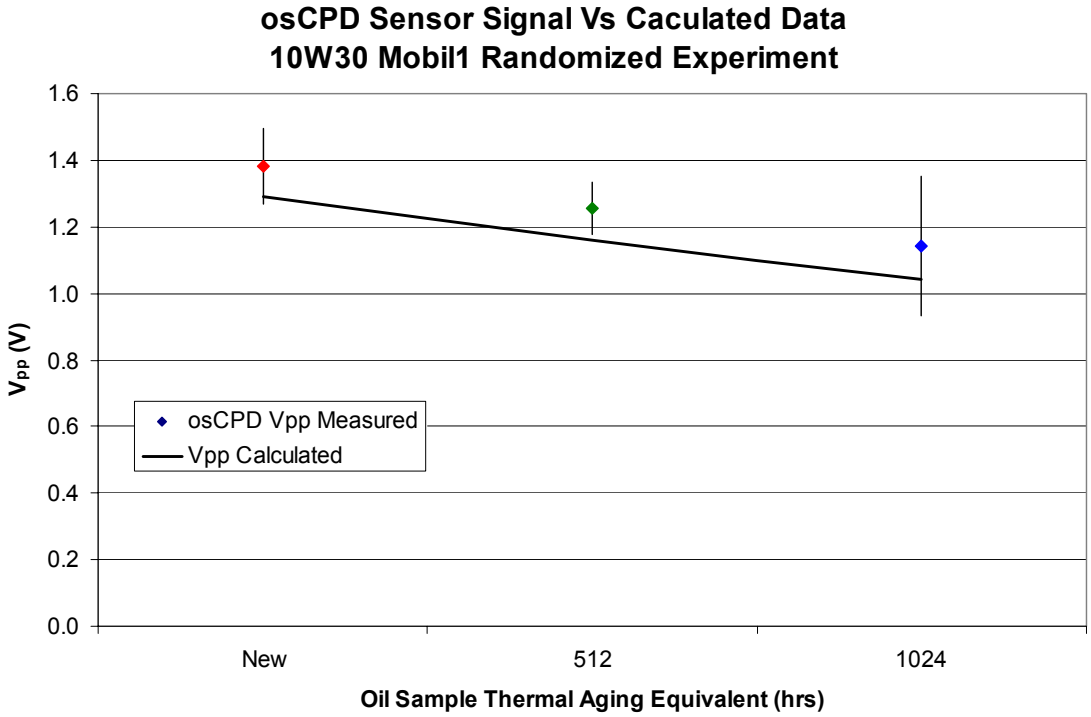

Figure 6-21: Model comparison with data for sequential experiments – V_{pp} Summary

Table 6-5 Summarizes the predicted versus measured peak-to-peak voltages for the osCPD sensor in the thermal aging experiments for 10W30 Mobil1. The last column indicates the value for fs that was selected to amplitude-match the predicted waveform with the osCPD waveform from the sequential data. Figure 6-22 contains a graph showing where the selected values for surface potential lie with respect to calculated values for surface potential.

Table 6-5: Predicted versus measured osCPD signal for 10W30 Mobil1

Oil Sample	V_{osCPD} *data Sequential*	V_{osCPD} *data Round-robin*	V_{pp} *model Predicted*	ϕ_s *used in model*
New	1.31	1.38V	1.25V	.50 eV
512-hour	1.14	1.26V	1.13V	.45 eV
1024-hour	1.05	1.14V	1.01V	.41 eV

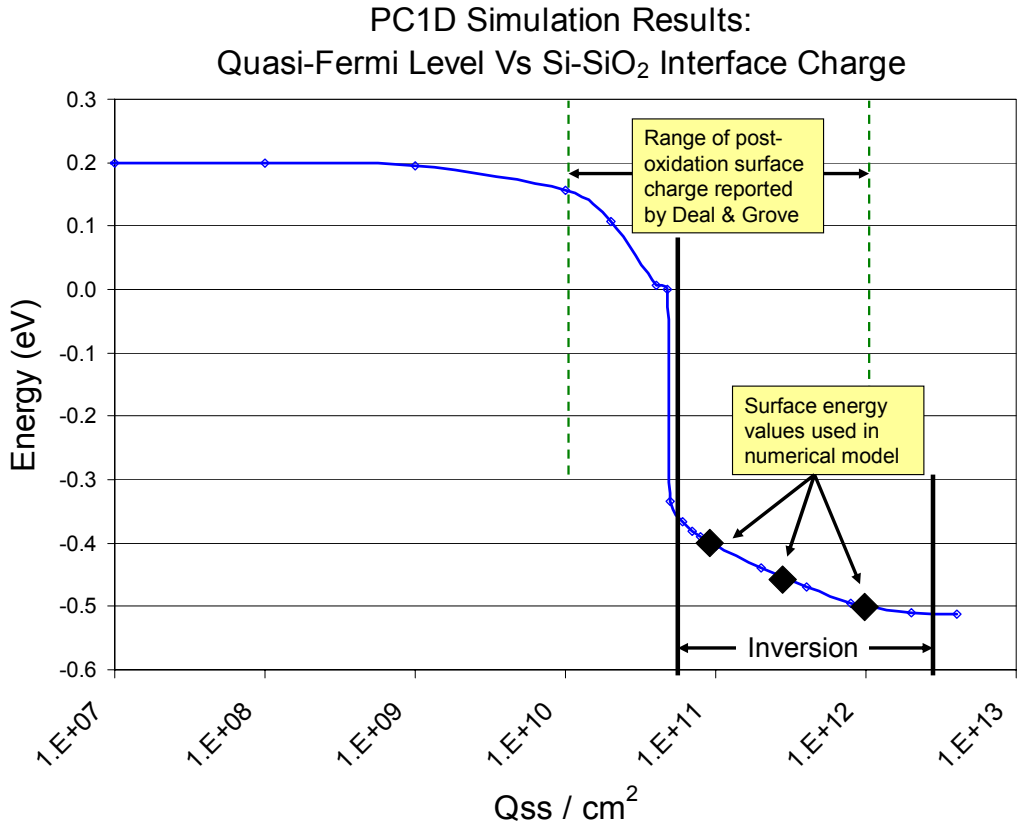

Figure 6-22: Predicted quasi-Fermi level and values used in numerical model

As seen in Figure 6-22, all of the selected values for the quasi-Fermi level at the top surface of the silicon substrate fall within the inversion region predicted by the PC1D simulation tool. This range of surface charge also lies well within the range of charge due to trapped charges from low-temperature oxidation[43].

It should be noted that the model as presented is based entirely on material properties of the silicon substrate as well as geometric properties of the test system. The shape of the predicted waveform is determined entirely by these physical properties; it is only the amplitude of the waveform that is fit to the data.

Extension of osCPD Predictive Model to the Adsorption Isotherm

Instead of predicting the change in work function as a function of adsorbate concentration, if the change in work function is calculated from osCPD measurements, the change in concentration of adsorbate species can be deduced by rearranging Equation 6.27 as

$$\Delta\theta = \frac{\varepsilon_0 \varepsilon_r}{\mu_p N}\left[\Phi_2 - \Phi_1\right]. \tag{6.50}$$

Here, Φ_1 and Φ_2 are calculated based on osCPD measurements of different oil samples. Related ongoing research in the Electronic Materials Research Lab using a vibrating CPD probe to evaluate the same oil samples has provided an estimate of the dipole moment of the active adsorbate species as μ_p=0.079D. Setting the number of active surface sites, N, on the SiO_2 surface equal to $7x10^{14}$ / cm^2 allows the relative change in adsorbate concentration, $\Delta\theta$, to be calculated using Equation 6.50. Calculated results are shown in Table 6-6.

Table 6-6: Calculated change in adsorbate concentration at SiO_2 surface

Oil Sample	$\Delta\phi$	$\Delta\theta$
512-hour	0.05eV	48%
1024-hour	0.045eV	43%

The calculated surface concentration of the adsorbate is shown to be reduced by 48% after 512 hours of equivalent thermal aging, and by an additional 43% after 1024 hours of equivalent thermal aging. If the number of surface sites, N, is varied, the predicted percentage change in coverage will change in inverse proportion. For example, setting

the number of active surface sites, *N*, on the SiO_2 surface equal to $1x10^{15}$ / cm^2 yields predicted successive reductions in surface coverage of 34% and 30%, respectively.

An alternative expression for the Helmholtz equation is given by[30]

$$A_m = \frac{\mu_p}{\varepsilon_o \varepsilon_r \left[\Phi_2 - \Phi_1\right]} \tag{6.51}$$

where A_m is the surface area occupied by the polar end-group of one molecule. Taking this approach, the area of the depleted adsorbate in these experiments is calculated to be

$$A_m = 1.9x10^{-19} m^2 \tag{6.52}$$

This number compares reasonably well with the value of $7.85x10^{-19}$ m^2 calculated by Korach et al. in their study of adsorption of PFPE lubricant on a hard disk surface[30].

Sensitivity and Limits of Adsorption Calculations

It should be noted that the adsorption calculations performed are relative in nature, and not absolute quantities. The adsorption analysis is based on assumed adsorbate properties. Any of these values will directly influence the magnitude of the calculated quantities, but not the trend or behavior as predicted. Calculated values also depend on the results of the osCPD finite response model which is fundamentally a relative response as discussed previously. However, as evidenced by the correlation with other physical measurements (light absorption and oxidation measurements) the model is in good agreement with experimental observations for the range of parameters investigated.

Summary

This chapter developed predictive models that relate the osCPD sensor output signal to the chemical and dielectric properties of the oil sample, as well as to the geometry, composition, and control inputs of the silicon substrate and test fixture. The osCPD signal generation process was described in four principle stages to include photon absorption and photo-generation, minority carrier diffusion and the formation of a space charge region at the $SiSiO_2$ interface, adsorbed dipole layer interaction with the space charge region, and CPD probe response. The process can be briefly summarized as follows.

An intensity modulated light source selectively illuminates the back surface of the silicon substrate. Photon absorption leads to electron-hole pairs creation (generation) and a significant increase in the electron density of the p-type substrate. Minority carrier diffusion at steady state illumination leads to the creation of a space charge region at the top surface of the silicon substrate with an associated surface potential. The surface potential is proportional to the incident light intensity, and is modulated between flat band and some maximum as the light is chopped. The CPD probe detects the modulation of the surface potential. A dipole layer formed by adsorbed molecules from the fluid sample interacts with the space charge region and affects the value of surface potential achieved during steady state illumination. The peak-to-peak CPD signals for different adsorbate concentrations vary according to the influence of the adsorbate on the surface potential of the silicon substrate.

CHAPTER 7

CONCLUSIONS

The primary outcomes of this investigation can be summarized as follows:

1. A non-vibrating contact potential difference (CPD) probe has been used in conjunction with a semiconductor substrate and optical stimulus to form a new sensor, the optically stimulated contact potential difference sensor (osCPD).
2. A physics-based model predicting the osCPD sensor response was developed, and the final soCPD signal response was predicted to be of the form $i_{CPD}(t) = \frac{C_{eq}}{|e|}\frac{\partial \phi_s(t)}{\partial t}$ where $\phi_s(t)$ is the light-intensity modulated surface potential of the silicon substrate, and C_{eq} is determined by the geometry of the sensor.
3. Functional osCPD sensor prototypes were designed, fabricated, and tested. The osCPD sensor was shown to be capable of monitoring adsorption processes and charge interactions at a semiconductor surface. As tested, the sensor has a signal-to-noise ratio of 42dB with a predicted resolution of 0.005eV.
4. Degradation due to thermal aging of motor oil was detected by the osCPD sensor. The area of the polar end-group of the adsorbate species measured was calculated to be 1.9×10^{-19} m^2.
5. Data from the osCPD sensor is well correlated with oxidation behavior in the oil as determined by third-party measurements including optical spectroscopy, FTIR, total acid number, and total base number measurements.

Recommendations for Future Investigation

The basic model for signal generation presented in this work should provide an ample basis for a wide range of future research activities. These activities include modification and improvement of the osCPD senor hardware, research into other areas of application, and refinement of the response model. Future investigations should also seek to understand the influence of the bulk dielectric properties of the fluid under investigation; although not detected in the current research, it is possible that the dielectric properties of the fluid under investigation may contribute substantially under different testing circumstances or as a result of alternate sample preparation techniques.

The osCPD sensor and test fixture utilized in this work was purpose-built to facilitate proof-of-concept experimentation. There are numerous opportunities to miniaturize and refine the sensor. The light source could be replaced with an LED or some other solid state, electronically modulated source. This would enable higher incident intensity transition rates, and larger amplitude signals. Different surface treatments of the silicon substrate should be investigated in order to develop chemically selective response as well as a more repeatable, controlled surface than can be created by uncontrolled oxidation at room temperature. Such investigations would lay the groundwork that could provide a path to a MEMS embodiment of the osCPD sensor. An array of sensors could be created on a single silicon substrate with a range of surfaces tailored to respond to a selected set of chemicals or contaminants. Ultimately, even the CPD probe tip could be built into the MEMS structure. If this were the case, both non-vibrating measurements (such as those currently made using the osCPD sensor) as well as vibrating CPD measurements could be made (using a cantilever or some other vibrating structure).

APPENDIX I

FERRIC CHLORIDE EXPERIMENTS

Experiments were conducted in which the oil chemistry was intentionally modified by a known additive. Samples of base stock oil (or virgin oil) and base stock plus 1000ppm ferric chloride ($FeCl_3$) were obtained from Analysts, Inc., a commercial oil analysis lab located in Norcross, Georgia. 38μm precision glass spacer beads were mixed with the oil prior to measurement on the osCPD system. The spacer beads were placed in new pre-marked vials for each sample. Using marked pipettes, a measured, consistent volume of oil was added to the vials containing the spacer beads. Major test parameters are listed in Table A1-1.

Table A1-1: Experimental parameters for ferric chloride experiment

Equipment/ Parameter	*Description / Settings and comments*
Oil Sample	Virgin Base Stock & Ferric Chloride Solution
Glass Spacers	38μm
CPD Probe	Custom-built as described in Chapter 3
Light Source	Source 600 nm, +/- 20nm; 1.67mW intensity
Optical Chopper Settings	7-blade chopper; 290 Hz chopping frequency
Voltage Bias	None / grounded

Twelve individual (111) p-type silicon substrates and matching mica spacers were used in conducting the individual sets of experiments. The silicon substrate and mica were soaked in an agitated petroleum ether bath for several minutes to remove the prior oil sample. Individual silicon-mica pairs were maintained, and care was taken to maintain

the vertical orientation of the silicon substrate (so that only the top surface was exposed to oil samples). Six of the silicon-mica pairs were loaded with virgin oil, and the other six were loaded with 1000ppm $FeCl_3$. After individual measurements were made on each of the samples, the silicon-mica pairs were washed, and the groups were reversed with respect to the sample that was loaded. A total of three sets of measurements was executed, and the grand average for each of the waveforms is shown in Figure A1-1. The data shows a very clear distinction between virgin oil and 1000ppm $FeCl_3$. As shown in Figure A1-2, however, the standard deviations for these measurements are much larger than for prior experiments using the same CPD probe and test fixture.

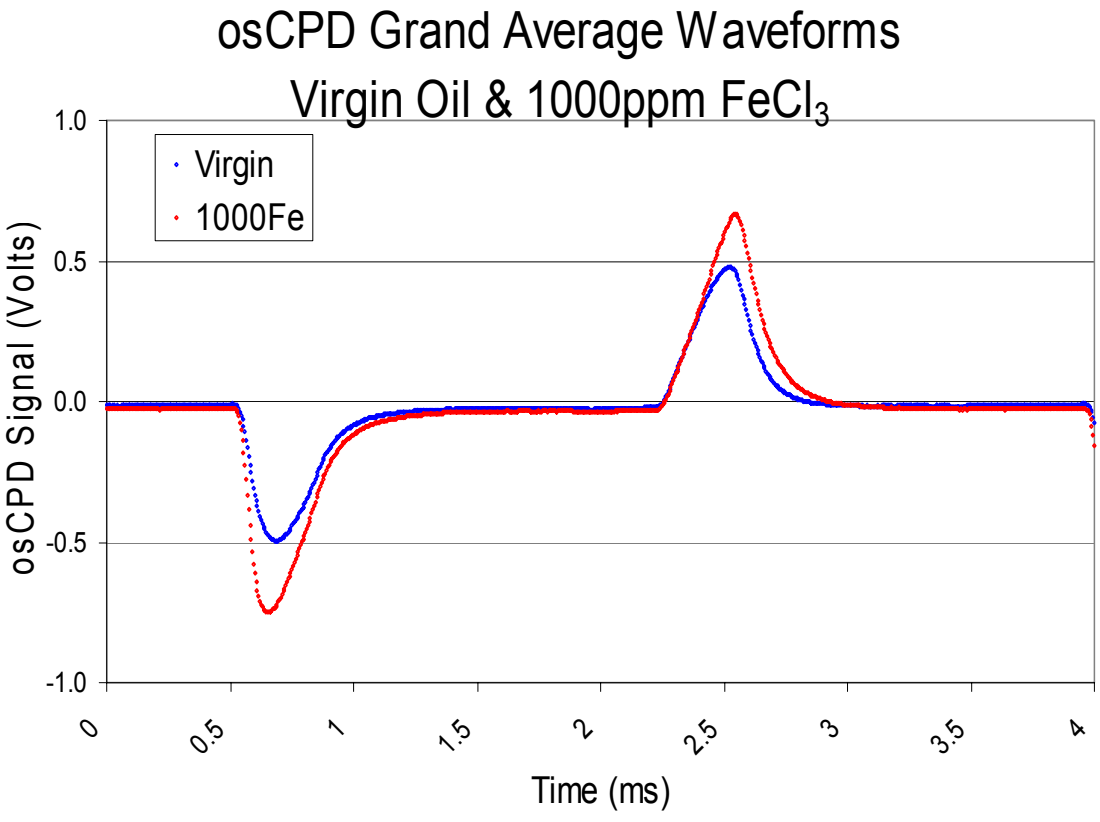

Figure A1-1: Scanned waveform from ferric chloride experiment

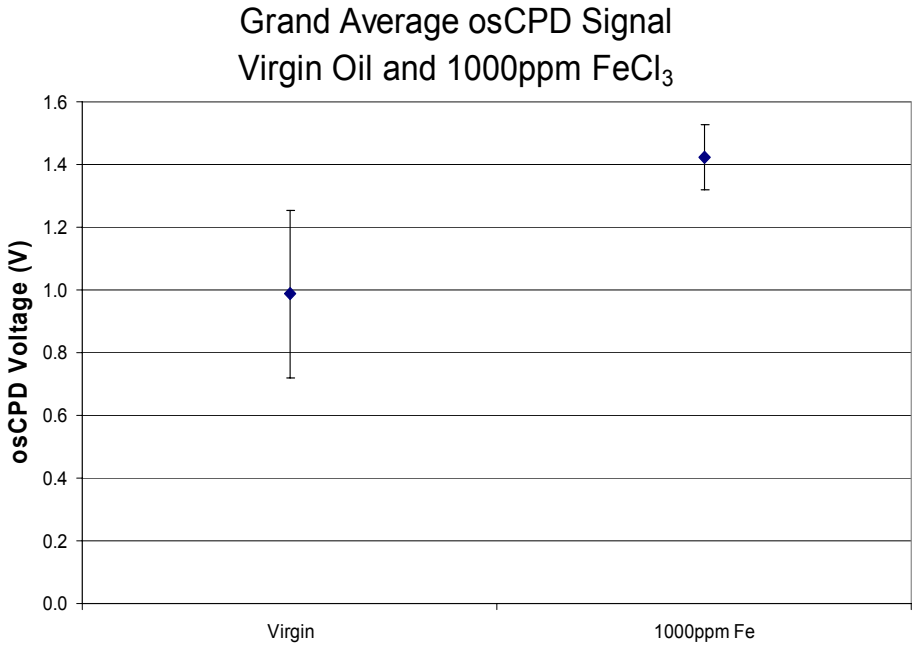

Figure A1-2: Peak-to-peak voltage data from ferric chloride experiment

Closer inspection of the data reveals that the cause for the greater variability in the data is due to hysteresis in the measurements, particularly with respect to measurements made on virgin oil. As can be seen in Figure A1-3, individual groupings of measurements do not show a large standard deviation. However, there is a substantial shift in the data for virgin oil between the first and last measurements made using the first group of silicon substrates. This can be seen in the two groups of data labeled "Si1 Virgin1" and "Si1 Virgin3". This is the same oil sample measured on the same set of substrates, but with a set of $FeCl_3$ measurements made on the substrates in between. It would appear that exposure to the 1000ppm $FeCl_3$ sample results in an irreversible reaction at the SiO_2 surface. In the second group of substrates (Si2) the FeCl3 samples are measured first (Si2 1000Fe1), and the virgin oil samples are measured afterwards (Si2 Virgin2). The average value is very close to that for Si1 Virgin3.

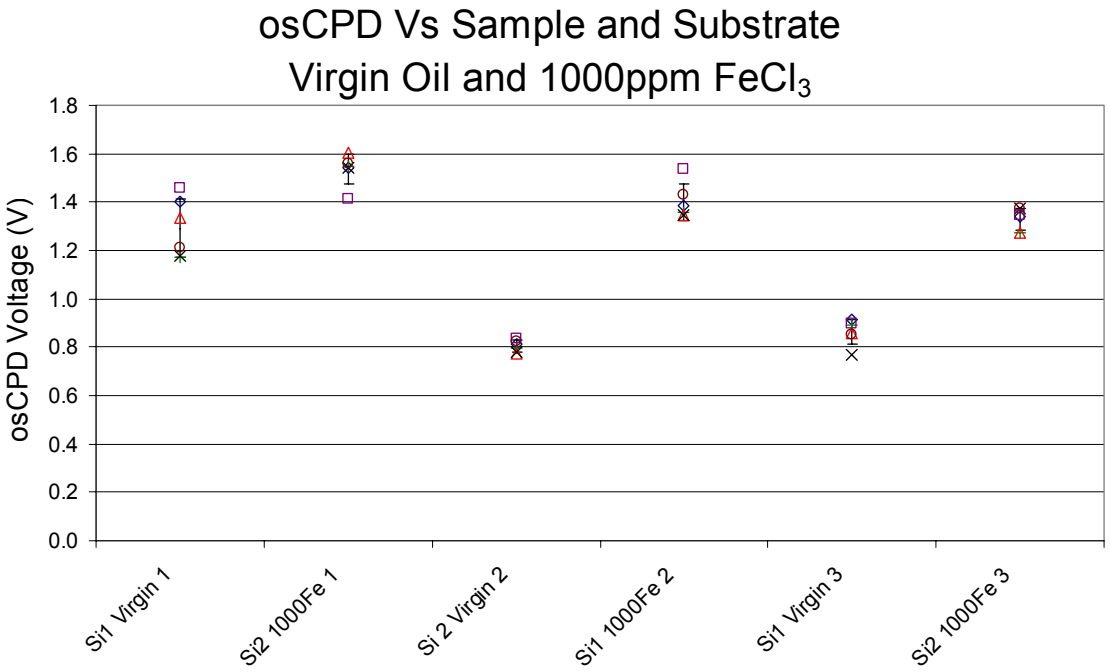

Figure A1-3: Peak-to-peak voltages for $FeCl_3$ in experimental order

The hysteresis is perhaps better illustrated by Figure A1-4 and A1-5 in which the $FeCl_3$ samples and the virgin oil samples are presented as separate groups. In figure A1-4, the successive signals for the $FeCl_3$ samples can be seen to be gradually decreasing in amplitude, suggesting that the surface reaction is ongoing, or possibly that ionic diffusion into the SiO_2 is taking place over time. The sensor signals for the virgin oil samples as seen in Figure A1-5 experience an abrupt reduction in peak-to-peak voltage if placed on a substrate that has been exposed to $FeCl_3$. This suggests that a non-reversible chemical reaction occurs at the SiO_2 surface due to the presence of the $FeCl_3$.

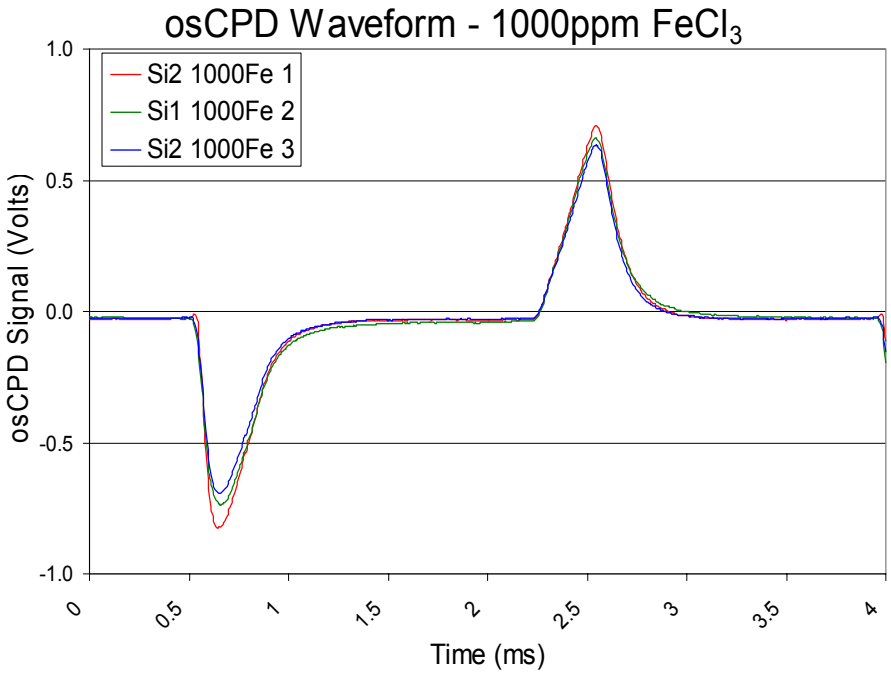

Figure A1-4: Scanned waveform data for 1000ppm $FeCl_3$

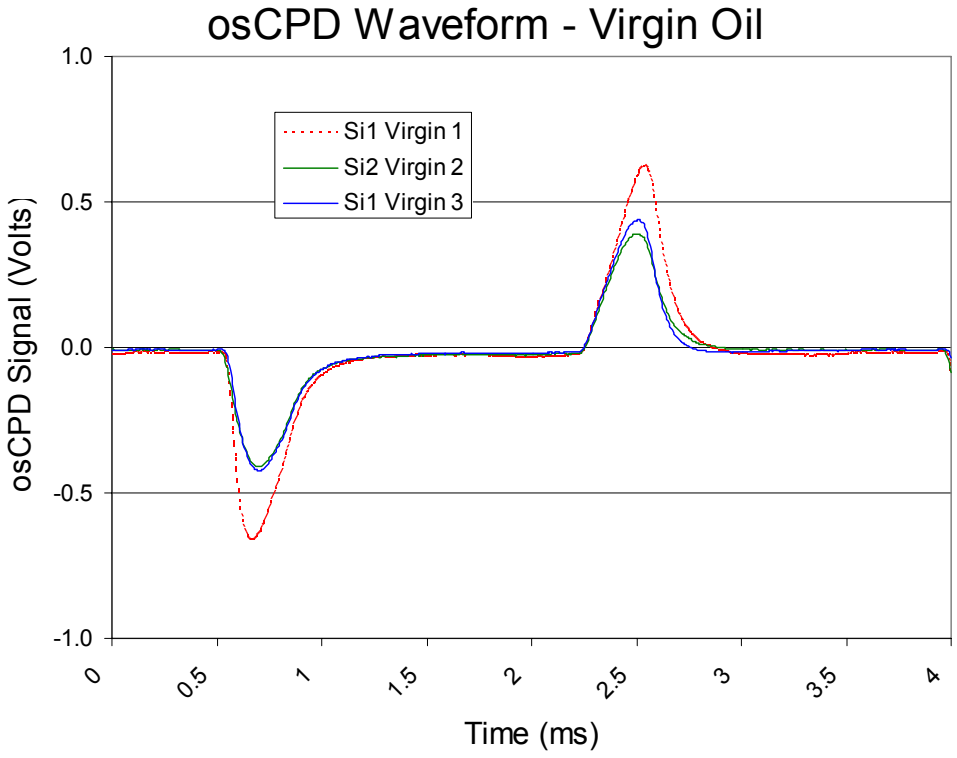

Figure A1-5: Scanned waveform for virgin oil (base stock)

APPENDIX II

COMMERCIAL LAB ANALYSIS OF OIL SAMPLES

Measurements were made on the thermally aged 10W30 Mobil1 by Analysts, Inc, a commercial oil analysis lab located in Norcross, Georgia. The three measurements performed were Absolute Oxidation (ABS Ox), Total Base Number (TBN), and Total Acid Number (TAN). The data for these measurements is shown in Figure A2-1.

The ABS Ox measurement was performed using a commercially available laboratory oil analyzer manufactured by Digilab. The measurement is an infrared analysis technique in which a range of wavelengths is transmitted through the oil sample, and transmittance is measured. The ABS Ox numbers as reported are somewhat arbitrary in that they represent the integrated area of a transmission scan between $2000cm^{-1}$ and $600cm^{-1}$ (a range of wave numbers known to be associated with oxidation byproducts). Thus, ABS Ox numbers as reported are specific to the equipment used to make the measurement. As seen in Figure A2-1, the ABS Ox values initially show a decrease in value through 512 hrs, then show a gradual increase in value. The general trend of this data versus the osCPD data is similar, although the osCPD sensor indicates monotonically decreasing signal through 1024 hours of equivalent thermal aging.

The Total Base Number (TBN) measurement was performed according to[45] ASTM D2896-05, "Standard Test Method for Base Number of Petroleum Products by Potentiometric Perchloric Acid Titration." The data shows a good correlation with the data from the osCPD sensor in that the output signal is monotonically decreasing through the full ranges of equivalent thermal aging that was evaluated.

The Total Acid Number (TAN) measurement was performed according to[46] ASTM D664-04, "Standard Test Method for Acid Number of Petroleum Products by Potentiometric Titration." The TAN test data appears to show the strongest correlation with the osCPD sensor data.

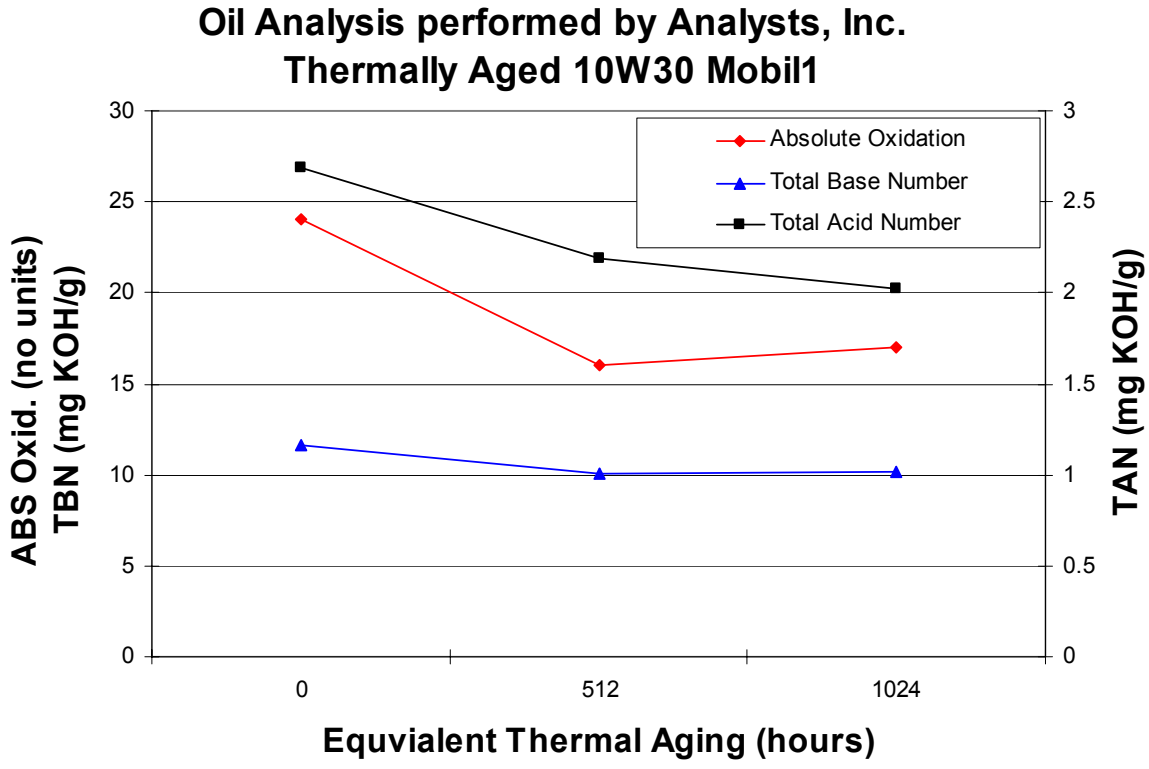

Figure A2-1: Analysis by Analysts, Inc. of thermally aged Mobil1 Samples

REFERENCES

1. A. Dabrowski, "Adsorption – from theory to practice," *Advances in Colloid and Interface Science v 93, n 1-3,* (2001) p135

2. J. Janata, M. Josowicz, P. Vanysek, D.M. DeVaney, "Chemical Sensors," *Analytical Chemistry v70 n12* (1998) p179R

3. J. Gardner, V. Varadan, O. Awadelkarim, "*Microsensors, MEMS, and Smart Devices," John Wiley & Sons, New York 2001*

4. Figaro Engineering, Inc. Osaka Japan, "Thecnical Information on Usage of TGS Sensors for Toxic and Explosive Gas Leak Detectors" *Accessed December 12, 2005* < http://www.figaro.co.jp/en/item2.html >

5. C.T. Sah, "Evolution of the MOS Transistor – From Conception to VLSI," *Proceedings of the IEEE v76 n10* (1988) p1280

6. P. Bergveld, "Development of an Ion-Sensitive Solid-State device for neurophysiological measurements," *IEEE Transactons Bio-Medical Engineering, v BME-17 n1* (1970) p70

7. K.I. Lundstrom, M.S. Shivaraman, C.M. Svensson, "A hydrogen-sensitive Pd-gate MOS transistor," *Journal of Applied Physics, v46 n9* (1975) p3876

8. J.V.Hatfield, J.A. Covington, J.W. Gardner, "GasFETs incorporating conducting polymers as gate materials," *Sensors and Actuators B: Chemical v65 n1* (2000) p253

9. J. Janata, M. Josowicz, "A Fresh Look at Some Old Principles: The Kelvin Probe and the Nernst Equation," *Analytical Chemistry, v69 n293* (1997) p293A

10. D.G. Hafeman, J.W. Parce, H.M. McConnell, "Light-Addressable Potentiometric Sensor for Biochemical Systems," *Science v240 n2856* (1988) p1182

11. D. Troyer, J. Fitch, "Oil Analysis Basics," Noria Corporation, Tulsa, Oklahoma 2001

12. J. Janata, M. Josowicz, "Chemical Modulation of Work Function as a Transduction Mechanism for Chemical Sensors," *Accounts of Chemical Research v31 n5* (1998) p241

13. Kelvin, "Contact Electricity of Metals," *Philosophical Magazine v46* (1898) p82

14. W.A. Zisman, "A New Method of Measuring Contact Potential Differences in Metals," *Review of Scientific Instruments, v3 n7 (1932) p367*

15. S. Danyluk, "A UHV guarded Kelvin probe," *Journal of Physics E: Scientific Instruments v5 n5* (1972) p478

16. J. de Boer, H. Krusemaeyer, N. Jaspers, "Analysis and Improvement of the Kelvin Method for Measuring Differences in Work Function," *Review of Scientific Instruments, v44 n8* (1973) p1003

17. M. McKay, R. Dougal, "A simple modification of the Kelvin method of measuring differences in work function," *Journal of Physics E: Scientific Instruments v8 n1* (1975) p71

18. E. Zanoria, S. Danlyuk, A. Zharin, C. Bhatia, "Contact potential measurements of hard disk drive surfaces in humid environments," *Journal of Vacuum Science & Technology A: Vacuum, Surfaces, Films v14 n1 (*1996) p52

19. E. Zanoria, K. Hamall, S. Danyluk, A.L. Zharin, "The nonvibrating Kelvin probe and its application for monitoring surface wear," *Journal of Testing & Evaluation v25 n2* (1997) p223

20. Y. Yang, S. Danyluk, M. Hoeprich, "Rolling Element Skew in Tapered Roller Bearings," *Tribology Transactions v43 n3 (2000) p564*

21. Y. Yang, T. Kurfess, S. Liang, S. Danyluk, "Application of a specialized capacitance probe in bearing diagnosis," *Wear 225-229 nII* (1999) p1215

22. A. Watt, J. Zheng, A. Zharin, S. Danyluk, "Non-Contact In-Situ Measurement of Wear Particle Formation by Contact Potential Difference Techniques," *Proceedings, ICoPE* (2003)

23. I. Langmuir, "The adsorption of gases on plane surfaces of glass, mica, and platinum," *Journal of the American Chemical Society v40 (1918) p1361*

24. J.H. Schulman, E.K. Rideal. "On the Surface Potentials of Unimolecular Films of Long Chain Fatty Acids. Part I. Experimental Method," *Proceedings of the Royal Society of London. Series A v130 n813* (1931) p259

25. J.H. Schulman, E.K. Rideal. "On the Surface Potentials of Unimolecular Films of Long Chain Fatty Acids. Part II. The Evaluation of the Resolved Electric Moments," *Proceedings of the Royal Society of London. Series A v130 n813* (1931) p270

26. G. Phillips, "An electronic method of detecting impurities in the air," *Journal of Scientific Instruments v28 n11* (1951) p342

27. K.W. Bewig, W.A. Zisman, "Surface Potentials and Induced Polarization in Nonpolar Liquids Adsorbed on Metals," *Journal of Physical Chemistry v68 n7* (1964) p1804

28. O. Levine, W.A. Zisman, "Physical Properties of Monolayers Adsorbed at the Solid-Air Interface," *Presented at 130th meeting of the American Chemical Society, Division of Colloid Chemistry, Atlantic City, NJ, September 1956*

29. M. Beltzer, "Assessing Adsorption of Conventional Frication Modifying Molecules by Relative Contact Potential Difference Measurements," *Journal of Tribology v114 n4* (1992) p675

30. C.S. Korach, J. Streator, S. Danyluk, "Measurement of perfluoropolyether lubricant thickness on a magnetic disk surface," *Applied Physics Letters v79 n5 (2001) p698*

31. D. Yano, C. Korach, J. Streator, S. Danyluk, "Nonvibrating Contact Potential Difference Probe Measurement of a Nanometer-Scale Lubricant on a Hard Disk," *Journal of Tribology, Transactions of the ASME v121 n4* (1999) p980

32. D.K. Schroder, "Surface voltage and surface photovoltage: history, theory and applications," *Measurement Science& Technology v12 n3* (2001) pR16

33. E.O. Johnson, "Measurement of Minority Carrier Lifetimes with the Surface Photovoltage," *Journal of Applied Physics v28 n11 (*1957) p1349

34. I.D. Baikie, U. Petermann, B. Lagel, "UHV-Compatible spectroscopic scanning Kelvin probe for surface analysis," *Surface Science v433-435* (1999) p249

35. B. Lagel, I.D. Baikie, U. Petermann, "A novel detection system for defects and chemical contamination in semiconductors based upon the Scanning Kelvin Probe," *Surface Science v433-435* (1999) p622

36. H. Shimizu, "Atomic Bridging and Barrier-Type AC Surface Photovoltage Measurements on Iron- and Copper-Contaminated Silicon Surfaces," *Journal of The Electrochemical Society v150 n12* (2003) pG725

37. K. Dirscherl, I. Baikie, G. Forsyth, A. Van der Heide, "Utilisation of a micro-tip scanning Kelvin probe for non-invasive surface potential mapping of mc-Si solar cells," *Solar Energy Materials and Solar Cells v79 n4* (2003) p485.

38. J. Cogdell, "Foundations of Electrical Engineering," *Prentice Hall, Englewood Cliffs, New Jersey,1990*

39. Wikipedia Contributors, "Johnson-Nyquist noise," *Wikipedia, The Free Encyclopedia, Accessed December 12, 2005*, *11:07 UTC*
< http://en.wikipedia.org/w/index.php?title=Johnson-Nyquist_noise&oldid=29900873 >

40. R. Pierret, "Semiconductor Device Fundamentals," *Addison Wesley, New York 1996*

41. M.A. Green, "Solar Cells: Operating Principles, Technology and System Applications," *University of New South Wales, Kensington, New South Wales 1998*

42. S.M. Sze, "Physics of Semiconductor Devices, Second Edition," *John Wiley & Sons, New York,1981*

43. B.E. Deal, M. Sklar, A.S. Grove, E.H. Snow, "Characteristics of the surface-state charge (Qss) of thermally oxidized silicon," *Journal of the Electrochemical Society, v114 n3* (1967) p266

44. The Effects of Motor Oil on Contact Potential Difference," Terry Thomas, *MS Thesis, Georgia Institute of Technology* (1998)

45. ASTM D 2896-05, "Standard Test Method for Base Number of Petroleum Products by Potentiometric Perchloric Acid Titration," *ASTM International (2005)*

46. ASTM D 664-04, “Standard Test Method for Acid Number of Petroleum Products by Potentiometric Titration,” *ASTM International (2005)*

47. L. Bousse, S. Mostarshed, D. Hafeman, M. Satore, M. Adami, C. Nicolini, “Investigation of carrier transport through silicon wafers by photocurrent measurements” *Journal of Applied Physics v75 n8* (1994) p4000

48. J.R. Stetter, W.R. Penrose, S. Yao, ”Sensors, Chemical Sensors, Electrochemical Sensors, and ECS,” *Journal of the Electrochemical Society v150 n2* (2003) s11

49. J.N. Zemel, “Ion-Sensitive Field Effect Transistors and Related Devices,” *Analytical Chemistry v47 n2* (1975) p255A

50. W.G. Jung, “IC Op-Amp Cookbook, Third Edition,” *Prentice-Hall, Upper Saddle River, New Jersey 1997*

51. R.A. Pease, “Troubleshooting Analog Circuits,” *Newnes, Boston 1993*

VITA

Francis M. (Frank) Mess was born in 1971 in Washington D.C. and was raised in Alexandria, Virginia. His first career ambition was to become a pilot in the United States Marine Corps. Frank earned a full scholarship in the Naval Reserve Officer Training Corps as a Marine Option, and elected to attend the Georgia Institute of Technology. Frank was recognized for his leadership through promotion, and was also awarded medals for military excellence. A traumatic accident at the end of his junior year left Frank permanently disabled, and ended his military aspirations. After a year of absence from school while recuperating, Frank returned to Georgia Tech, this time focused on academics. He began work as an undergraduate research assistant in the Electronic Materials Lab under Professor Steven Danyluk. After earning the degree of Bachelor of Mechanical Engineering, Frank matriculated into the graduate program in mechanical engineering at Georgia Tech. He earned a Master's Degree in Mechanical Engineering, and his research in the area of Chemical Mechanical Polishing led to a research and development position at Lucent Technologies in the Optical Waveguides Group. After several years with Lucent, Frank was recruited as the first hire by YAFO Networks, a start-up company in Baltimore, Maryland that designed and built high-speed optical telecommunications equipment. Frank initially served as YAFO's Principle Mechanical Engineer and later as Director of Operations. After the collapse of the telecommunications market (and the associated demise of YAFO), Frank made the decision to return to Georgia Tech to finish the work he had begun on a Ph.D. In addition to completing degree requirements during his return to Atlanta, Frank took the opportunity to pursue other interests: He earned a PADI certification as an open-water diver, learned to fly, and founded and incorporated an engineering consulting company. At the time of publication of this dissertation, Frank is actively pursuing a return to a career in industry.